

21957



National Library / Bibliothèque nationale  
of Canada / du Canada

CANADIAN THESES  
ON MICROFICHE

THÈSES CANADIENNES  
SUR MICROFICHE

NAME OF AUTHOR/NOM DE L'AUTEUR

William A. Roga

TITLE OF THESIS/TITRE DE LA THÈSE

Ultrasonic Quantum Oscillations  
in Tin and Indium

UNIVERSITY/UNIVERSITÉ

U of Alberta

DEGREE FOR WHICH THESIS WAS PRESENTED/  
GRADE POUR LEQUEL CETTE THÈSE FUT PRÉSENTÉE

Ph.D

YEAR THIS DEGREE CONFERRED/ANNÉE D'OBTENTION DE CE DEGRÉ

1974

NAME OF SUPERVISOR/NOM DU DIRECTEUR DE THÈSE

Dr. S. B. Woods

Permission is hereby granted to the NATIONAL LIBRARY OF  
CANADA to microfilm this thesis and to lend or sell copies  
of the film.

L'autorisation est, par le présente, accordée à la BIBLIOTHÈ-  
QUE NATIONALE DU CANADA de microfilmer cette thèse et  
de prêter ou de vendre des exemplaires du film.

The author reserves other publication rights, and neither the  
thesis nor extensive extracts from it may be printed or other-  
wise reproduced without the author's written permission.

L'auteur se réserve les autres droits de publication; ni la  
thèse ni de longs extraits de celle-ci ne doivent être imprimés  
ou autrement reproduits sans l'autorisation écrite de l'auteur.

DATED/DATE

Oct 2/74

SIGNED/SIGNÉ

William A. Roga

PERMANENT ADDRESS/RÉSIDENCE FIXE

23 Wyndrock Drive  
Halifax, Nova Scotia

THE UNIVERSITY OF ALBERTA

ULTRASONIC QUANTUM OSCILLATIONS IN TIN AND INDIUM

---

by

©

WILLIAM ALEXANDER ROGER

A THESIS

SUBMITTED TO THE FACULTY OF GRADUATE STUDIES AND RESEARCH  
IN PARTIAL FULFILLMENT OF THE REQUIREMENTS FOR THE DEGREE

OF DOCTOR OF PHILOSOPHY

IN

PHYSICS

DEPARTMENT OF PHYSICS

EDMONTON, ALBERTA

FALL, 1974

THE UNIVERSITY OF ALBERTA

FACULTY OF GRADUATE STUDIES AND RESEARCH

The undersigned certify that they have read,  
and recommend to the Faculty of Graduate Studies and  
Research, for acceptance a thesis entitled ULTRASONIC  
QUANTUM OSCILLATIONS IN TIN AND INDIUM submitted by  
William Alexander Roger in partial fulfillment of the  
requirements for the degree of Doctor of Philosophy in  
Physics.

*A. B. ...*  
.....  
Supervisor

*A. B. Blake*  
.....

*Peter ...*  
.....

*J. S. ...*  
.....

*M. ...*  
.....

*E. ...*  
.....  
External Examiner

DATE: Oct 1, 1974

## ABSTRACT

Quantum oscillations in the ultrasonic attenuation that are periodic in the reciprocal of an applied magnetic field have been observed in tin and indium. The attenuation oscillations in both metals were observed in fields between 10 and 88 kilogauss, and are attributed to variations in the electronic density of states which also cause the de Haas-van Alphen effect.

The very complicated oscillatory dependence of the attenuation was resolved into component frequencies by digital Fourier analysis. These frequencies enabled extremal cross-sectional areas of the Fermi surface to be calculated. The cyclotron effective masses of many orbits were determined from the temperature dependence of the oscillation amplitudes.

Some interesting anomalies in the oscillation amplitudes of tin were observed and are discussed briefly. Finally, several frequencies in the oscillatory attenuation are assigned to orbits caused by magnetic breakdown. An estimate of the breakdown field at the two non-equivalent tunneling junctions is given.

## ACKNOWLEDGEMENTS

It is a pleasure to acknowledge the assistance and guidance of my supervisor, Dr. S.B. Woods, who gave freely of his time. In addition I am indebted to Dr. G. Rostoker for the loan of the digital data acquisition system, to Mr. B. Stackhouse for the use of his crystal growing furnace, and to Dr. G. Hughes for the use of the NMR apparatus. The continuing interest of Dr. J. Rowlands in this project and our many lively discussions is greatly appreciated.

I would like to acknowledge an assistantship from the University of Alberta and a fellowship from the Izaak Walton Killam Memorial Trust.

Finally, a special word of thanks to my wife, Betty, for her constant moral support and encouragement.

# TABLE OF CONTENTS

	<u>Page</u>
Chapter 1 INTRODUCTION	1
CHAPTER 2 THEORETICAL BACKGROUND	2
2.1 Introduction to the Fermi Surface	2
2.2 Quantum Oscillations in the Ultra-sonic Attenuation	5
2.2.1 Consequences of the Conservation Requirement	6
2.2.2 Formula for the Oscillatory Attenuation	9
2.2.3 Calculation of Effective Masses and Dingle Temperatures	11
2.3 Introduction to Magnetic Breakdown	12
CHAPTER 3 EXPERIMENTAL APPARATUS	14
3.1 Electronic Apparatus	14
3.2 Calibration of the Magnet	18
3.3 Cryostat	21
3.4 Sample Holder	24
3.5 Transducer Bonds	27
CHAPTER 4 SAMPLE PREPARATION	30
4.1 Tin Samples	30
4.1.1 Preparation of Tin Samples	30
4.1.2 Electronic Mean Free Path in Tin	33
4.2 Indium Sample	33
4.2.1 Preparation of Indium Sample	33

	<u>Page</u>
CHAPTER 4 (cont'd)	
4.2.2 Electronic Mean Free Path in Indium	34
CHAPTER 5 COMPUTATIONAL TECHNIQUE	35
5.1 Preparation of Data for Analysis	37
5.1.1 Inversion of the Magnetic Field	37
5.1.2 Elimination of Non- Oscillatory Background Attenuation	37
5.2 Determination of Oscillation Frequencies and Amplitudes	38
5.3 Correction Factor for the Oscillation Amplitude	40
5.4 Effective Mass Determination	47
CHAPTER 6 EXPERIMENTAL RESULTS	51
6.1 Fermi Surface Frequencies in Tin	51
6.1.1 Previous Investigations in Tin	52
6.1.2 Nomenclature for Identifying Frequencies in Tin	53
6.1.3 Composite Graph and Table of Fermi Surface Frequencies in Tin	54
6.1.4 Frequencies in the Three Principal Planes of Tin	55
6.2 Effective Masses in Tin	69
6.2.1 Elimination of Erroneous Data	69
6.2.2 Presentation of Effective Masses in Tin	72

	<u>Page</u>
<b>CHAPTER 6 (cont'd)</b>	
6.3 Comparison of Oscillation Amplitudes in Tin	77
6.3.1 Comparison of Amplitudes from Sn 2 and Sn 3.	77
6.3.2 Amplitudes of the Oscillations	79
<hr/>	
6.4 Fermi Surface Frequencies in Indium	82
6.5 Apparent Modulation of Two Frequency Branches	87
<b>CHAPTER 7 DISCUSSION OF EXPERIMENTAL RESULTS</b>	<b>91</b>
7.1 Fermi Surface Frequencies of Tin	91
7.1.1 Model of the Fermi Surface of Tin	91
7.1.2 Discussion of Frequency Branches of Tin	93
7.2 Cyclotron Effective Masses in Tin	117
7.3 Comparison of Oscillation Amplitudes in Tin	119
7.3.1 Comparison of Amplitudes from Sn 2 and Sn 3	120
7.3.2 Amplitudes of the Oscillations	120
7.4 Estimation of the Magnetic Breakdown Probabilities when H is parallel to [110]	121
7.5 Fermi Surface Frequencies of Indium	126
7.5.1 Fermi Surface Model of Indium	126
7.5.2 Assignment of Fermi Surface Frequencies in Indium	126
<b>CHAPTER 8 CONCLUSIONS</b>	<b>129</b>



	<u>Page</u>
BIBLIOGRAPHY	132
APPENDIX 1 . Crystallographic Data for White Tin and Indium	136
APPENDIX 2 . Definitions of Crystallographic Plane and Cut-off of an Orbit	137

---

## LIST OF TABLES

	<u>Description</u>	<u>Page</u>
1	Data for the three tin specimens	32
2	Fermi surface frequencies in tin at [001]	58
3	Fermi surface frequencies in tin at [100] or [110]	60
4	$m_C^*$ in tin at [001]	72
5	$m_C^*$ in tin at [100]	75
6	$m_C^*$ in tin at [110]	76
7	$m_C^*$ in tin in the (110) plane	78
8	Amplitude ratios in tin at [100] and [001]	80
9	Maximum to minimum amplitude ratios in tin	81
10	Fermi surface frequencies in indium	86
11	Apparent "modulation" of amplitudes in tin	89
12	Comparison of the angular range of frequencies in tin in the (100) plane	96
13	Magnetic breakdown orbits in tin near [001]	103
14	Comparison of the angular range of frequencies in tin in the (110) plane	108
15	Magnetic breakdown orbits in tin at [001]	112
16	Magnetic breakdown orbits in tin at [110]	115
17	Oscillation amplitudes used in breakdown fields analysis	123

## LIST OF FIGURES

<u>Figure</u>	<u>Description</u>	<u>Page</u>
1	Density of states in a magnetic field	4
2/	Block diagram of the electronic apparatus	15
3	Field factor as a function of magnetic field	20
4	Variation of the magnetic field with axial distance.	22
5	Low temperature apparatus	23
6	The sample holder	25
7	Oscillations as a function of reciprocal magnetic field	41
8	Fast Fourier transform	42
9	Slow Fourier transform	43
10	$\alpha_0/T$ as a function of T	50
11	Composite graph of all frequency branches observed in tin	56
12	Low frequency branches in the (100) plane of tin	62
13	High frequency branches in the $(\bar{1}00)$ plane of tin	63
14	Low frequency branches in the (110) plane of tin	65
15	High frequency branches in the (110) plane of tin	66
16	Frequency branches in the (001) plane of tin	68
17	$\beta_1^2$ orbit in the (100) plane of indium	83
18	Frequency branches in the (001) plane of indium	85

<u>Figure</u>	<u>Description</u>	<u>Page</u>
19	Model of the Fermi surface of tin	92
20	Orbits $\epsilon_1^3$ , $\epsilon_1^{5a}$ , and $\epsilon_1^6$ in the fourth zone	100
21	Magnetic breakdown orbits at [001]	105
22	Magnetic breakdown orbits at [110]	114
23	Model of the Fermi surface in indium	127

## CHAPTER 1

### INTRODUCTION

During the past twenty years, an intensive investigation of the size and shape of the Fermi surface has been carried out in order to better understand the electronic behaviour in metals, alloys, and semiconductors. Under certain conditions the quantum oscillations in the ultrasonic attenuation yield the same information as the more familiar de Haas-van Alphen effect. However for several years there has been growing evidence that some orbits are much more easily observed by one effect than the other. Consequently an investigation was undertaken, in a material well studied by the dHVA effect, to determine if further information on the Fermi surface could be extracted using ultrasonic attenuation. The material chosen was white tin, and in addition a preliminary study of indium was performed.

After a brief introduction to quantum oscillations and detailed equations for the ultrasonic attenuation, the new experimental results for Fermi surface frequencies and effective masses are presented and discussed in relation to other investigations. The appendices detail some basic crystallographic data and definitions.

## CHAPTER 2

### THEORETICAL BACKGROUND

---

#### 2.1 Introduction to the Fermi Surface

Each conduction electron in a metal occupies an allowed quantum state characterized by a wave vector and spin quantum number. If a free electron gas at the absolute zero of temperature is viewed in wavevector or  $k$ -space, the electrons fill quantum states of ever increasing energy until a particular value called the Fermi energy. Above this energy the states are unoccupied and the spherical boundary between filled and empty states is called the Fermi surface. In real metals, however, a periodic lattice potential is present which partitions wavevector space by a set of planes into regions called Brillouin zones. Along each plane there is an energy discontinuity associated with Bragg reflection of the electrons. To more easily study the Fermi surface, the second and higher Brillouin zones may be rearranged into a reduced zone representation in which the Fermi surface separates into a number of sheets.

The application of a magnetic field ( $H$ ) drastically alters the distribution of electrons. The allowed states become a discrete set of highly

degenerate, concentric cylinders (Landau, 1930) with a common axis (usually) parallel to the field. An example is shown in Fig. 1 for free electrons in a very large field. Both the cross-sectional areas (perpendicular to  $\underline{H}$ ) and the degeneracy of these Landau cylinders are proportional to  $\underline{H}$ . An increasing magnetic field causes the cylinders to expand, and the consequent variation in the density of states at the Fermi surface produces quantum oscillations in a number of properties, such as the susceptibility (de Haas-van Alphen effect), magnetostriction, magnetoresistance (Shubnikov-de Haas effect), and temperature (magnetothermal oscillations). The periodicity of these oscillations,  $\Delta(1/H)$ , is related to the Fermi surface by (Onsager, 1952)

$$\Delta\left(\frac{1}{H}\right) = \frac{2\pi e}{\hbar S_F} \quad (2.1)$$

where  $S_F$  represents an extremum value of cross-sectional area perpendicular to  $\underline{H}$  and bounded by the Fermi surface. One over-riding condition for quantum oscillations is the requirement that the energy separation between Landau levels,  $\hbar\omega_c$  ( $\omega_c =$  cyclotron frequency), be larger than the width of a level ( $\Delta E$ ) due to the finite lifetime of electron states ( $\tau$ ). From the uncertainly relation  $\Delta E = \hbar/\tau$  and consequently the relation  $\omega_c \tau > 1$  must be satisfied.

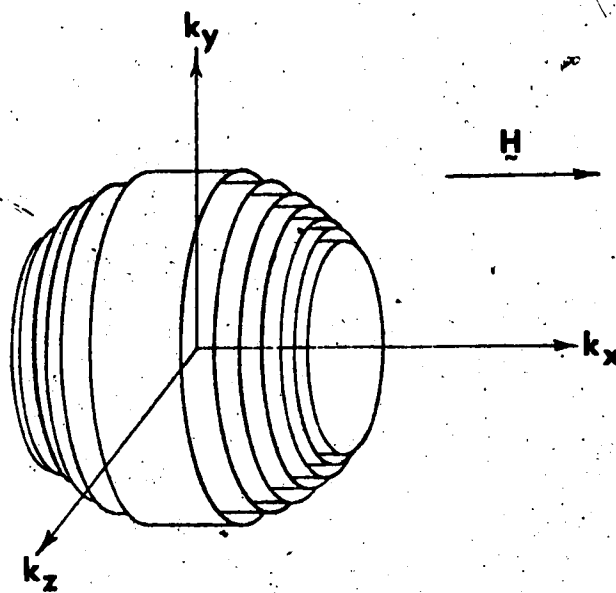


Fig. 1: Density of states for a free electron gas in a magnetic field. The only allowed states are on the Landau cylinders within the Fermi surface.



### The Fermi Surface (Blacknell and Wong, 1973)

offers a good general review of the oscillatory phenomena just mentioned, while a more detailed discussion of the de Haas-van Alphen (dHvA) effect can be found in the Simon Fraser Summer School lectures by Gold (1968).

### 2.2 Quantum Oscillations in the Ultrasonic Attenuation

The attenuation of sound waves by electrons also oscillates in amplitude when a changing magnetic field is present (provided  $\omega_c \tau > 1$ ). But unlike the previously mentioned oscillatory phenomena, there is an interaction between acoustic phonons and electrons which requires conservation of energy and momentum. This is discussed more fully in the following section where it is shown that under certain conditions the oscillation periodicity depends on a non-extremal cross-sectional area; however, in the experiments to be discussed these conditions were not satisfied and Eq. 2.1 remains valid.

In addition to determining the frequency of the oscillations, the temperature dependence of several oscillation amplitudes were measured. This dependence has the same form as in the dHvA effect and can be used to calculate the cyclotron effective masses.

6

Both Bhatia (1967) and Roberts (1968) have reviewed some of the oscillator attenuation effects caused by a magnetic field.

### 2.2.1 Consequences of the Conservation Requirement

When the conduction electrons suffer no collisions, the conservation of energy and momentum requirement allows only a certain group of electrons to interact with the acoustic phonons. Consider a free electron gas placed in a magnetic field along the z-direction; the energy of an electron on the  $n^{\text{th}}$  Landau level is

$$E_n = \left(n + \frac{1}{2}\right)\hbar\omega_c + \frac{\hbar^2 k_z^2}{2m} \quad (2.2)$$

where the cyclotron frequency  $\omega_c = eH/m$ . In magnetic fields greater than  $\sim 1$  KG the phonon energy,  $\hbar\omega_q$ , is much less than the Landau level separation,  $\hbar\omega_c$ ; thus the electron cannot jump to another level and the momentum and energy conservation relation is

$$\frac{\hbar k_z^2}{2m} + \hbar\omega_q = \frac{\hbar^2}{2m} [k_z + q_z]^2, \quad (2.3)$$

where  $\underline{q}$  is the phonon wavevector. Rearrangement of Eq. 2.3 yields

$$k_z^0 = \frac{mv_s}{\hbar \cos \theta} - \frac{q \cos \theta}{2} \quad (2.4)$$

where  $\theta$  is the angle between  $q$  and  $H$ ,  $v_s$  represents the sound velocity, and the  $^{\circ}$  attached to  $k_z$  emphasizes that the RHS is a constant for a particular sound wave. Eq. 2.4 can be given greater physical significance by replacing  $k_z^{\circ}$  with  $mv_{Fz}/\hbar$  ( $v_F$  = electron velocity) and neglecting  $q \cos \theta/2$  since  $mv_s/\hbar \cos \theta$  is much larger. Then

$$v_s = v_{Fz} \cos \theta \quad (2.5)$$

If instead Eq. 2.4 is divided by the wavevector of the Fermi surface:

$$\frac{k_z^{\circ}}{k_F} = \frac{v_s}{v_F \cos \theta} \quad (2.6)$$

Eq. 2.5 states that only those electrons which keep in phase with the sound wave can absorb energy from it; Eq. 2.6 demonstrates that  $k_z^{\circ}$  is very much smaller than  $k_F$  except when  $\theta \sim \pi/2$ , because in metals  $v_F/v_s > 200$  for most electrons.

If the electrons are limited to a free path length,  $l$ , an uncertainty is introduced into the conservation relations, and Eq. 2.4 is modified to (Reed and Brickwedde, 1971)

$$k_z^{\circ} \pm \Delta k_z = \left( \frac{mv_s}{\hbar \cos \theta} - \frac{q \cos \theta}{2} \right) \pm \frac{k_F}{\sqrt{2} q_z l} \quad (2.7)$$

where  $\Delta k_z = 1/2l_z$  and the  $\pm$  signs on each side of the equation are not related.

Eq. 2.7 can be separated into three regions characterized by the value of  $q_z l$ . When  $q_z l \gg v_F/v_s$ , the product  $\omega_q \tau = qlv_s/v_F \gg 1$  ( $\omega_q \tau \approx \hbar\omega_q/\Delta E$ ) and the uncertainty in  $k_z$  is very small,  $\Delta k_z \ll k_z^0$ . Consequently, in a changing magnetic field resonant absorption of the acoustic phonons occurs whenever electrons within  $\Delta k_z$  of  $k_z^0$  pass through the Fermi surface (Gurevich et al, 1961). These spike-like oscillations, called "giant quantum oscillations", have a periodicity determined by the Fermi surface cross-sectional area at the plane  $k_z^0$  - not the extremal area.

For a metal where  $q_z l \gg 1$  but  $\omega_q \tau \lesssim 1$ , the uncertainty  $\Delta k_z$  remains small compared to  $k_F$  although  $\Delta k_z \gtrsim k_z^0$  (Eq. 2.7). The electrons from the extremal orbit ( $k_z = 0$ ) contribute in phase to the attenuation and produce oscillations whose periodicity is given by Eq. 2.1. These are called "intermediate region oscillations" and are the type observed in the experiments to be discussed.

Finally, when  $q_z l \lesssim 1$ , the momentum and energy conservation restriction is completely relaxed ( $\Delta k_z \gtrsim k_F$  in Eq. 2.7) and all electrons at the Fermi surface may absorb energy from the sound wave.

The amplitude of these (de Haas-van Alphen-like) oscillations is expected to be small. Note that Eq. 2.7 predicts a change from intermediate region oscillations to de Haas-van Alphen-like oscillations as  $\theta$  approaches  $\pi/2$ .

### 2.2.2 Formula for the Oscillatory Attenuation

A detailed calculation of quantum oscillations in the attenuation has been reported by Reed and Brickwedde (1971). Although the analysis neglected the spin of the electrons, it extended the earlier work of Skobov (1961) and Liu and Tøxen (1965). The electrons at the  $j^{\text{th}}$  extremal cross-sectional area of sheet  $i$ ,  $S_{ij}$ , cause an attenuation given by

$$\alpha_{ij} = \alpha_{ij}(H \rightarrow 0) \left[ 1 + \frac{2\sqrt{2} q_z l k T m_{cj}^* v}{\phi_{ij} \hbar^3 (|S_i''(E_F, k_{zj})|)^{1/2}} \right] \cdot \left( \frac{2\pi}{\hbar e H} \right)^{1/2} \cdot \sum_{p=1}^{\infty} \frac{p^{1/2} \cos[(p\hbar S_{ij}/eH) - 2\pi p \gamma - \pi/4]}{\sinh[2\pi^2 p m_{cj}^* kT/\hbar e H]} \cdot \exp(-\pi p m_{cj}^*/eH\tau_j), \quad (2.8)$$

where  $m_{cj}^* = \hbar^2 (\partial S_{ij}/\partial E)/2\pi$  is the cyclotron effective mass at the extremal orbit  $j$ . Here  $\phi_{ij}$  is defined as  $\rho_{ij}(E_F, q, l, \hat{k}_z)$  when  $q_z l > 1$  and  $\rho_{ij}(E_F, q, l, \hat{k}_z)$  is the density of states for those electrons which can interact with the sound wave. When  $q_z l \leq 1$ ,  $\phi_{ij} = \sqrt{2} q_z l \cdot \rho_i(E_F)$  and  $\rho_i(E_F)$  includes the whole sheet  $i$ .

The factor  $\alpha_{ij}(H \rightarrow 0)$  is the zero field attenuation (e.g., see Pippard, 1955, 1960) and  $S_{ij}''(E_F, k_{zj}) = \partial^2 S_{ij}(E_F, k_{zj}) / \partial k_z^2$  where  $S_{ij}(E_F, k_{zj})$  is the area of cross-section at  $k_{zj}$ .

Eq. 2.8 can be rewritten to illustrate some important physical points:-

$$\alpha_{ij} = \alpha_{ij}(H \rightarrow 0) \left( 1 + \frac{c\sqrt{2} \alpha_z l}{\sqrt{H} \phi_{ij}} \cdot \frac{T}{(|S_{ij}''(E_F, k_{zj})|)^{1/2}} \sum_{p=1}^{\infty} p^{1/2} \frac{\cos[2\pi p \frac{f}{H} - 2\pi p \gamma - \frac{\pi}{4}]}{\sinh[2\pi^2 p \frac{kT}{\hbar\omega_c}]} \cdot e^{-p\pi/\omega_c \tau_j} \right) \quad (2.9)$$

where  $f = 1/\Delta(1/H)$ . The term  $(|S_{ij}''|)^{-1/2}$  gives the length of the Landau cylinder at the Fermi surface extremum which dominates the attenuation. The term,  $e^{-p\pi/\omega_c \tau_j}$ , describes how the oscillation amplitudes are damped due to collisions of the electrons with impurities. If a "Dingle temperature"  $T_D = \hbar/2\pi k\tau_j$  is defined and  $1/\sinh X_p$  ( $X_p = 2\pi^2 p kT/\hbar\omega_c$ ) is approximated with  $\exp(-X_p)$ , the two exponentials can be combined into  $\exp(-2\pi^2 p k(T+T_D)/\hbar\omega_c)$ . Thus the finite lifetime between collisions reduces the oscillation amplitude, when expressed as  $A_{ij} = \alpha_{ij}/T$ , in the same manner as a rise  $T_D$  in the temperature of the metal. Finally, the thermal damping of  $\alpha_{ij}$  is described by  $X_p/\sinh X_p$  which multiplies each term of the summation, but there

does not appear to be any simple physical argument that gives this expression. However the thermal damping is expected to depend on  $kT/\hbar\omega_c$ , which compares the diffuseness of the Fermi surface,  $\sim kT$ , with the separation of the Landau levels,  $\hbar\omega_c$ .

### 2.2.3 Calculation of Effective Masses and Dingle Temperatures

The cyclotron effective mass ( $m_{cj}^*$ ) can be calculated from the temperature dependence of the amplitude of the oscillations. When only the  $p = 1$  term of Eq. 2.9 is retained and  $\sinh X_1$  approximated by  $\exp(X_1)$ , the logarithm of the oscillation amplitude ( $\alpha_{ij}^0$ ) divided by  $T$ ,  $\ln(\alpha_{ij}^0/T)$ , has a linear dependence on  $T$  with slope  $b = -2\pi^2 k/\hbar\omega_c$ . Consequently  $m_{cj}^*$  can be calculated from

$$m_{cj}^* = b \times H_0 \times \frac{\hbar e}{2\pi^2 k} \quad (2.10)$$

where  $H_0$  represents the particular value of field at which  $b$  was measured. The neglect of higher order terms in the summation ( $p > 1$ ) is justified because  $\exp(\pi p/\omega_c \tau)/\sinh X_p$  which multiplies each harmonic greatly reduces their amplitudes, and experimentally the harmonics are seldom detected. Note that the mean free path ( $\ell$ ) has been treated as a temperature

independent factor. This is justified for  $T < 5$  K where impurities dominate the scattering of electrons.

After calculation of  $m_{cj}^*$  the Dingle temperature ( $T_D$ ) is obtained from the slope of  $\ln(H^2 \alpha_{ij}^0 \sinh X_1)$  versus  $1/H$  which has a linear dependence (when  $T$  is constant).

### 2.3 Introduction to Magnetic Breakdown

The phenomenon of magnetic breakdown (Cohen and Falicov, 1961) results from the finite probability that an electron will tunnel from one Fermi surface sheet to an adjacent one when they are separated by a small forbidden region in  $k$ -space. Usually the Brillouin zone boundary is the cause of the small forbidden region.

In large magnetic fields electrons travel on tightly curved trajectories in real space whose radii are proportional to  $1/H$ ; consequently the condition for Bragg reflection is satisfied for only a short interval of time and the probability of break-through may become quite large (Stark and Falicov, 1967).

The probability that an electron will tunnel through a forbidden region,  $k_g$ , is (Chambers, 1966)

$$P = e^{-H_0/H} \quad (2.11)$$

where



$$H_0 = \frac{\pi \hbar}{2e} \sqrt{\frac{k_g^3}{a+b}} \quad (2.12)$$

In Eq. 2.12  $1/a$  and  $1/b$  are the radii of curvature of the two Fermi surface sheets at the point of funneling.

## CHAPTER 3

### EXPERIMENTAL APPARATUS

Extremal Fermi surface areas and rates of change with energy were determined by measuring the variation in the ultrasonic attenuation as a function of magnetic field. To obtain long electron mean free paths, all experiments were performed from 4.2 K down to the lowest attainable temperature of 1.3 K; a superconducting magnet produced fields to 88 kilogauss. Pure longitudinal sound waves between 170 and 430 MHz were generated by 1/4 inch, X-cut quartz transducers operating at odd harmonics of their 10 MHz fundamental resonant frequency. The attenuation of these waves was measured by detecting the variation in amplitude of the first echo transmitted through the sample.

#### 3.1 Electronic Apparatus

A block diagram of the electronic apparatus is shown in Fig. 2. The transmitter, and the mixer and if amplifier of the receiver, were housed in a single commercial unit incorporating a main frame with plug-in units to cover different frequency ranges (Matec, 1970). The transmitter generated  $\sim 0.5 \mu\text{s}$  pulses of the carrier wave with a 100 V amplitude and a pulse repetition rate of approximately one ms. Stub tuners matched

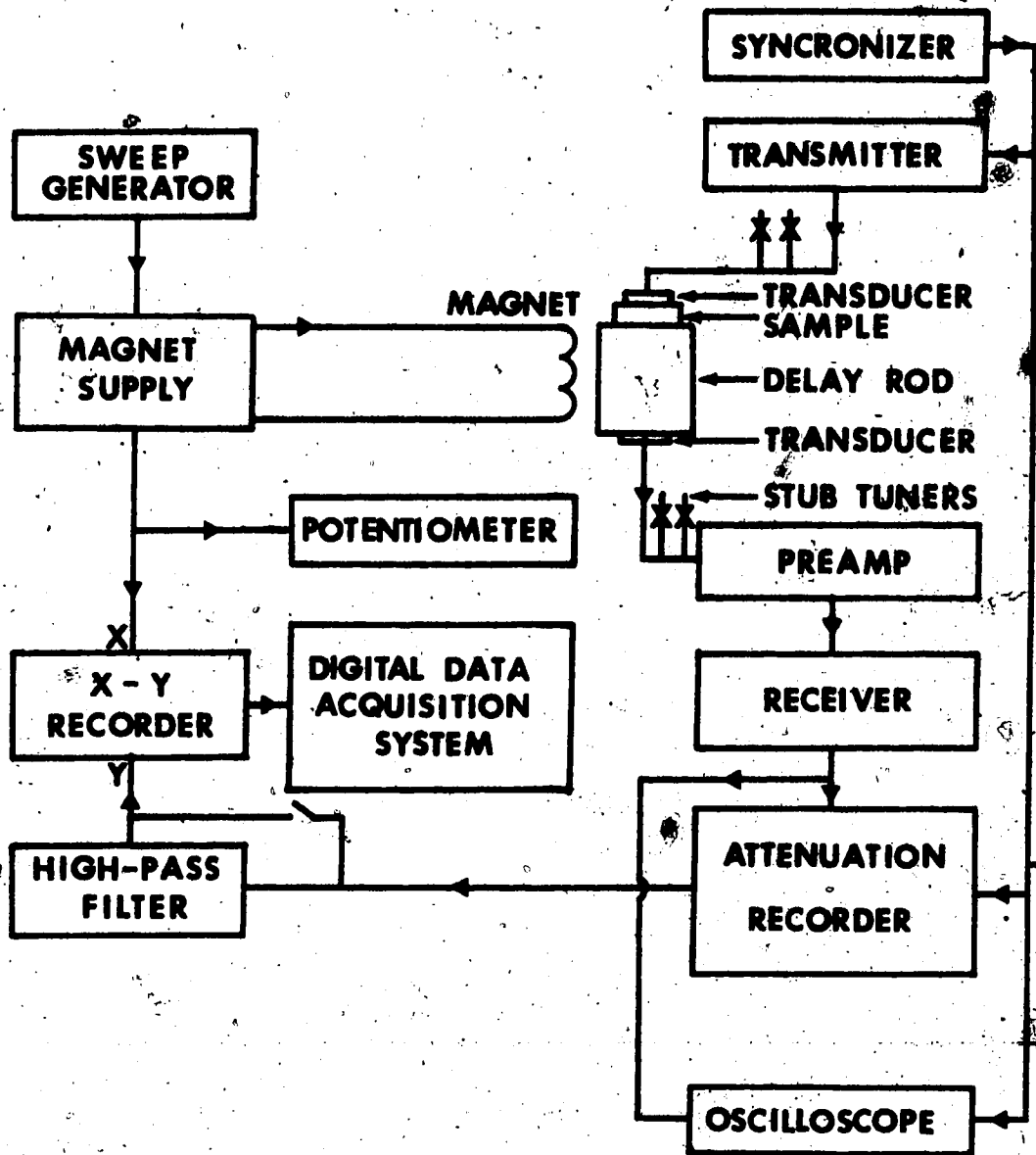


Fig. 2: Block diagram of the electronic apparatus.

the transmitting and receiving transducers to their respective 50 ohm coaxial cables. Although separate transmitting and receiving transducers helped to

isolate the receiver from the transmitter driving pulse, enough rf energy leaked through to paralyze the receiver for  $\sim 2 \mu\text{s}$ . Therefore a Z-cut quartz delay rod of one cm length was bonded between the sample and receiving transducer to delay the first echo long enough for the receiver to recover.

A low noise broadband preamplifier (Hewlett Packard, 1971) increased the signal-to-noise ratio (S/N) by 15 db when placed before the mixer. This improvement allowed the use of higher ultrasonic frequencies which increased the oscillation amplitude of the attenuation,  $\alpha_0$  (see Eq. 2.8).

The echo train was fed from the if amplifier into a Matec Model 2470 automatic attenuation recorder. Owing to the large attenuation in the sample at high frequencies, only the first echo could be detected; therefore the attenuation recorder logarithmically amplified the peak height of this echo and compared it to a d.c. voltage. After box-car integration, the output was displayed on the Y-axis of an X-Y recorder in db. Two modifications were made to the attenuation recorder: (1) the sensitivity was doubled, and (2) the meter displaying attenuation was bypassed because its

coil filtered out the higher frequency oscillations and increased the noise level.

Early experiments showed the need for high pass filtering of the integrator output. First, in addition to the oscillations in attenuation there was a monotonic variation with field; suppression of this non-oscillatory part stopped the pen of the X-Y recorder from drifting off scale. Secondly, three Fermi surface orbits ( $\tau_2^1$ ,  $\epsilon_3^2$ ,  $\pi_2^2$ ) produced oscillations large enough to require decreasing the sensitivity of the recorder. These oscillations had the lowest frequencies in the field sweep ranges of interest; thus the high-pass filter could effectively attenuate them while maintaining maximum sensitivity at the higher frequencies.

The 90 kilogauss niobium-titanium superconducting magnet (Ferranti Packard, 1970) was driven by a Hewlett Packard Model 6260A 100 ampere programmable power supply. The magnetic field was determined by accurate measurement of the voltage across a 5 milliohm resistor placed in series with the current. This voltage also drove the X axis of the recorder. A standard analog integrator circuit swept the magnet current linearly with time within a preset range. Although circuits are available which can drive the power supply to sweep  $1/H$  approximately linearly with time, accurate linearity is quite difficult to obtain.

Consequently, it was decided to perform the inversion digitally by computer.

The digital data acquisition system, borrowed from the Killam Earth Sciences group at this university, consisted of a highly accurate three channel analog-to-digital converter (less than  $\pm 0.03\%$  differential error) and a write-only seven track tape drive. Two of the channels were connected to the wipers of retransmitting slidewire potentiometers on the X and Y arms of the X-Y recorder. The non-linearity of these potentiometers was less than  $.15\%$ . During a magnetic field sweep, the pen position was recorded every 0.45 seconds or about 0.015 inch. The use of this digital data collection system, coupled with the powerful technique of Fourier analysis, substantially increased the sensitivity and selectivity of the apparatus. Oscillations of amplitude 0.05 inches on the 10 inch  $\times$  15 inch X-Y recorder paper could be detected in the presence of several other frequencies 200 times larger in amplitude, provided the background noise level was less at the frequency of interest.

### 3.2 Calibration of the Magnet

Since the magnetic field was determined indirectly by measurement of the power supply current,

precautions had to be taken to ensure that all current passed through the solenoid. This magnet was fitted with a mechanically operated switch which when 'off' was of infinite resistance. Other persistent switch designs often utilize a superconducting wire; however, the finite resistance of the wire in the normal state allows a significant current to bypass the field windings.

The magnet was calibrated by nuclear magnetic resonance of  $\text{Al}^{27}$  using apparatus borrowed from Dr. Hughes of this department. Seven turns of #24 AWG copper wire wrapped around a  $3\frac{1}{2}$  mm  $\times$  5 mm cylinder of powdered Al formed the low temperature probe. At the same time the magnetic field was determined to  $\pm 0.01\%$  by NMR, a potentiometer measured the voltage across the 5 milliohm resistor to the same accuracy. Dividing this voltage into the corresponding field yielded a field factor, in KG/mV, whose largest error arose from temperature drifts of the resistor and of the potentiometer standard cell. The field factor was constant to within  $\pm 0.06\%$  for both increasing and decreasing fields, between 28 and 75 KG, that were measured on three separate occasions. This data is shown graphically in Fig. 3 after subtraction of the Knight shift (0.162%). Although the NMR apparatus would not operate above  $\sim 75$  KG, there is no reason to doubt the accuracy

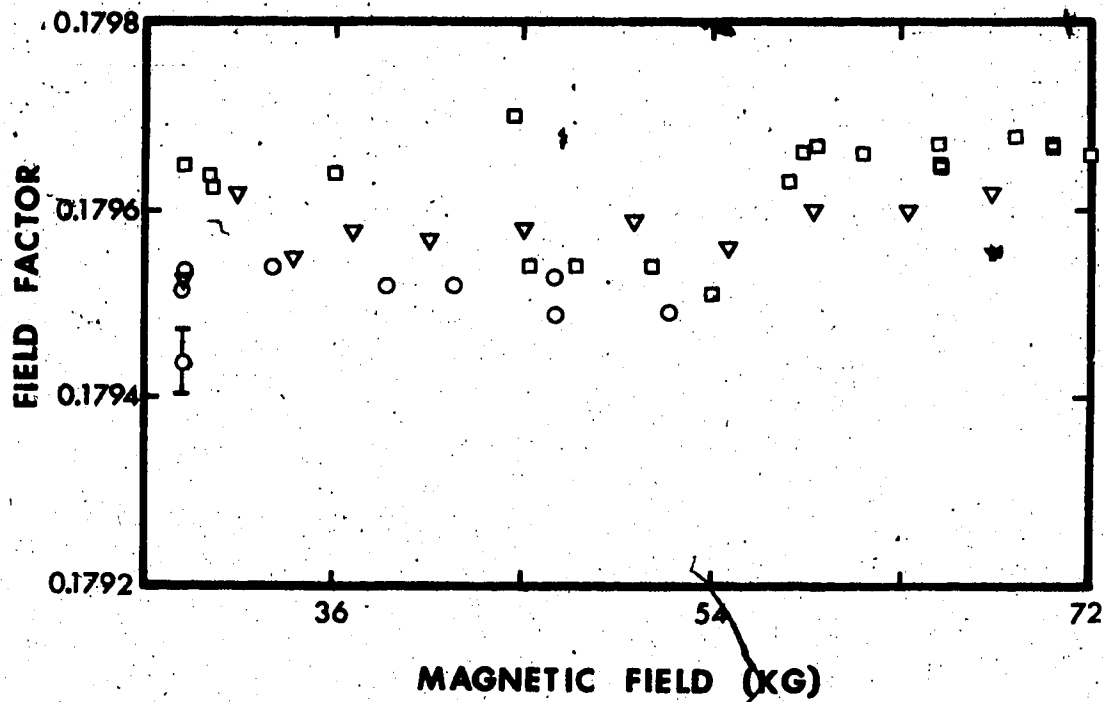


Fig. 3: Plot of the magnet's field factor as a function of magnetic field to illustrate its constancy. The data is derived from NMR measurements and the constant Knight shift has been subtracted from the data.



of the field factor at higher fields.

Due to space limitations, the sample could not be placed at the exact midpoint of the magnet bore;

however, it was always within 8 mm of the centre.

In this distance along the solenoid axis the field decreased less than 0.03%, as shown in Fig. 4, and the field change in the radial direction will be less.

### 3.3 Cryostat

In Fig. 5 is shown the low temperature apparatus. The stainless steel magnet dewar was of conventional design employing a liquid nitrogen shield. An insert capable of being pumped to 1.2 torr fitted inside the  $\frac{1}{8}$  inch magnet bore. The sample was initially immersed in a litre of liquid helium, and could be held at 1.4 K for about three hours before the insert had to be refilled through a needle valve. This particular design of insert, although having limited thermal anchoring to the external 4.2 K helium bath, allowed the sample holder to be removed and replaced without warming the cryostat. As discussed in Sec. 3.5, transducer bonds often crack when cooled to helium temperatures. A quick and simple removal procedure was necessary since the bonds must be repaired or remade at room temperature.

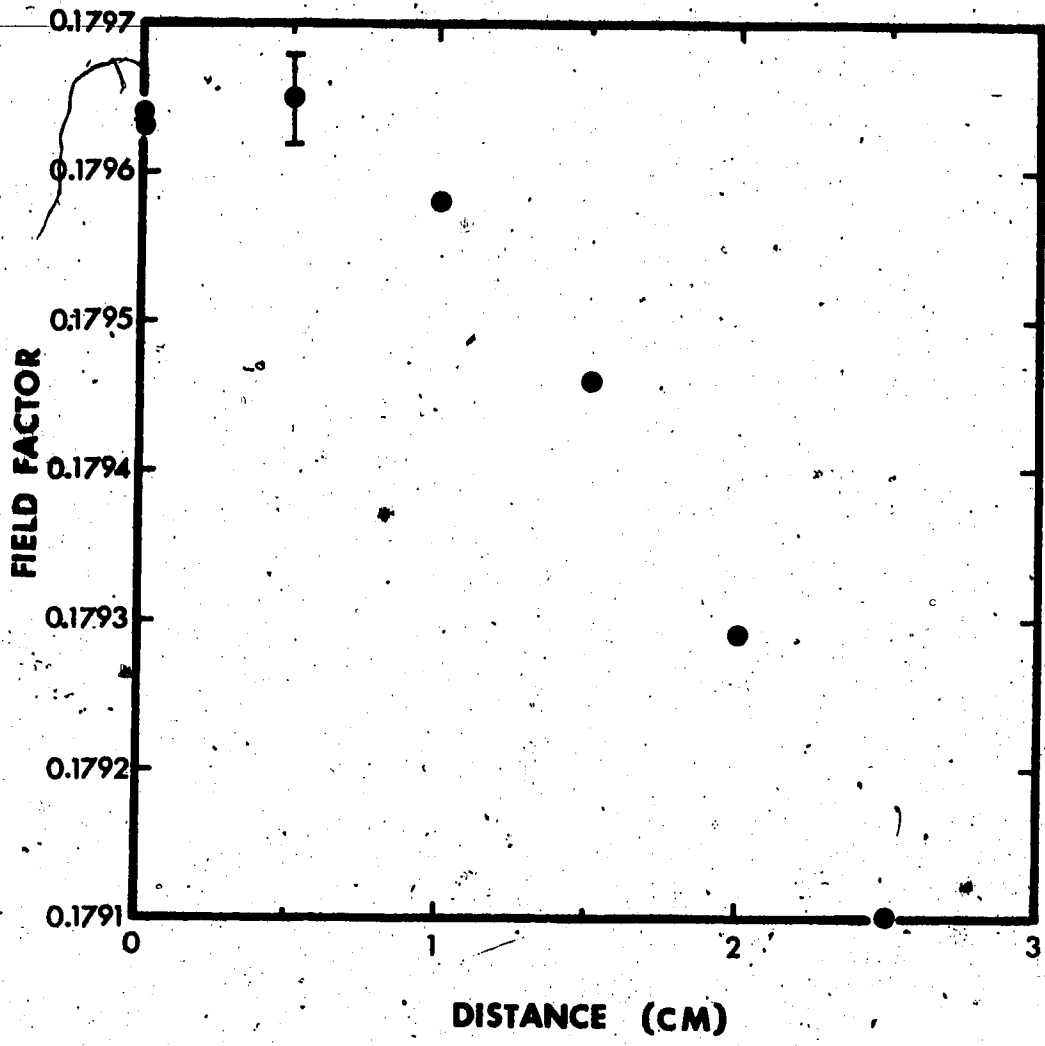


Fig. 4: Variation of the magnet's field with axial distance from the centre. The data points are from NMR measurements

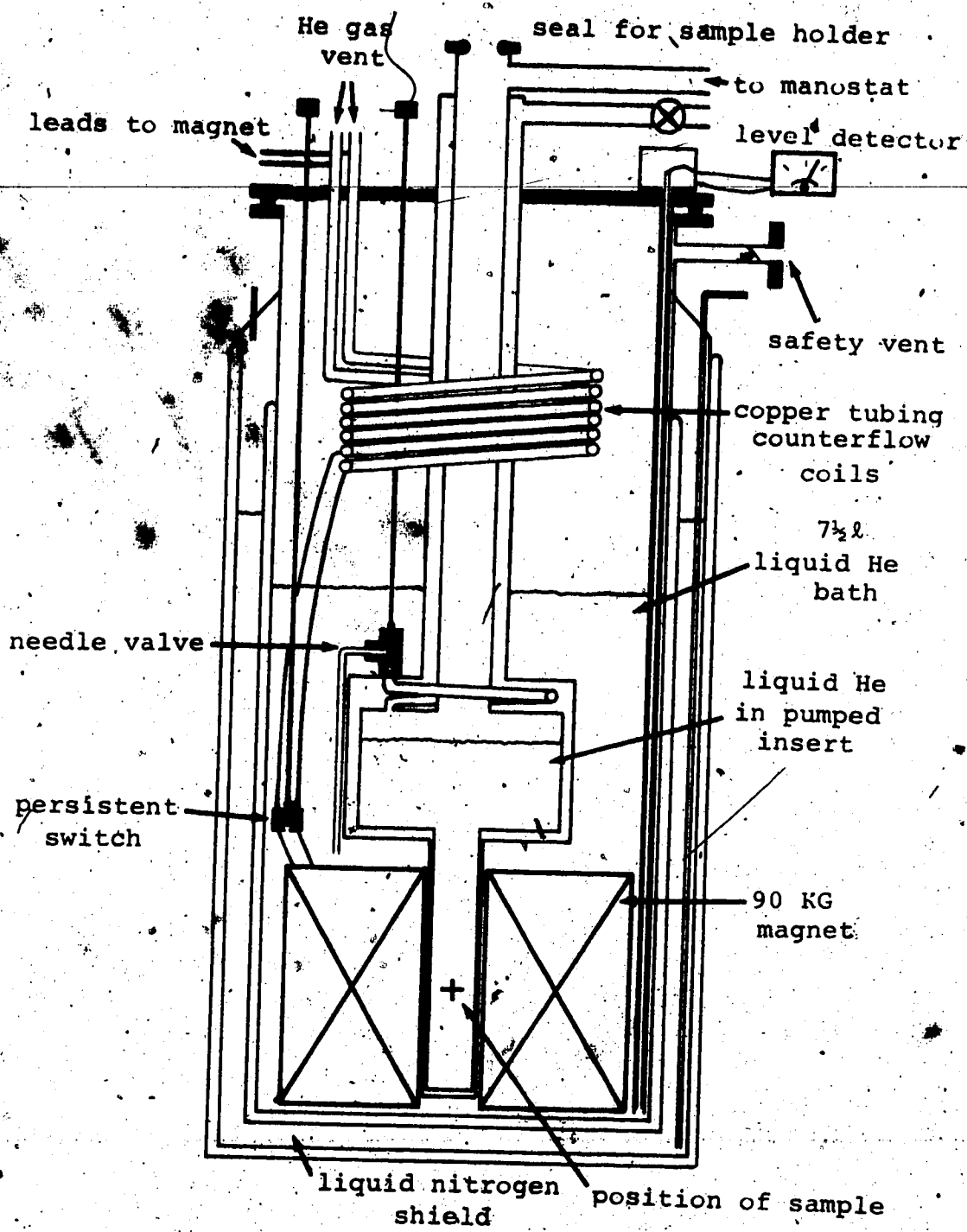


Fig. 5: Low temperature apparatus consisting of the stainless steel cryostat, magnet, and pumped insert.

To monitor the depth of both the liquid nitrogen precoolant and the liquid helium, a simple level detector was constructed utilizing the linear relation between the length of coaxial capacitor immersed in the liquid and its capacitance (Vrba, 1971).

### 3.4 Sample Holder

The sample holder, shown in Fig. 6, was designed to rotate the specimen in two perpendicular directions. First, the sound wavevector  $\underline{q}$  (which was along a particular crystallographic axis) had to rotate from a position parallel to the magnetic field to one perpendicular to  $H$ . Secondly, the sample had to rotate about the axis defined by  $\underline{q}$ .

A brass sphere 0.98 inch in diameter was fabricated with a cylindrical space at the centre, 0.75 inch in diameter and 0.41 inch long. The sphere was held by two small brass screws acting as axles such that the sphere rotated about an axis perpendicular to the axis of the cylindrical cavity. In addition the sphere formed one end of a pulley arrangement. A drum of the same diameter at the room temperature end was driven by a 5:1 reduction worm gear. Non-magnetic wire wrapped around and secured to grooves in both sphere and drum provided a non-slip link, while a strong beryllium-copper spring joining the wire ends relieved

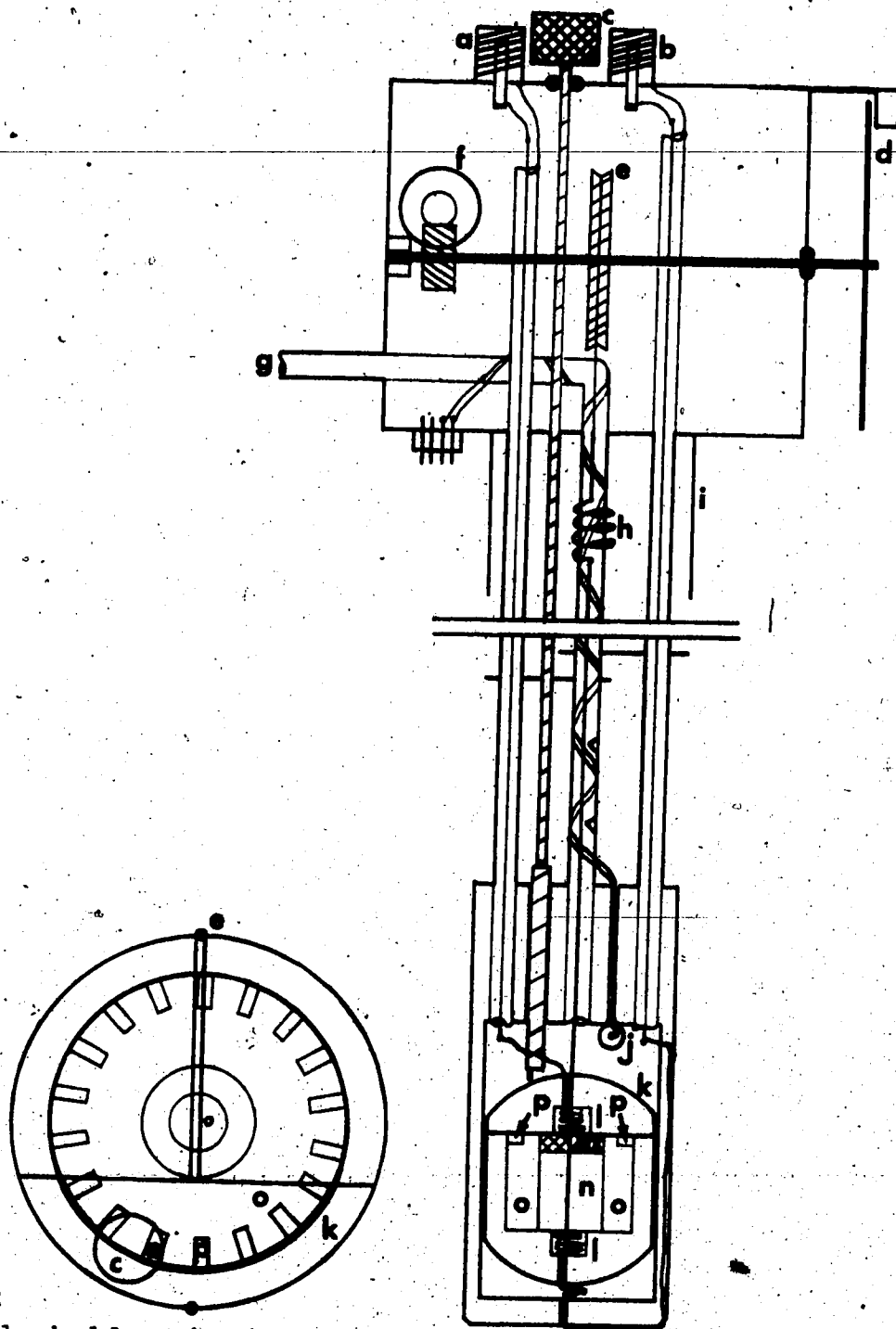


Fig. 6:

Sample holder showing in enlargement a top view of the sphere (not to scale): (a) and (b) transducer coaxial cables; (c) offset pin arrangement; (d) sample position dial; (e) drum and pulley wire; (f) worm gear; (g) to precision pressure gauge; (h) spring; (i) part of insert seal; (j) carbon resistor thermometer; (k) brass sphere; (l) transducer-coaxial cable terminal; (m) sample; (n) delay rod; (o) brass collar; (p) milled grooves

stresses due to thermal contractions. The relative position of the sphere was read from a dial rigidly fixed to the drum axle and calibrated during each experiment using the symmetry of the Fermi surface. The pulley arrangement provided about  $100^\circ$  movement in the first plane.

A cylindrical brass collar fitting into the cylindrical cavity and turned by a gear provide rotation in the second direction. The sample and delay rod assembly was held by silicone vacuum grease in a hole through the centre of the collar and parallel to its axis. One end of the collar had grooves milled every  $20^\circ$  to form a gear. With the collar (and thus  $q$ ) axis vertical, an offset pin arrangement operated from room temperature could be lowered a small distance to engage one of the grooves. Rotating the drive shaft from the room temperature end caused the pin to describe a short radius arc that in turn rotated the collar up to  $20^\circ$ . The shaft was then raised, rotated back to its initial position, and lowered enough to have the pin engage the next groove.

The ability to rotate the sample about  $q$  allowed alignment of the crystal at helium temperatures by using the symmetry of the Fermi surface. The accuracy of this alignment was about  $\pm 3^\circ$ . In early experiments orientation was done at room temperature but this

proved too inaccurate. A further advantage of the gear arrangement was the ability to rotate the sample to one of the other principal planes without warming it from 4 K.

The high voltage driving pulses from the transmitter and the return signal were carried on regular RG 174/U coaxial cable to the low temperature end of the sample holder. The external plastic cover had been removed to allow more efficient heat exchange between the helium gas and the outer conductor, while the #36 AWG wire connecting the inner coax conductor to the transducer provided thermal isolation of the sample.

The temperature of the specimen was obtained by measuring the vapour pressure above the helium bath using a Texas Instruments precision pressure gauge. To indicate when the pot was empty, and as an independent check, a carbon resistance thermometer was also used. The temperature measurement was accurate to  $\pm 5$  mK.

### 3.5 Transducer Bonds

The differential thermal contraction between quartz transducers and metallic crystals has always caused severe bonding problems, to the extent that there is no single bond material that works

successfully on all metals. The best of several bonding agents tested was Dow Corning high vacuum silicone grease. To improve the bonding success rate, thin indium foil was placed between the transducer and sample to relieve the stresses induced by cooling (Simpson, private communication). But the increased number of interfaces (transducer-grease-foil-grease-sample) resulted in significantly less ultrasonic power being transmitted into the sample. Fortunately a thin film of indium evaporated onto the transducer prior to bonding worked just as well without decreasing the received echo height. In addition, transducer (indium film)-sample-(indium film) delay rod-transducer structures could be cooled to 4 K several times without failure provided that: (1) the grease bonds were very thin, (2) they were precooled quickly in liquid nitrogen, and (3) the final cooling to helium temperatures took less than about two hours.

To produce thin bonds, the transducer (or sample) was placed on a blank quartz delay rod (which has a mirror smooth flat surface) over a small amount of grease. After most of the grease had been squeezed out, the transducer was carefully slid off the rod onto the surface to which it was to be bonded without additional grease.



Another bonding method that is often successful and can be thermally cycled almost indefinitely uses indium films evaporated onto each surface (Perz and Roger, 1971). The films are then fused together in a press heated to just below the indium melting point (156.6°C). Although this method worked well on a tin crystal with the [001] axis perpendicular to the surface, several attempts on a [110] crystal failed.

## CHAPTER 4

### SAMPLE PREPARATION

---

Three single crystals of tin were used in this series of experiments. The method of preparation is described in Sec. 4.1.1 and an estimate of the electronic mean free path ( $\ell$ ) is given in Sec. 4.1.2. Similarly, the preparation of the indium crystal and its  $\ell$  are discussed in Sec. 4.2.1 and Sec. 4.2.2, respectively.

#### 4.1 Tin Samples

##### 4.1.1 Preparation of Tin Samples

Three single crystals of 99.9999% pure tin were produced from the same ingot using the method of Bridgman (1925). These samples, made in the form of short cylinders 8 mm in diameter by  $\sqrt{2}\frac{1}{2}$  mm thick, had either the [110] or [100] normal to the flat surfaces. In this thesis square brackets denote a particular crystallographic axis. To ensure that the specimen grew with the desired orientation, a seed crystal was first oriented by X-ray Laue back reflection<sup>o</sup> and a mould was then built around one end. Two pieces of plate glass  $\sqrt{1/2}$  inch square were used for the top and bottom of the mould, while glass tubing, one cm

in diameter,  $2\frac{1}{2}$  mm long and halved lengthwise served as walls. The seed end projected between the tubing halves on one side and the nozzle of a small glass funnel on the other. A release agent (Miller-Stephenson Chemical Co., 1970) prevented the metal from sticking to the glass and plaster of paris held the entire structure together.

After tin was loaded into the funnel, the mould was heated in a crystal growing furnace built by Mr. B. Stackhouse. Thermocouples embedded in the plaster provided continuous monitoring of the temperature. When these indicated that the tin in the funnel had melted, helium gas forced the metal into the mould cavity. The temperature was slowly increased until the upper part (only!) of the seed was also molten; then a motor raised the furnace at  $\approx 4$  cm per hour. Afterwards the mould could be disassembled by submerging it in water. Any deviation of the crystal axis from perpendicularity (to the flat surface) was determined using the Laue method, and corrected when the two flat faces were planed by a Metals Research "Servomet" spark cutter.

Some physical and crystallographic data for the three samples are given in Table 1.

Table 1

Physical and crystallographic data for the three tin specimens, including the length  $L$  of each crystal, and the angle  $\theta$  between the normal to the surface and the crystal axis,  $C$ .

Crystal	$C$	$\theta$	$L$ in mm
Sn 1	[110]	$2^\circ$	2.184
Sn 2	[110]	$1\frac{1}{2}^\circ$	2.170
Sn 3	[100]	$\frac{1}{2}^\circ$	2.096

#### 4.1.2 Electronic Mean Free Path in Tin

The ingot used in the manufacture of these single crystals had a resistivity ratio  $R = \rho_{293}/\rho_4$  of  $\sim 22,000$  (Woods, private communication) which had been determined by the eddy-current technique.

Chambers (1952) has shown that

$$\ell = (9.5 \times 10^{10} \rho_4)^{-1} \text{ cm} \quad (4.1)$$

which, using  $\rho_{293} = 11.0 \times 10^{-6} \Omega\text{-cm}$  (Handbook of Chemistry and Physics), yields  $\ell = 0.02 \text{ cm}$ .

### 4.2 Indium Sample

#### 4.2.1 Preparation of Indium Sample

A small sample 2.23 mm in length was spark cut from a large indium crystal which had twinned. The [100] axis was within  $2^\circ$  of the normal to the flat surfaces. Although this small crystal twinned during thermal cycling, it was possible to unambiguously assign the measured frequencies as discussed in Sec. 6.4.

A serious difficulty prevented the preparation of an indium single crystal. Although a seed supplied by Dr. Woods produced typical Laue diffraction patterns, four crystals grown as described in Sec. 4.1.1 (one crystal not seeded) showed only two or three possible

Laue spots. Yet visually the blaze planes were easily observable. Spark planing and etching with dilute nitric acid of various concentrations made no improvement.

#### 4.2.2 Electronic Mean Free Path in Indium

The ingot from which the large twinned crystal was prepared had a resistivity ratio of  $\sim 22,000$  (Woods, private communication). This represents an electron mean free path of roughly 0.02 cm (using Eq. 4.1).

Geometric oscillations in the ultrasonic attenuation (Bhatia, 1967) were observed at 1.9 K using a frequency of 170 MHz. These oscillations give an estimate of the mean free path of the orbit producing the oscillations (Rayne and Chandrasekhar, 1962),

$$\ell = \pi \left( n + \frac{1}{2} \right) \lambda \quad (4.2)$$

$\lambda$  is the wavelength of sound and  $n$  represents the number of oscillations seen. For this orbit  $\ell \sim 0.07$  cm since experimentally  $n = 17$  oscillations.

A difference between the two estimates of  $\ell$  is expected because the eddy current method measures an average  $\ell$  while geometric oscillations measure  $\ell$  for a particular cyclotron orbit.

## CHAPTER 5

### COMPUTATIONAL TECHNIQUE

---

The different frequencies comprising a complicated waveform can be determined by three basic methods: comparison, elimination, or transformation. The simplest comparison technique is by inspection. In a slightly more sophisticated form, voltages from several signal generators can be mixed in an attempt to synthesize the waveform. The elimination method utilizes a narrow band-pass filter to eliminate all but one (or two) of the frequencies. The measurements must then be repeated at different band-pass frequencies until all the frequencies have been detected. Lastly, the entire spectrum can be found immediately by means of the Fourier transform, using either analogue or digital techniques.

Fourier transformation from digitally recorded data was chosen as the most efficient means of analysis due to its comparatively greater speed, sensitivity, and selectivity; especially since a trace might contain 15 frequencies with a 200:1 range in amplitudes. The major drawback was not being able to calculate the transform during the experiment.

The transformation method has become even more powerful, in practical terms, since the introduction

of the fast Fourier transform (Cooley and Tukey, 1965) which requires much less computer time. However, it has two restrictions. For a wave sampled over some finite interval, the entire transformed spectrum is evaluated, but only at those frequencies having an integral number of oscillations in the interval considered. Also the wave must be sampled at  $N$  equal intervals where  $N$  is an integral power of 2 (e.g. 256, 512, 1024 etc.).

Briefly the method of analysis was as follows. The digital data acquisition system recorded the attenuation,  $\alpha(H)$ , and field on magnetic tape. A program run on the Computing Services IBM 360/67 computer inverted  $\alpha(H)$  to  $\alpha(1/H)$  in equal intervals of inverse field, automatically removed non-oscillatory background attenuation, and evaluated the fast Fourier transform. The inversion process to  $1/H$  and the background attenuation removal are discussed more fully in Sec. 5.1, while the extraction of frequencies and amplitudes from the transform is described in Sec. 5.2. An amplitude correction factor, calculated in Sec. 5.3, is necessary to prevent errors in the effective masses. The method used to obtain the masses is discussed in Sec. 5.4.

The main purpose of these experiments was to extract the frequencies and amplitudes of the



oscillations in the attenuation. This information is contained in the absolute value of the Fourier transform, since the phase of the transform relates the phase of the oscillations to the trace midpoint. Consequently, the term "Fourier transform" will refer to the absolute value of the transform unless specified otherwise.

## 5.1 Preparation of Data for Analysis

### 5.1.1 Inversion of the Magnetic Field

The attenuation was sampled approximately 1000 times in equal intervals of magnetic field, but the Fermi surface frequencies being analyzed are periodic in  $1/H$ . Consequently, a computer program was written to calculate 512 values (usually) of attenuation ( $\alpha_m$ ) at equal intervals in inverse field using linear interpolation.

### 5.1.2 Elimination of Non-oscillatory Background Attenuation

The zero of attenuation as recorded by the digital acquisition system was at the lower edge of the graph paper. Thus  $\alpha_m$  contained a large constant offset. Also, it varied monotonically with  $H$  when the high-pass filter was not used. These combined to

produce a substantial amplitude in the Fourier transform near zero frequency which swamped the Fermi surface spectrum. To eliminate this problem a straight line,  $\alpha' = b + m(1/H)$ , was generated and subtracted from  $\alpha_m$  using values of  $b$  and  $m$  calculated from an initial fast Fourier transform. A short analysis shows that the required value of  $b$  is just the real part of the transform at zero frequency divided by the length  $L$  of trace in inverse field:  $b = \text{Re}\{F(0)\}/L$ , and

$$m = \frac{2\pi \text{Im}\{F(\omega = \frac{2\pi}{L})\}}{L^2}$$

The final set of attenuation data  $\alpha(1/H) = \alpha_m - \alpha'$  gives the oscillatory change in the attenuation with respect to equal intervals of inverse field.

## 5.2 Determination of Oscillation Frequencies and Amplitudes

The spectrum of  $\alpha(1/H)$  could now be calculated, but a further modification is desirable. The Fourier transform of a waveform of finite length generates false frequency peaks (side lobes) which have the same form as Fraunhofer diffraction. They occur at regularly spaced (frequency) intervals and decrease in magnitude as  $1/|f-f_0|$ , with the first side lobe being 22% of the peak height.

To reduce these as much as possible, the attenuation data were multiplied by the "Tukey window" (Jenkins and Watts, 1968)

$$W(1/H) = 1 + \cos(f_1/H) \quad (5.1)$$

where  $f_1$  is chosen to make  $W = 0$  at each end of the trace. The window in effect amplitude modulates each frequency in such a manner that the upper and lower sidebands in the Fourier transform caused by the modulation cancel the side lobes. At the expense of roughly doubling the width of the main peak, the side lobes are reduced by an order of magnitude (to 2.7% for the first side lobe). The fast Fourier transform was calculated on the modified attenuation data to obtain the frequency spectrum up to that particular frequency which had three data points per oscillation.

The amplitude  $A$  of a simple sinusoidal wave with angular frequency  $\omega_0$ , and oscillating for a length of time  $L$ , can be determined from its Fourier transform through

$$A = \frac{2|F(\omega_0)|}{L} \quad (5.2)$$

The Fourier transform was plotted using Eq. 5.2 and  $L = 1/H$  to display the frequencies and amplitudes. A typical trace of the oscillatory attenuation in inverse field before multiplication of the Tukey

window is displayed in Fig. 7, while its frequency spectrum is shown in Fig. 8. If the frequency or amplitude of a particular peak was needed more precisely, the slow Fourier transform was calculated in a small frequency range including the peak, as shown in Fig. 9. Although Eq. 5.2 accurately describes the magnitude of a simple sinusoidal wave, an amplitude correction factor must be applied when the wave is of changing amplitude, such as the attenuation.

### 5.3 Correction Factor for the Oscillation Amplitude

Owing to the variation in amplitude of the oscillatory attenuation,  $\alpha_0$ , with field, Eq. 5.2 requires modification by an amplitude correction factor which is a function of temperature, effective mass, and the range of magnetic field. The correction was determined by calculating the Fourier transform of Eq. 2.8, the formula for the attenuation coefficient at one Fermi surface frequency. This is rewritten below after collecting all the field independent terms into four parameters and discarding the unimportant constant background attenuation. Also, only the leading term of Eq. 2.8 is retained since the harmonics were seldom detectable experimentally. Thus:

$$\alpha(y) = \frac{Ay^{\frac{1}{2}}}{\sinh By} \cos(\omega_0 y + \theta), \quad y_1 \leq y \leq y_2. \quad (5.3)$$

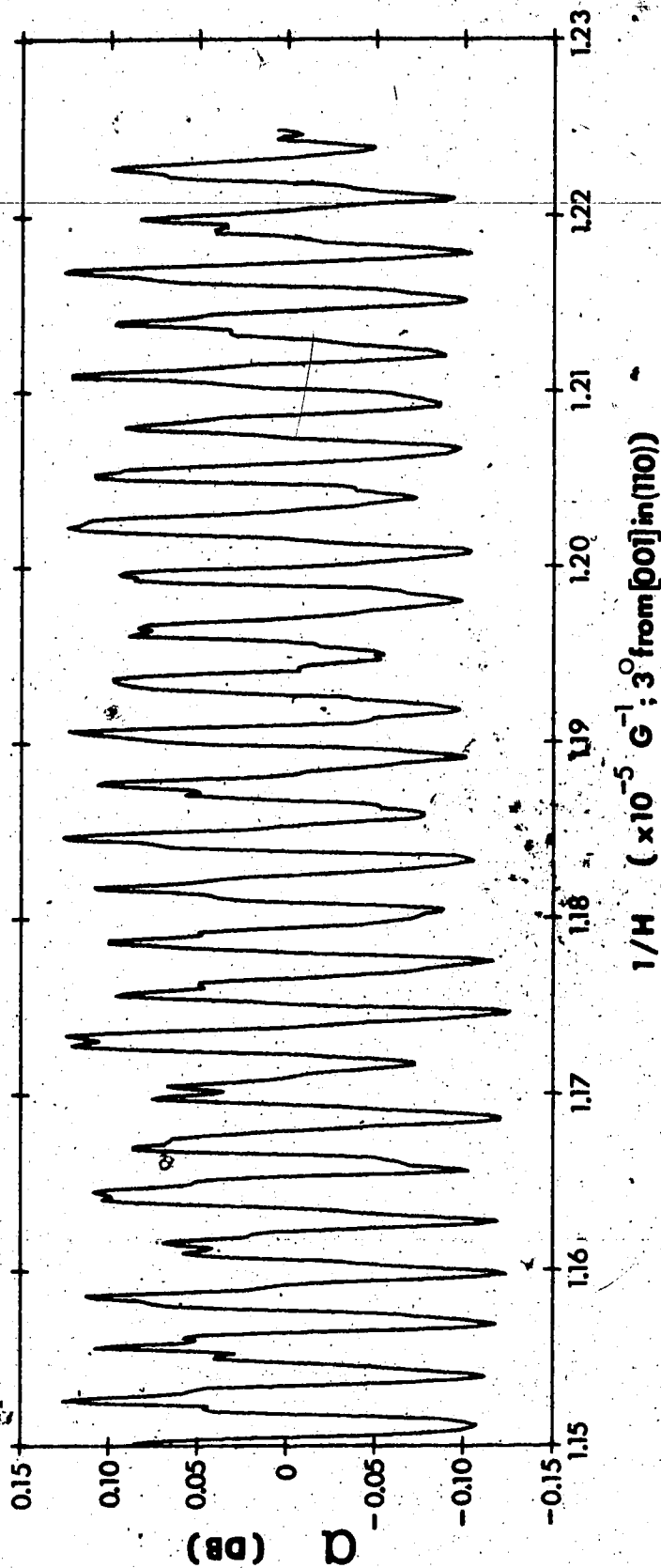


Fig. 7: Oscillation in the attenuation as a function of reciprocal magnetic field.

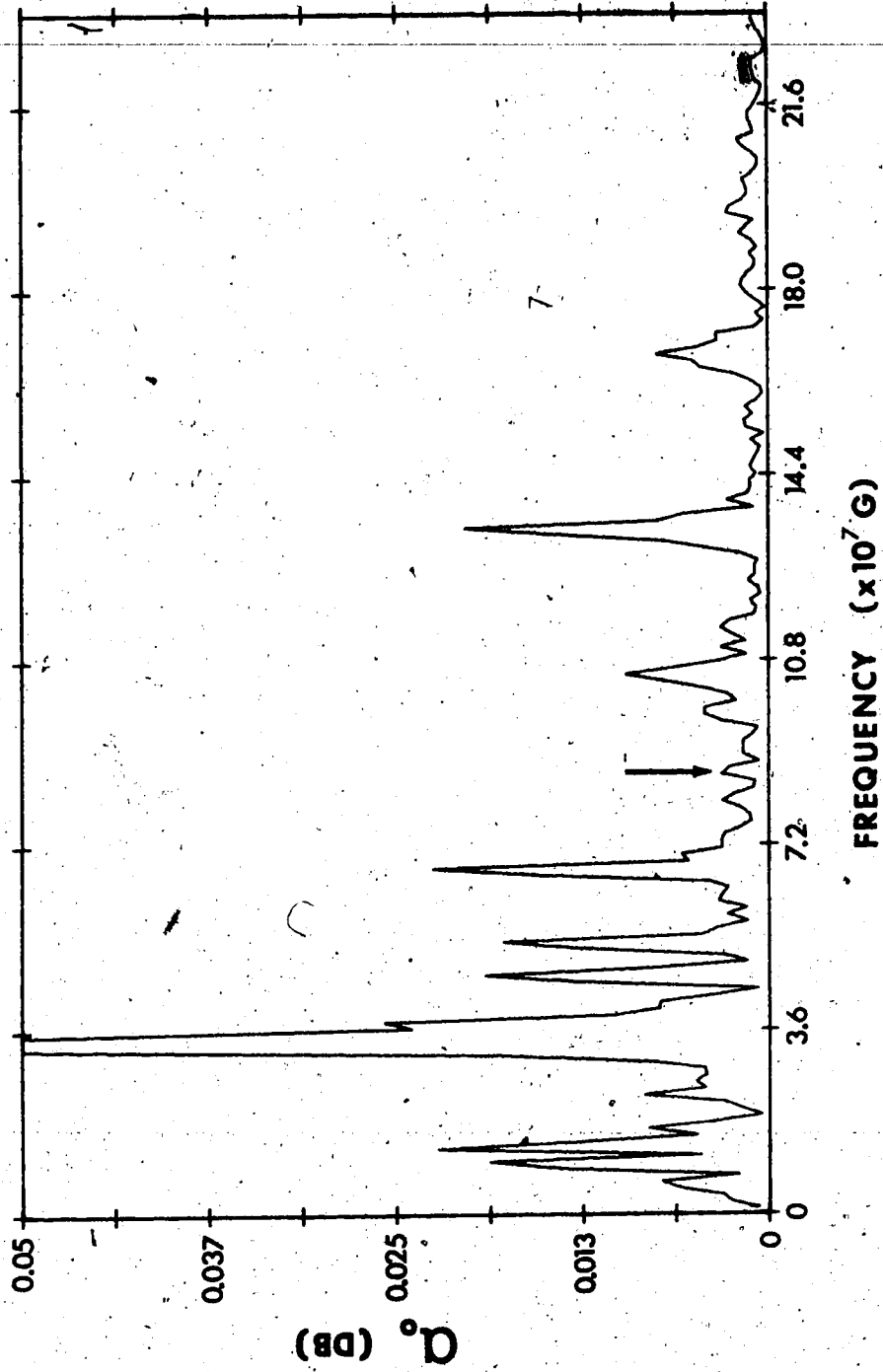


Fig. 8: Fast Fourier transform of the oscillations shown in Fig. 7 after application of the Tukey window.

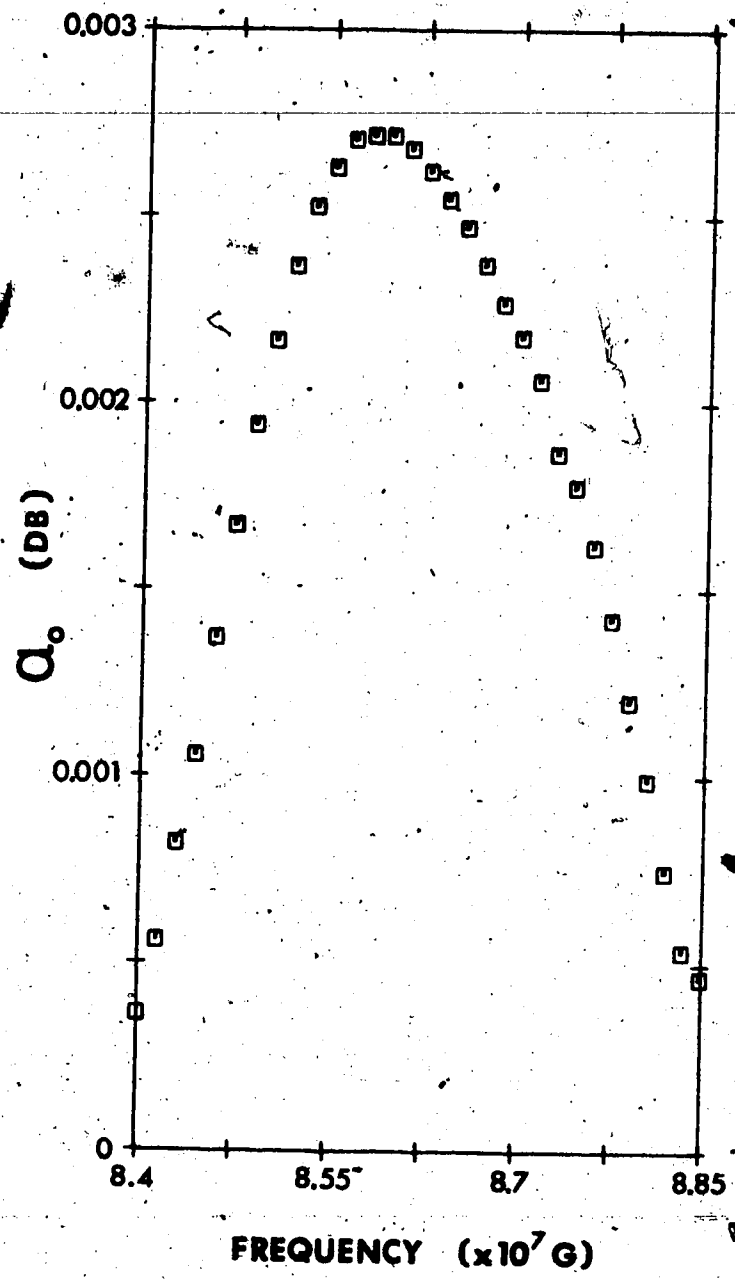


Fig. 9: Slow Fourier transform of the peak in Fig. 8 marked with an arrow.

The parameter A contains all the field independent factors of Eq. 2.8. in front of the summation sign,  $B = \cdot 2\pi^2 m_c^* kT / \hbar e$ , and  $y$  represents  $1/H$  in the sweep range  $y_1$  to  $y_2$ . The theoretical expression for the oscillation amplitude is  $\alpha_0(y) = y^2 A / \sinh By$ , and the terms determining the frequency and phase of the oscillations have been combined into  $\omega_0$  and  $\theta$ , respectively. The  $y^{1/2}$  term which appears in Eq. 5.3 will be neglected subsequently in order to keep the Fourier integrals reasonably simple. This will be justified later.

To make Eq. 5.3 more easily integrable, the  $1/\sinh By$  term was replaced by an infinite series (Gradshteyn et al, 1965):

$$0.5(\sinh By)^{-1} = e^{-By} + e^{-3By} + e^{-5By} + \dots, y > 0. \quad (5.4)$$

The oscillatory attenuation is now

$$\alpha(y) = Ae^{-By} \cos(\omega_0 y + \theta) + Ae^{-3By} \cos(\omega_0 y + \theta) + \dots \quad (5.5)$$

where the 0.5 from Eq. 5.4 has been absorbed into A. Two further simplifications consist of transforming the inverse field  $y$  into  $x = Y - y$  where  $Y = (y_1 + y_2) / 2$  is the midpoint of the field sweep range; the new (inverse) field  $x$  is swept from  $-X$  to  $+X$ . Also, the phase  $\theta$  does not affect the oscillation amplitude and



can be neglected. With these two simplifications the attenuation becomes

$$\alpha(x) = Ae^{-BY} [e^{-Bx} \cos \omega_0 x] + Ae^{-3BY} [e^{-3Bx} \cos \omega_0 x] + \dots, \quad -X \leq x \leq X \quad (5.6)$$

Next, since all experimental attenuation data were modified by the Tukey window  $W(x)$ , shown in Eq. 5.1, the theoretical expression for  $\alpha(x)$  must similarly be multiplied by  $W(x)$ . Now the transform integrals can be calculated. The real part of the transform evaluated at the frequency of oscillation  $\omega_0$  is

$$\text{Re}\{F(\omega_0)\} = \lim_{\omega \rightarrow \omega_0} \int_{-X}^X \alpha(x) \cdot W(x) \cdot \cos \omega x \, dx \quad (5.7)$$

where  $\alpha(x)$  is explicitly shown in Eq. 5.6.

The imaginary part of the transform is almost zero because the modified attenuation  $\alpha(x) \cdot W(x)$  is an even function (except for the small field dependence of the amplitude) and the Fourier transform of an even function is real. Thus the absolute value of the transform equals the real part to a very good approximation. After evaluation of the Fourier integral Eq. 5.7 yields

$$|F(\omega_0)| = AXe^{-BY} g(BX) + AXe^{-3BY} g(3BX) + AXe^{-5BY} g(5BX) + \dots \quad (5.8)$$

where the function

$$g(nBX) = \frac{\sinh(nBX)}{nBX} - \frac{nBX \sinh(nBX)}{(nBX)^2 + \frac{\pi^2}{4}}, \quad n = 1, 3, 5, \dots \quad (5.9)$$

The quantity which must finally be determined is the oscillation amplitude at the midpoint of the sweep range, which from Eq. 5.6 is

$$\alpha_o(0) = Ae^{-BY} + Ae^{-3BY} + Ae^{-5BY} + \dots \quad (5.10)$$

But each term in this series can be evaluated through rearrangement of Eq. 5.8. Finally, the corrected (midpoint) oscillation amplitude is

$$\alpha_o(0) = \frac{2|F(\omega_o)|}{(2X)} \left( \frac{e^{-BY} + e^{-3BY} + e^{-5BY} + \dots}{e^{-BY}g(BX) + e^{-3BY}g(3BX) + e^{-5BY}g(5BX) + \dots} \right) \quad (5.11)$$

The term in front of the square brackets gives the amplitude of a simple sinusoidal wave, while that within the brackets corrects for the  $1/\sinh By$  dependence. Eq. 5.11 will be used in the evaluation of effective masses, described in the following section.

As previously mentioned the factor  $y^{1/2}$  (i.e.  $H^{-1/2}$ ) was neglected in Eq. 5.3. Since this is only slowly varying compared to  $\sinh By$ , the correction factor will remain quite accurate. Furthermore, this approximation causes no error when amplitudes are compared using the same field sweep range. The effective masses will be

determined in this way by changing only the temperature between each sweep.

#### 5.4 Effective Mass Determination

Effective masses are determined by measuring the variation in the experimental oscillation amplitude as a function of temperature at one average field  $H_0$ . To show explicitly how the theoretical oscillation amplitude depends on the temperature, Eq. 2.8 is rewritten below but with the temperature independent terms collected into the constant C. It is assumed that the mean free path is essentially temperature independent below 4 K and can be included in C. Eq. 2.8, in this more compact form, is

$$\alpha_0 = \frac{CTm_C^*}{\sinh(Dm_C^*T/H_0)} \quad (5.12)$$

where, in terms of the variables introduced in the last section,  $C = A/T$  and  $D = 2\pi^2 k/\hbar e = B/m_C^*T$ .

Although only approximate, the standard method compares theoretical and experimental oscillation amplitudes by graphical techniques after linearizing Eq. 5.12. The linearization is achieved by the approximation

$$\exp(Dm_C^*T/H_0) \approx 2 \sinh(Dm_C^*T/H_0) \quad (5.13)$$

With some rearrangement Eq. 5.12 simplifies to

$$\ln(\alpha_o/T) = \ln 2m_c^*C - (Dm_c^*/H_o) \cdot T \quad (5.14)$$

By plotting the experimental  $\alpha_o/T$  vs  $T$  on semi-logarithmic graph paper,  $m_c^*$  can be determined easily from the slope, using Eq. 2.10.

Unfortunately, the approximation, Eq. 5.13, is quite inaccurate for small values of the argument,  $(Dm_c^*T/H_o)$ . This difficulty can be avoided by manipulating Eq. 5.12 into the form

$$\ln[(\alpha_o/T) \cdot \{1 - \exp(-2Dm_c^*TY)\}] = \ln(2m_c^*C) - (Dm_c^*Y) \cdot T \quad (5.15)$$

where  $H_o$  has been replaced by  $Y$ . It is the necessity of sweeping  $H$  to obtain oscillations which requires the constant inverse field ( $H_o^{-1}$ ) to be approximated. The correct value is the midpoint of the sweep range,  $Y$ , which may be substituted without error.

The LHS of Eq. 5.15 must now be determined using the formula for  $\alpha_o$ , Eq. 5.11, remembering  $Dm_c^*T = B$ . We finally obtain for the LHS,

$$\ln\left(\frac{\alpha_o}{T} (1 - e^{-2BY})\right) = \ln\left[\frac{2|F(\omega_o)|}{T(2X)} \left\{ \frac{e^{-BY}}{e^{-BY}g(BX) + e^{-3BY}g(3BX) + \dots} \right\}\right] \quad (5.16)$$

Since Eq. 5.15 has  $m_c^*$  on both sides of the equality signs, an iterative procedure must be used to evaluate the correct effective mass. A computer program was written to first obtain an approximate value for  $m_c^*$  from the simplified formulas Eq. 5.2 and Eq. 5.14. The experimental amplitudes were manipulated into the form  $\ln(\alpha_o/T)$  vs.  $T$ . The best straight line was obtained by the method of least squares and the mass calculated from the slope. This was then used as a starting value in Eq. 5.16 which gave a better estimate of  $m_c^*$  from the slope of Eq. 5.15. The iterations were stopped when succeeding effective masses differed by less than 0.2%. In all cases no more than five iterations were required.

An example chosen to emphasize the limitation of Eq. 5.14 is shown in Fig. 10, using data for the  $\delta_3^1$  orbit. The uncorrected points obtained directly from Eq. 5.2 and Eq. 5.14 produce the upper (curved) line. The corrected data points having a linear relation with temperature were evaluated by the procedure just described and had a slope  $\sim 20\%$  smaller.

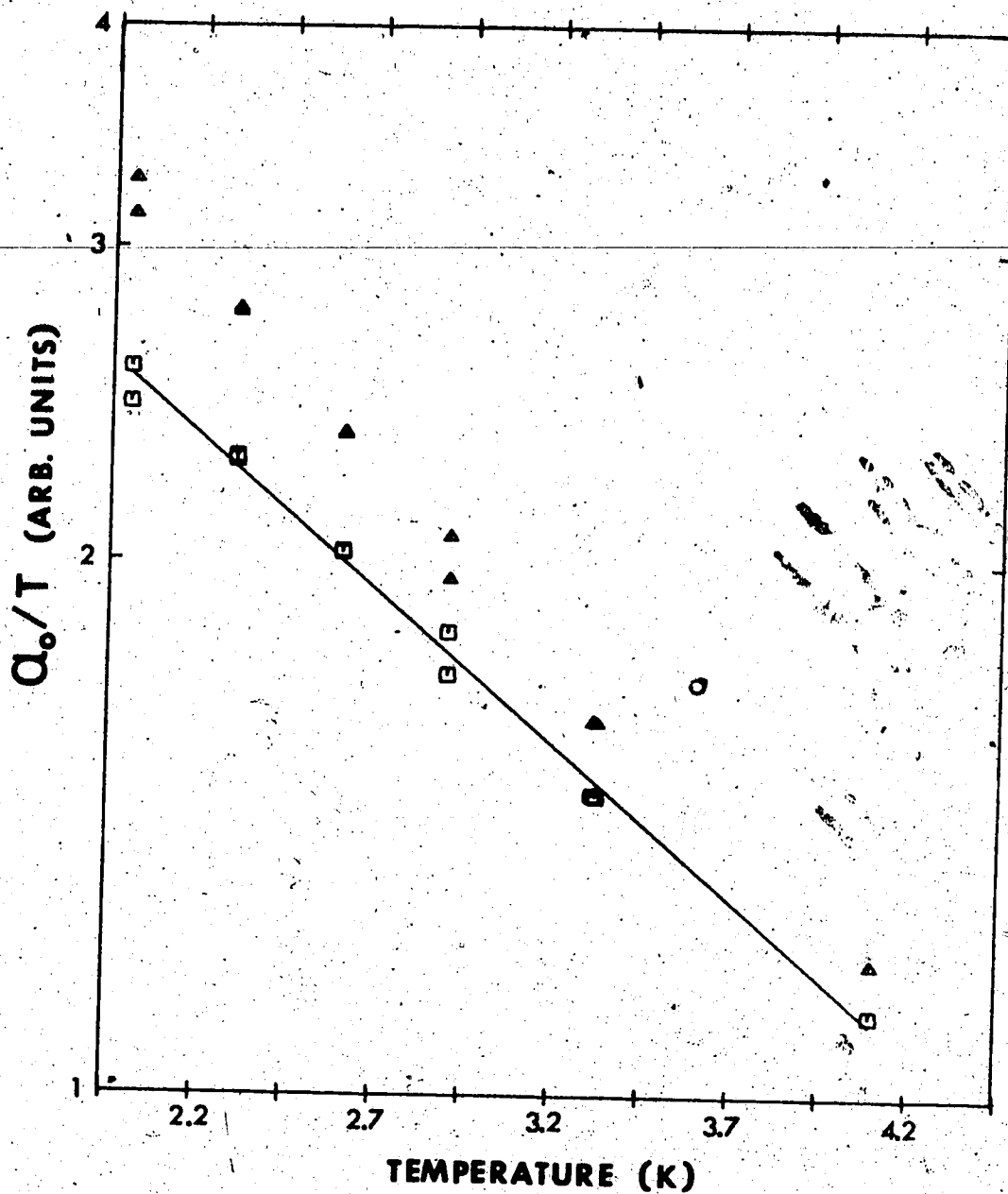


Fig. 10: Plot of oscillation amplitude divided by  $T$  as a function of  $T$  whose slope is related to  $m^*$ . The triangles are uncorrected points and squares the same points after applying the corrections in Eq. 5.16.

## CHAPTER 6

### EXPERIMENTAL RESULTS

Over 50 distinct frequency branches detected in the three principal crystal planes of tin are presented in Sec. 6.1. In order to make discussion of these results easier, a composite graph is displayed without individual data points, followed by graphs showing each plane in detail.

The results of the determination of twenty-eight effective masses are presented in Sec. 6.2. These were obtained for the three principal crystal axes, and also when the field direction was near  $[110]$ .

Some interesting anomalies which were noted in the oscillation amplitudes in tin are detailed in Sec. 6.3. For example, the Sn 2 and Sn 3 crystals gave significantly different amplitudes for certain frequencies in the  $(001)$  plane and along  $[001]$ , where comparison is possible.

#### 6.1 Fermi Surface Frequencies in Tin

The Fermi surface of tin has been extensively studied. To best compare the present work with that already reported, a brief summary of previous relevant investigations is given in Sec. 6.1.1. In Sec. 6.1.3 and Sec. 6.1.4 the experimental results are presented

and compared with this previous work. In Sec. 6.1.2 an elegant scheme is described for identifying the Fermi surface orbits. Originally introduced by Craven and Stark (1968), it has generally been accepted by later investigators and will be used throughout this thesis.

### 6.1.1 Previous Investigations in Tin

The pioneering dHVA work of Gold and Priestley (1960), subsequently referred to as GP, suffered from the lack of an accurate theoretical model. Thus they were unable to correctly assign most of the observed frequencies. Weisz (1966) utilized the radio frequency size effect measurements of Gantmakher (1963, 1964) to deduce a Fermi surface model using pseudopotential theory. Many of the extremal areas predicted by Weisz's model were subsequently found by Stafleu and de Vroomen (1966), referred to as SV, and by Craven and Stark (1968), referred to as CS, using the dHVA effect. The experimental areas, however, did not agree quantitatively with Weisz's model. Thus Craven (1969) calculated a new Fermi surface model to fit their dHVA results. Subsequent radio frequency size effect determinations (Devillers and de Vroomen, 1971), however, showed some disagreement with this model. Using the dHVA effect, further investigations by



053

Vaughan et al (1971) (subsequently referred to as V) and by Finkelstein (1974) (referred to as F1) detected no new Fermi surface areas. Measurements with oscillatory magnetostriction by Finkelstein (1974)

(referred to as F2) also did not observe new frequency branches. Previous to the present results, the only ultrasonic attenuation measurements (of Fermi surface areas) were reported by Deacon and MacKinnon (1973), referred to as DM. Although they observed interesting magnetic breakdown effects, the number of frequency branches detected was much less extensive than reported here.

#### 6.1.2 Nomenclature for Identifying Frequencies in Tin

The naming of Fermi surface areas follows that introduced by CS. The third, fourth, fifth, and sixth Brillouin zones contain sheets of the Fermi surface, and these are identified by the four Greek letters  $\delta$ ,  $\epsilon$ ,  $\pi$  and  $\tau$ , respectively. A subscript attached to the Greek letter specifies in which principal plane a particular extremal area is located. One refers to the (100) plane, two refers to the (001) plane, and three refers to the (110) plane. To distinguish between different areas in the same zone and plane, a superscript attached to the Greek letter indicates

the relative area of the orbit. Where necessary, a Roman letter appended to the superscript identifies a new orbit with an area intermediate to two orbits already named by CS. For example, the Fermi surface area in the third zone and (100) plane with minimum cross-sectional area is designated  $\delta_1^1$ .

The nomenclature employed by CS used Roman letters for the three frequencies attributed to magnetic breakdown. However, in this thesis all magnetic breakdown orbits are identified by the Greek letter  $\beta$ ; the subscripts and superscripts follow the convention already outlined.

All frequencies which cannot be assigned to a particular Fermi surface sheet are denoted by Roman letters. Subscripts will be used where needed to identify the intended principal plane.

### 6.1.3 Composite Graph and Table of Fermi Surface Frequencies in Tin

Frequencies detected in the three principal planes are collected into the composite graph shown in Fig. 11. The frequency branches are named according to the procedure discussed in Sec. 6.1.2, but justification of the assignments will be delayed until Chap. 7. For clarity, individual data points

are not shown since the following section will provide this in detail.

In order to facilitate comparison with previous investigators a line convention has been adopted for Fig. 11. Second harmonics of frequencies are not displayed in Fig. 11 or in the detailed frequency graphs (discussed in the next section) because they provide no additional information regarding Fermi surface areas.

In the rest of the thesis, angles mentioned in the text follow the same convention used in Figs. 11 to 16.

The values of the frequencies along the symmetry axes are presented in Tables 2 and 3, along with the reported values of DM, CS, and SV.

#### 6.1.4 Frequencies in the Three Principal Planes of Tin

The frequency branches observed in each crystallographic plane is presented graphically, with separate figures for each plane. In order to make discussion of the experimental results clearer, each frequency branch on the graphs is assigned an identifying letter in accordance with the naming procedure discussed in Sec. 6.1.2. The solid dots represent individual data points with a  $S/N > 2$ , while open circles show weakly observed data.

---

Fig. 11: Composite graph of all frequency branches observed in tin. Frequencies which have not previously been reported are represented by a solid line. Those frequencies that have appeared in the literature and also were observed in these experiments are shown by a dashed line. A dotted line denotes frequencies that, although reported previously, were not detected in these experiments.



Table 2 :

Fermi surface frequencies  $f$  measured in tin, with  $\mathbf{H}$  along  $[001]$ , are compared with previous investigations.

Orbit	$f$			
	This work	DM <sup>†</sup>	CS <sup>†</sup>	SV <sup>†</sup>
$\delta_{1,3}^1, \delta_{1,3}^1$	0.173	0.174	0.172	0.171
$\delta_{1,3}^2, \delta_{1,3}^2$	0.330	0.334	0.325	0.326
$\tau_{1,3}^0, \tau_{1,3}^0$	0.41			
$\tau_{1,3}^1, \tau_{1,3}^1$	0.449		0.446 <sup>†</sup>	
$\epsilon_{1,3}^2, \epsilon_{1,3}^2$	3.41	3.45	3.41	3.50
$\beta_{1,3}^1, \beta_{1,3}^5$	4.28			
$\pi_{1,3}^5, \pi_{1,3}^1$	5.28	5.49		5.4
$\pi_{1,3}^6, \pi_{1,3}^3$	6.25		6.33	
$\pi_{1,3}^7, \pi_{1,3}^4$	6.83	6.82	6.82	6.85
$E_{1,3}$	7.31			
$F_{1,3}$	7.97			
$H_{1,3}$	8.67	8.33		
$J_{1,3}$	9.92			
$\epsilon_{1,3}^4, \epsilon_{1,3}^3$	10.43		10.35	
$\beta_{1,3}^2, \beta_{1,3}^6$	10.9		10.85	
$\beta_{1,3}^3, \beta_{1,3}^7$	11.14			
$\epsilon_{1,3}^5, \epsilon_{1,3}^4$	11.33	11.0	11.23	11.0
$\beta_{1,3}^4, \beta_{1,3}^8$	13.33	13.7	13.44	
$\beta_{1,3}^5, \beta_{1,3}^{10}$	16.69			
$\beta_{1,3}^6, \beta_{1,3}^{11}$	18.27			
$\beta_{1,3}^7, \beta_{1,3}^{12}$	19.93			

Table 2 (cont'd)

Orbit	f			
	This work	DM <sup>†</sup>	CS <sup>†</sup>	SV <sup>†</sup>
$\beta_1^8, \beta_3^{13}$	22.55			
$\beta_1^9, \beta_3^{14}$	29.27			

<sup>†</sup> for abbreviations of references, see Sec. 6.1.1.

Table 3.

Fermi surface frequencies  $f$  measured in tin, with  $H$  along [100] or [110], are compared with previous investigations.

Axis	Orbit	This work	F		
			DM <sup>†</sup>	CS <sup>†</sup>	SV <sup>†</sup>
[100]	$\tau_1^1, \tau_2^1$	0.440	0.45	0.449	0.44
	$\delta_1^1, \delta_2^1$	1.58		1.58	1.55
	$\pi_1^1, \pi_2^1$	2.07	2.03	2.06/2.09	2.08
	$\epsilon_1^1, \epsilon_2^2$	3.43	3.33	3.30	3.4
[110]	$\tau_2^1, \tau_3^1$	0.583		0.588	0.57
	$\delta_2^1, \delta_3^1$	1.67		1.67	1.65
	$\beta_2^1, \beta_3^1$	1.88			
	$\beta_2^2, \beta_3^2$	2.07			
	$\beta_2^3, \beta_3^3$	2.30			
	$\epsilon_2^1, \epsilon_3^1$	2.49		2.56	2.55
	$\beta_2^4, \beta_3^4$	4.16			4.35
	$C_2, C_3$	5.81			
	$\pi_2^3, \pi_3^2$	6.73		6.78	6.85
	$\pi_2^4, \pi_3^5, \pi_3^6$	8.08	8.05	8.05	
$\epsilon_2^3, \epsilon_3^2$	9.60				

<sup>†</sup> for abbreviations of references, see Sec. 6.1.1.



(100) plane

Detailed plots of the frequencies observed in the (100) plane are presented in Fig. 12 and Fig. 13.

In this plane four cut-offs of branches were observed:  $\pi_1^5$  and  $F_1$  at  $37^\circ$ ,  $\pi_1^7$  at  $46^\circ$ ,  $\pi_1^{5a}$  at  $60^\circ$ ,  $R$  at  $38^\circ$ ,  $\epsilon_1^3$  at  $71^\circ$  and  $\epsilon_1^{5a}$  and  $\epsilon_1^6$  at  $72^\circ$ .

Sn 2 cannot be used for measurements in this plane. Experiments were performed on two separate occasions using Sn 3, an ultrasonic frequency of 410 MHz, and a temperature close to 1.4 K. The low frequency  $\uparrow$  and  $\delta$  orbits shown in Fig. 12 were specifically measured only on the first occasion using fields between 27 and 60 KG. The higher frequencies presented in Fig. 13 were measured on both occasions at fields ranging from 74 to 88 KG.

Along [100], sum frequencies of  $\tau$ ,  $\pi$ , and  $\epsilon$  have been reported by SV, and CS mentions observing unspecified sum and difference frequencies. Further dHVA effect studies by Vaughan (1971) revealed a large number of sum and difference frequencies along [100]. No combinations of frequencies were observed in these experiments, nor are they reported in the ultrasonic attenuation measurements of DM.

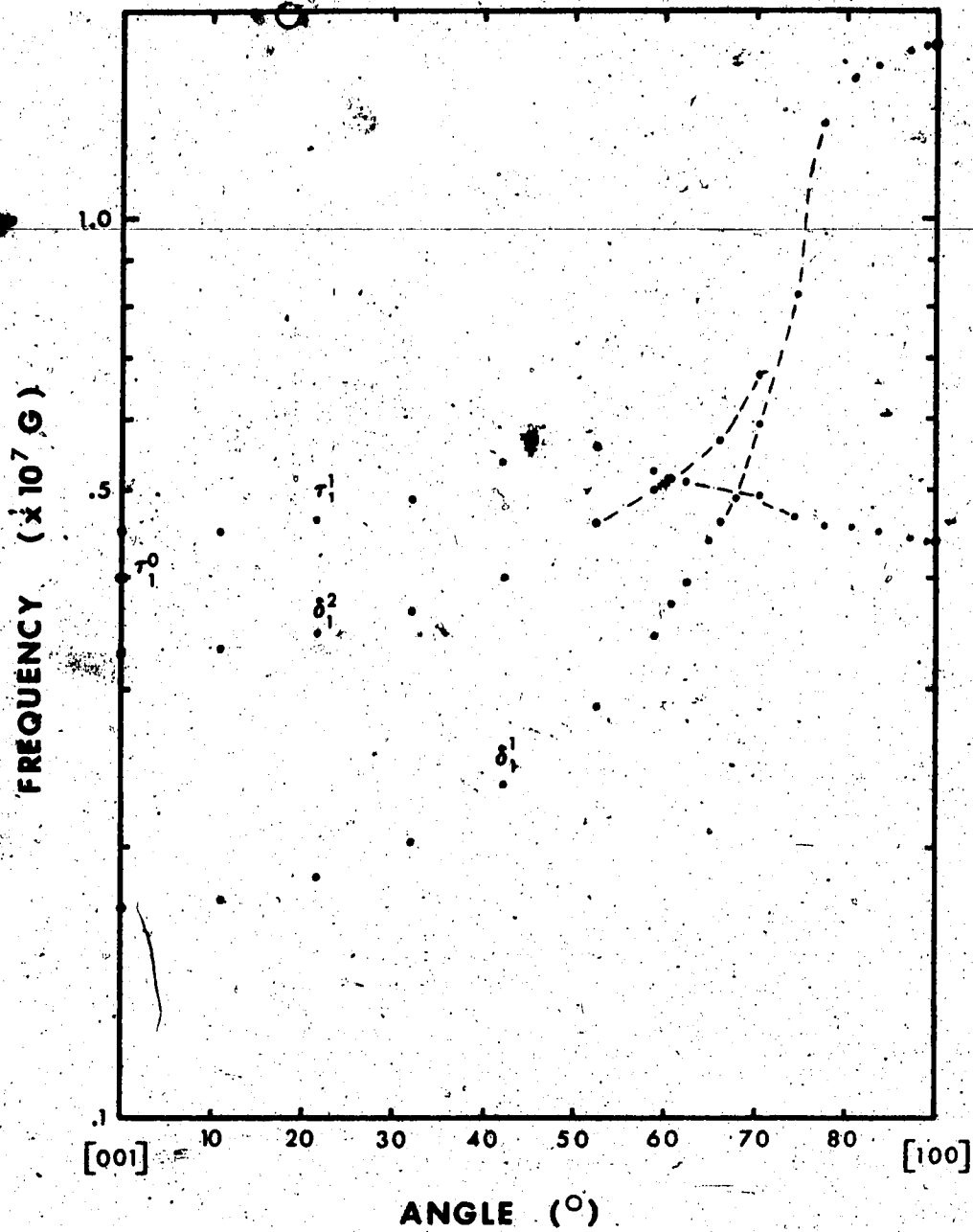


Fig. 12: Orientation dependence of the low frequency branches in the (100) plane of tin.

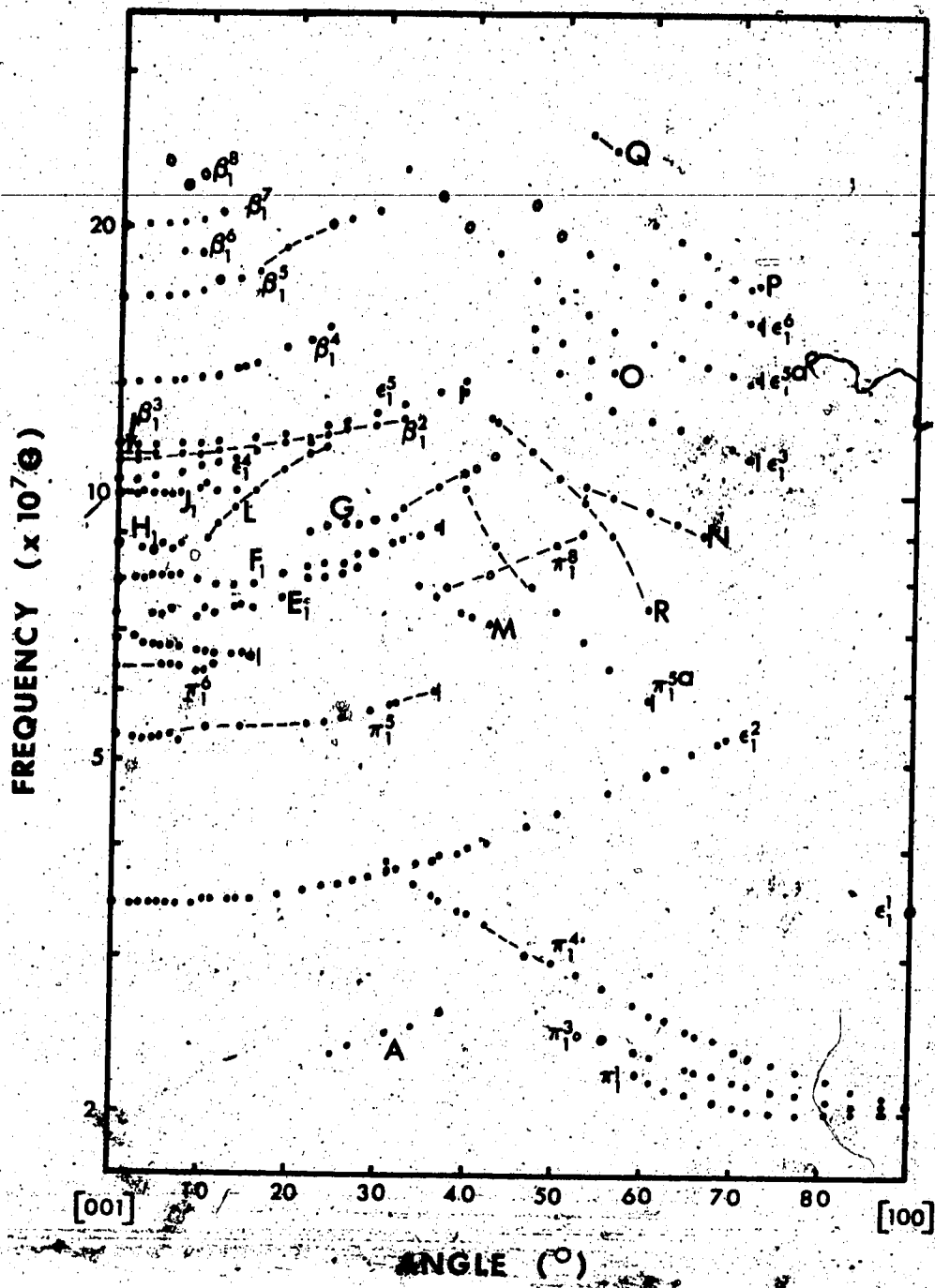


Fig. 13: Orientation dependence of the high frequency branches in the (100) plane of tin.

(110) plane

Fermi surface frequencies detected when the magnetic field was constrained to move in the (110) plane are presented in Fig. 14 and Fig. 15. Three cut-offs of branches were observed in this plane; the frequency  $\pi_3^1$  cut off at 25°,  $\pi_3^3$  at 15°, and  $\epsilon_3^2$  at 70°.

The high frequency orbit,  $\beta_3^9$ , although not detected in Sn 2, was seen at 39° once very strongly in Sn 1. At that time the gear arrangement had not been installed in the sample holder; consequently, the crystal was only approximately aligned in the (110) plane and these data are not included in the results.

Experiments were performed on Sn 1 during the initial testing of the apparatus. Unfortunately the crystal twinned during an unsuccessful attempt to affix transducers by the indium bond technique, discussed in Sec. 3.5. Sample Sn 2 was then grown and used in subsequent experiments. Thus although only one crystal was used for accurate measurements, most frequencies had also been detected using Sn 1.

The data were collected on three occasions using ultrasonic frequencies in the range 390 to 430 MHz. The 390 MHz frequency was needed only when the field direction approached [001]; then the total attenuation became very high. The temperature of

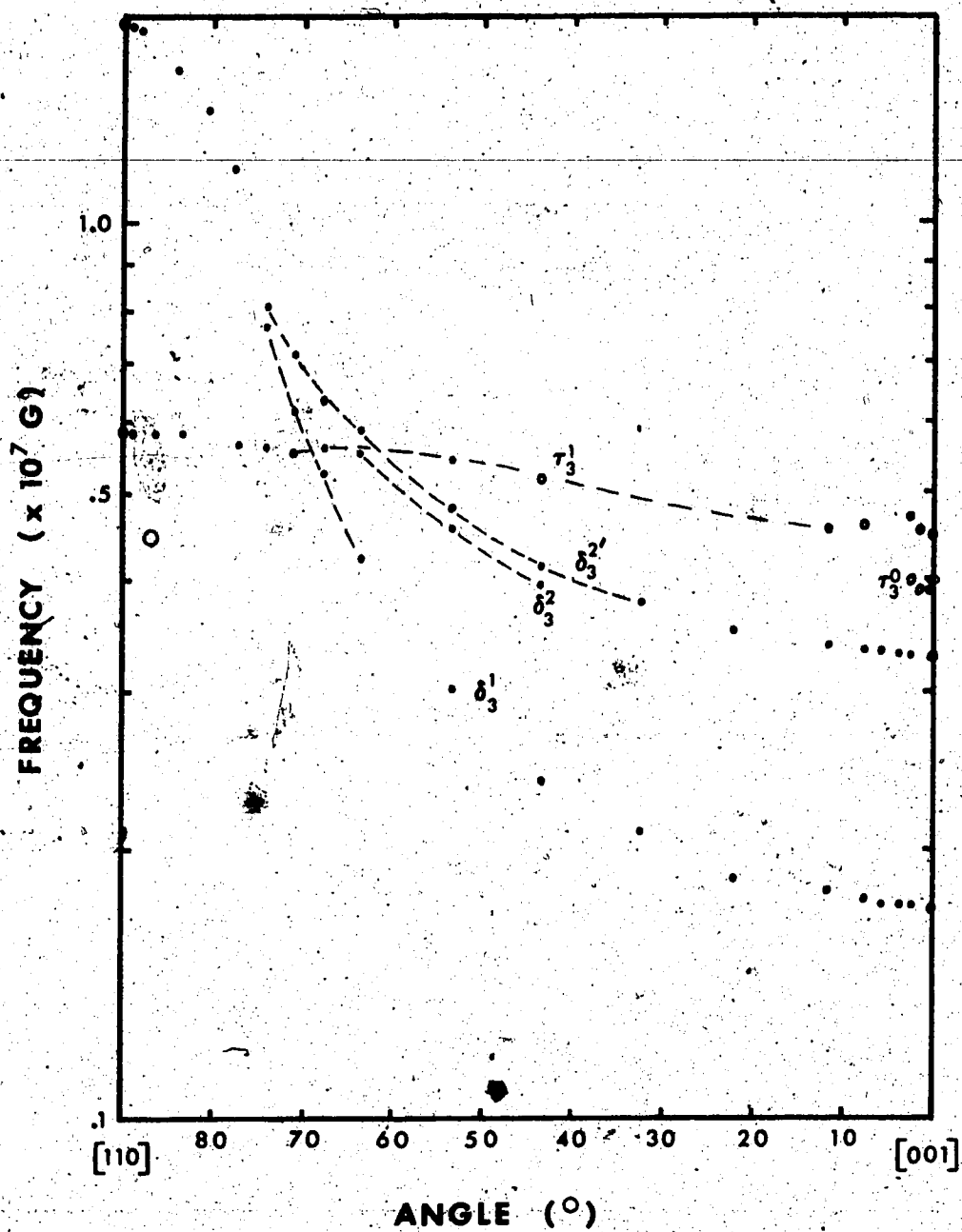


Fig. 14: Orientation dependence of the low frequency branches in the (110) plane of tin.

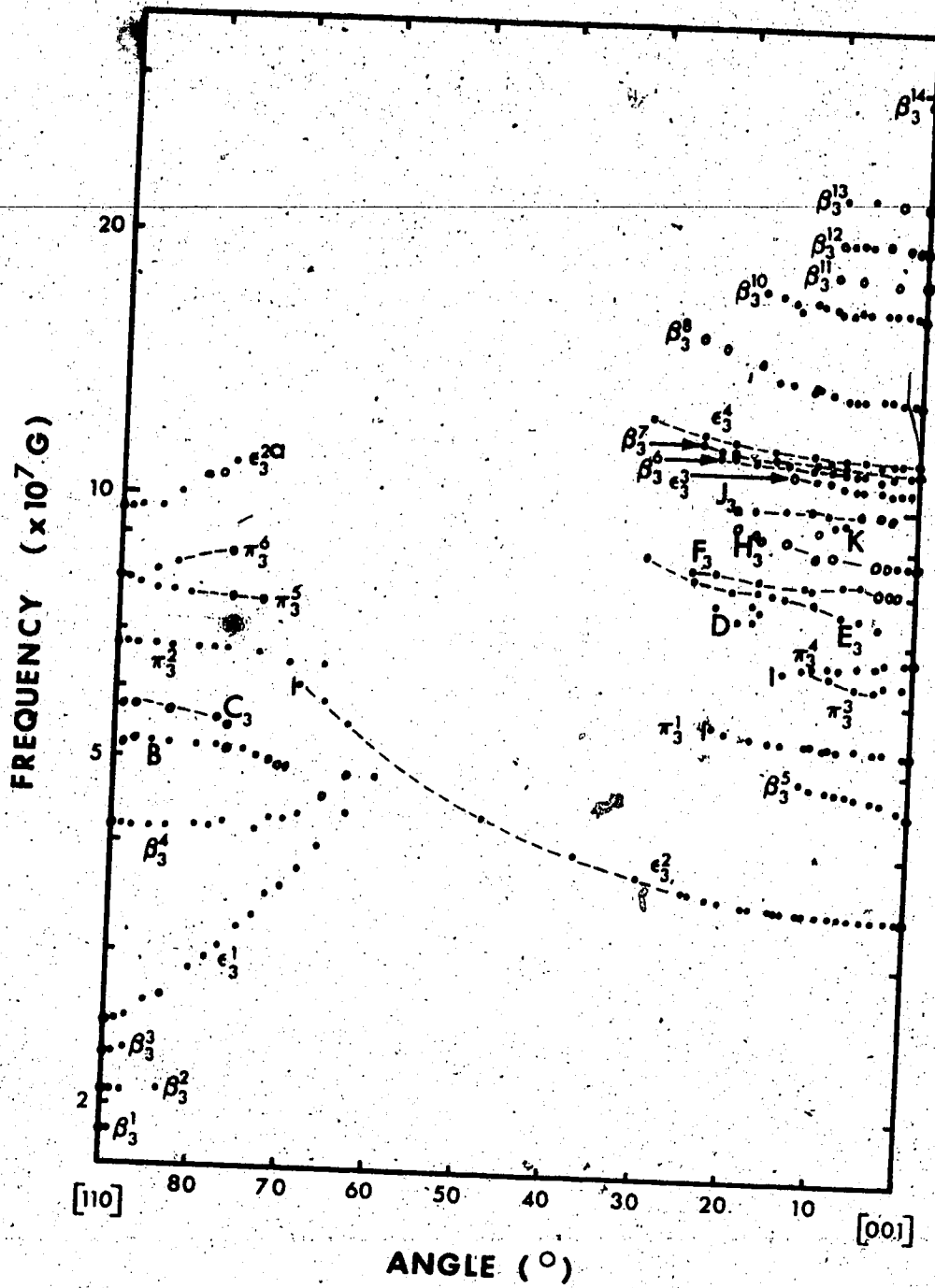


Fig. 15: Orientation dependence of the high frequency branches in the (110) plane of tin.

the sample was held between 1.5 and 2.0 K depending on the experiment. For measurements of the low frequencies shown in Fig. 14, fields between 35 and 75 KG were used. Shorter sweeps in the range 75 to 87 KG were employed for the high frequency observations presented in Fig. 15.

#### (001) plane

Frequency branches observed in the (001) plane are presented in the detailed graph, Fig. 16. Although the frequency labelled  $\pi_2^1$  was extended only  $2^\circ$ , the important information comes from observation of a cut-off at  $10^\circ$ .

This plane could be studied with both Sn 2 and Sn 3. The [110] crystal, Sn 2, was used on two occasions, while the [100] crystal, Sn 3, was used on one occasion. All measured branches, except the one labelled  $\beta_2^3$ , were observed in both crystals at least at one angle.

The experiments were performed at ultrasonic frequencies from 390 to 430 MHz, at temperatures between 1.4 and 2.0 K, and at 66 to 87 KG. The orbit  $\delta_2^1$  could not be detected at greater angles than  $\sim 12^\circ$  due to an overlapping of the larger amplitude third harmonic of  $\tau_2^1$  in Sn 2. The  $\tau$  frequency was being

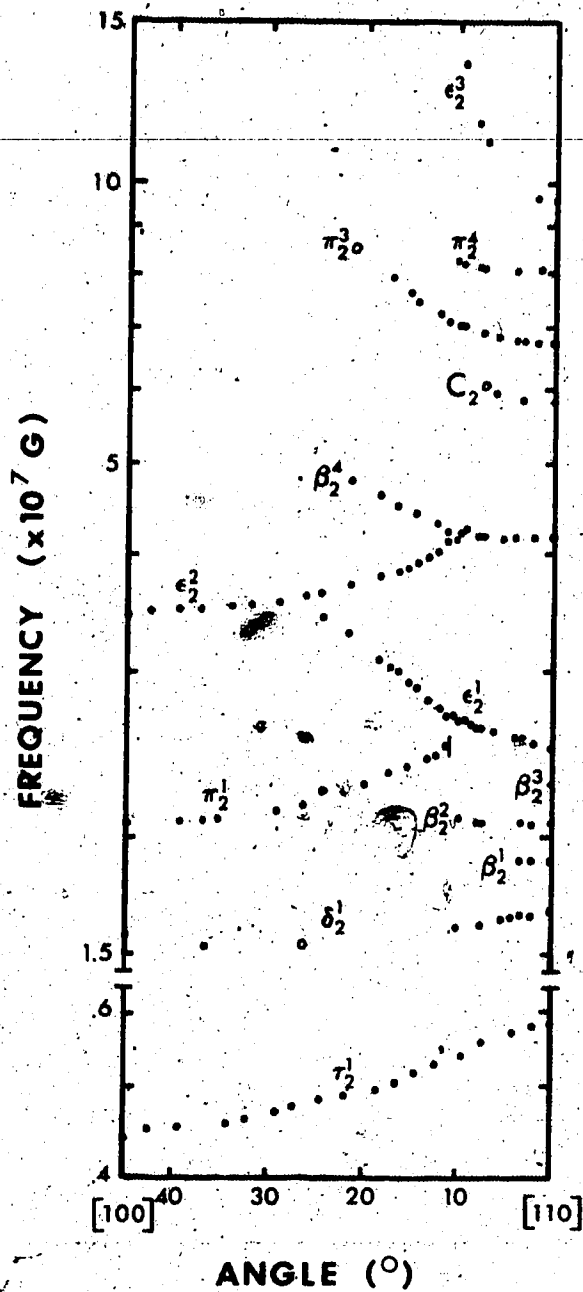


Fig. 16: Orientation dependence of the frequency branches in the (001) plane of tin. Note break in vertical scale above  $\tau_2^1$  branch.



attenuated by the high-pass filter. When the angular dependence of  $\delta_2^1$  was measured with Sn 3, it was seen weakly at 26°, at 37°, and at 45°.

## 6.2 Effective Masses in Tin

Effective mass measurements from 28 orbits are reported. No effective masses have previously been measured by ultrasonic attenuation although some have been obtained by other methods. GP found approximate values for 11 masses using the dHVA effect with impulsive magnetic fields to 80 KG. V also employed the dHVA effect to obtain more accurate values of several masses. Then earlier this year Finkelstein (1974) reported many of the orbital masses utilizing oscillatory magnetostriction (F2) and the dHVA effect (F1).

Azbel-Kaner cyclotron resonance provides an entirely different method for obtaining accurate effective mass values. But for various reasons discussed in Sec. 7.2 they are not immediately comparable.

### 6.2.1 Elimination of Erroneous Data

All effective masses were obtained using the iterative procedure described in Sec. 5.4. Also,

corrected oscillation amplitudes from Eq. 5.16 were plotted against temperature on semi-logarithmic graph paper to check the linearity of the data.

Occasionally an amplitude data point for a particular temperature would have a value much different from that predicted by the other data. Such "bad" data points usually had a low S/N ratio, and thus were confined to the higher temperatures.

One accepted procedure for error analysis is to neglect bad data points in the determination of the slope of the line, but to include it in any error analysis such as the standard deviation. Unfortunately, the small number of data used in evaluating  $m_c^*$  (8 to 15) meant that a "bad" data point greatly increased the standard deviation which then gave unrealistic error limits. In an attempt to overcome the problem, the following procedure was adopted. If a data point was quite far from the predicted straight line found by a least squares fit, the effective mass was recalculated without the point along with the estimator of the standard deviation of the slope. If the neglected point was greater than three standard deviations,  $3\sigma$ , away from the line, it was assumed to be in error and the new  $m_c^*$  was accepted. If, however, the data point was less than  $3\sigma$  from the line, the original effective mass (including this point) was

used. The  $3\sigma$  criterion was adopted since it represents a 99% confidence interval (Cameron, 1960); that is, only 1 data point in 100 is expected to be outside  $3\sigma$ .

The increasing S/N ratio at decreasing temperatures suggests that a weighting function should be used in the least squares determination of the slope. But it was felt that the increased complexity in calculating  $m_c^*$  outweighed the possible slight improvement in accuracy.

Once the effective masses had been obtained and checked for bad data points, each was assigned a 95% confidence interval. This was calculated from the estimator of the standard deviation of the slope using the Student's-t distribution (Cameron, 1960).

6.2.2 Presentation of Effective Masses in Tin

All effective masses calculated in this series of experiments are presented below. The temperature and field ranges used are included, along with the values of  $m_c^*$  obtained by previous investigators using either the dHVA effect or magnetostriction.

At [001]

The twelve effective masses determined with H parallel to [001] are presented in Table 4. The

Table 4

Values of  $m_c^*$  measured in tin for H along [001] compared with previous investigations.

Orbit	$m_c^*$				
	This work	GP <sup>†</sup>	V <sup>†</sup>	F1 <sup>†</sup>	F2 <sup>†</sup>
$\delta_3^1, \delta_1^1$	$0.098 \pm 0.006^a$	0.09			$0.11 \pm 0.01$
$\delta_3^2, \delta_1^2$	$0.162 \pm 0.004^a$	0.15	$0.16 \pm 0.02$		$0.17 \pm 0.01$
$\tau_3^0, \tau_1^0$	$0.15 \pm 0.04^a$				
$\tau_3^1, \tau_1^1$	$0.30 \pm 0.04^a$				$0.30 \pm 0.02$
$\epsilon_3^2, \epsilon_1^2$	$0.48 \pm 0.022^c$	0.51	$0.51 \pm 0.003$		$0.54 \pm 0.03$
"	$0.59 \pm 0.02^b$				
"	$0.5^d$				
$\beta_3^5, \beta_1^1$	$0.87 \pm 0.06^c$				
"	$0.93 \pm 0.04^b$				
$\pi_3^1, \pi_1^5$	$0.60 \pm 0.05^c$	0.64	$0.57 \pm 0.03$		$0.58 \pm 0.02$
"	$0.62 \pm 0.04^b$			$0.59 \pm 0.01$	
$\pi_3^4, \pi_1^7$	$1.0 \pm 0.25^b$			$0.69 \pm 0.02$	$0.71 \pm 0.05$
$H_3, H_1$	$0.58 \pm 0.25^c$				
"	$0.84 \pm 0.33^b$				
$\epsilon_3^3, \epsilon_1^4$	$1.24 \pm 0.09^c$			$0.61 \pm 0.01$	$0.59 \pm 0.06$
"	$1.17 \pm 0.18^b$				
$\beta_3^8, \beta_1^4$	$0.56 \pm 0.1^c$				$0.66 \pm 0.1$
$\beta_3^{10}, \beta_1^5$	$1.1 \pm 0.2^c$				

Table 4 (cont'd)

†: Abbreviations for references found in Sec. 6.1.1.

---

a: H range = 26.9 to 53.9 KG, T range = 4.10 to 2.00 K,  
11 values.

b: H range = 81.6 to 87.1 KG, T range = 2.80 to 1.46 K,  
15 values.

c: H range = 83.4 to 87.9 KG, T range = 2.29 to 1.32 K,  
13 values.

d: Measured by a crystal used in preliminary measurements.

frequencies found along this crystal axis covered two decades, therefore three different sweep ranges were used to obtain the amplitudes. Although considerably attenuated by the high-pass filter, intermediate frequencies were observed in the high frequency traces and thus had their masses determined twice.

At [100]

When the magnetic field was along [100] four orbits were detected and the effective mass of each determined. These are given in Table 5 along with masses reported in previous investigations. It should be noted that at [100] CS reported a second orbit,  $\pi_2$ , with a frequency only 1.3% higher than  $\pi_1$ . Limitations of the apparatus prevented the amplitudes from being sufficiently resolved to determine the individual masses. However, if the orbits had significantly different masses the combined amplitude would deviate from the standard temperature dependence. No such deviation was observed.

In (110) plane

Effective masses were also evaluated when H was parallel to the [110] axis. These are presented in Table 6. In addition, the values of  $m_c^*$  were

Table 5

Values of  $m_c^*$  measured in tin for H along [100] compared with previous investigations. Oscillation amplitudes were measured at 12 temperatures between 3.58 and 1.67 K and a field sweep range of 68.0 to 87.0 KG.

Orbit	$m_c^*$		$v^\dagger$	(dHvA) F1 <sup>†</sup>	(mag.) F2 <sup>†</sup>
	This work	GP <sup>†</sup>			
$\tau_1^1, \tau_2^1$	0.29±0.06	0.26	0.31±0.01		0.28±0.01
$\delta_1^1, \delta_2^1$	0.43±0.07				0.45±0.03
$\pi_1^1, \pi_2^1$	0.79±0.04	0.45	0.55±0.01		0.52±0.01
$\epsilon_1^1, \epsilon_2^1$	0.68±0.09	0.50	0.56±0.01		0.56±0.01

†: Abbreviations of references found in Sec. 6.1.1.

Table 6

Values of  $m_c^*$  measured in tin for H along [110] compared with previous investigations.

Orbit	$m_c^*$		
	This work	GP <sup>†</sup>	F2 <sup>†</sup>
$\tau_3^1, \tau_2^1$	$0.36 \pm 0.03^a$	0.34	$0.41 \pm 0.03$
$\delta_3^1, \delta_2^1$	$0.54 \pm 0.08^a$		$0.46 \pm 0.01$
$\beta_3^1, \beta_2^1$	$0.48 \pm 0.24^a$		
$\beta_3^2, \beta_2^2$	$0.81 \pm 0.14^a$		
"	$0.78 \pm 0.11^b$		
$\beta_3^3, \beta_2^3$	$0.63 \pm 0.31^b$		
$\epsilon_3^1, \epsilon_2^1$	$0.63 \pm 0.08^a$		$0.75 \pm 0.05$
"	$0.61 \pm 0.09^b$		
$\pi_3^2, \pi_2^3$	$0.67 \pm 0.1^b$	0.75	$0.79 \pm 0.02$
$\epsilon_3^{2a}, \epsilon_2^3$	$1.13 \pm 0.34^b$		

†: Abbreviations for references are found in Sec. 6.1.1.

a: H range = 85.2 to 85.0 KG, T range = 3.0 to 1.8 K,  
13 values.

b: H range = 77.7 to 85.1 KG, T range = 3.0 to 1.8 K,  
15 values.



calculated for two other directions of field in the (110) plane. The first was at  $2\frac{1}{2}^\circ$  from [110], and the second at  $7^\circ$  from [110]. These masses are presented in Table 7.

Two sweep ranges were used to adequately include all the Fermi surface frequencies. The orbits  $\beta_3^2$  and  $\epsilon_3^1$  appeared in both traces and consequently had their masses determined twice. The low amplitude oscillations of the  $\beta_3^3$  orbit could not be distinguished in the high frequency trace due to the lower frequency resolution.

### 6.3 Comparison of Oscillation Amplitudes in Tin

#### 6.3.1 Comparison of Amplitudes from Sn 2 and Sn 3

Both the [110] crystal, Sn 2, and the [100] crystal, Sn 3, were used in obtaining frequencies in the (001) plane. In addition, frequencies along [001] can be observed in both crystals. This overlap allowed the measurement of oscillation amplitudes at a particular field direction but with ultrasonic waves travelling down different crystal axes.

The amplitudes were reasonably constant in the (001) plane. Thus only at one angle in the plane were the amplitudes from each crystal compared; this was at [100]. Details of the angular dependence of the

Table 7

Values of  $m_c^*$  measured in tin when H was at an angle  $\theta$  from [110] in the (110) plane.

Orbit	$m_c^*$	
	$\theta = 2\frac{1}{2}^\circ$	$\theta = 7^\circ$
$\tau_3^1$	$0.40 \pm 0.03^a$	$0.4 \pm 0.2^c$
$\delta_3^1$	$0.45 \pm 0.04^a$	$0.58 \pm 0.05^c$
$\epsilon_3^1$	$0.66 \pm 0.05^a$	$0.63 \pm 0.07^c$
	$0.80 \pm 0.14^b$	$0.59 \pm 0.09^d$
$\pi_3^2$	$0.64 \pm 0.09^b$	$1.00 \pm 0.13^d$

a: H range = 65.3 to 84.9 KG, T range = 3.20 to 1.80 K,  
10 values.

b: H range = 77.9 to 85.0 KG, T range = 3.20 to 1.79 K,  
9 values.

c: H range = 65.2 to 85.0 KG, T range = 3.00 to 1.80 K,  
14 values.

d: H range = 77.9 to 85.0 KG, T range = 3.00 to 1.80 K,  
14 values.

amplitudes with angle are given in Sec. 6.3.3.

The ratios of the amplitudes (from each crystal) at  $[100]$  and  $[001]$  were calculated and those equal to or greater than three are included in Table 8. These ratios will only be approximate since the data were gathered during different experiments at slightly different temperatures, field sweep ranges, and noise levels. Also the amplitudes were not corrected for the 4% difference in length of the crystals.

#### 6.3.2 Amplitudes of the Oscillations

Theory predicts a rather strong dependence of oscillation amplitude on angle. The data are presented below so that a comparison can be made.

Most frequency branches exhibit a fairly constant amplitude of oscillation across their entire angular range. However, some orbits show variations greater than a factor of five; these are collected into Table 9. The angle at which the maximum and minimum amplitudes occur are included. Finally the ratio of these two amplitudes is displayed in the last column of the table. Most of the orbits in this table had only a single maximum in amplitude.

Table 8

Ratio R of oscillation amplitudes from Sn 2 ( $\alpha_2$ ) and Sn 3 ( $\alpha_3$ ), for H || [100] or [001]. Only when  $R \geq 3$  are values given.

Axis	Orbit	$\alpha_2^\dagger$	$\alpha_3^\dagger$	R
[100]	$\tau_2^1$	0.61	0.04	15
[100]	$\pi_2^1$	0.0094	0.38	40
[100]	$\epsilon_2^2$	0.052	0.003	17
[001]	$\delta_1^1, \delta_3^1$	0.31	0.035	10
[001]	$\delta_1^2, \delta_3^2$	0.73	0.019	38
[001]	$\tau_1^1, \tau_3^1$	0.051	0.012	4
[001]	$\pi_1^7, \pi_3^4$	0.013	0.072	5
[001]	$\beta_1^4, \beta_3^8$	0.033	0.15	3
[001]	$\beta_1^1, \beta_3^5$	0.16	0.006	>15

†: Amplitudes are in db.

Table 9

Ratio (R) of the maximum oscillation amplitude of an orbit, observed at angle  $\theta_{\max}$ , to its minimum amplitude, observed at angle  $\theta_{\min}$ , in tin. Angles are measured in degrees and follow the convention of Fig. 11.

Orbit	$\theta_{\max}$	$\theta_{\min}$	R
R	50	39	60
$\epsilon_1^2$	0	69	46
$\beta_1^4$	5	24	32
$\beta_1^5$	0	29	20
$\epsilon_1^3$	66	47	3
$\epsilon_1^{5a}$	69	32	38
$\epsilon_1^6$	66	47	15
$\pi_1^{5a}$	50	39	11
$\pi_2^1$ (Sn 3)	26	11	45
$\epsilon_2^2$ (Sn 2)	37	11	7
$\epsilon_3^1$	90	60	
$\epsilon_3^2$	0	69	30
$\beta_3^5$	0	12	7
$\pi_3^1$	0	14	30

#### 6.4 Fermi Surface Frequencies in Indium

The experimental data discussed below resulted from a preliminary investigation of the frequencies in indium. Since only one crystal was used, the study was restricted to the two principal planes, (001) and (100). In none of these experiments was there any evidence of oscillations attributable to the large second zone hole surface.

No generally accepted, systematic procedure had been used to identify the orbits in indium. Therefore, in this thesis the nomenclature employed with tin was modified for use with indium. The third zone has been assigned the Greek letter  $\beta$ , and subscripts and superscripts identify crystallographic planes and Fermi surface areas as discussed previously.

Justification for the assignment of orbits will be made in Sec. 7.5.2.

##### (100) plane

In the (100) plane a frequency branch,  $\beta_1^2$ , was observed which had a S/N  $\sim 30$  (at 2 K) at [100]. As the angle from this axis increased toward [001], the amplitude decreased until it was lost at  $78^\circ$ . The angular dependence of this frequency is shown in Fig.

17.

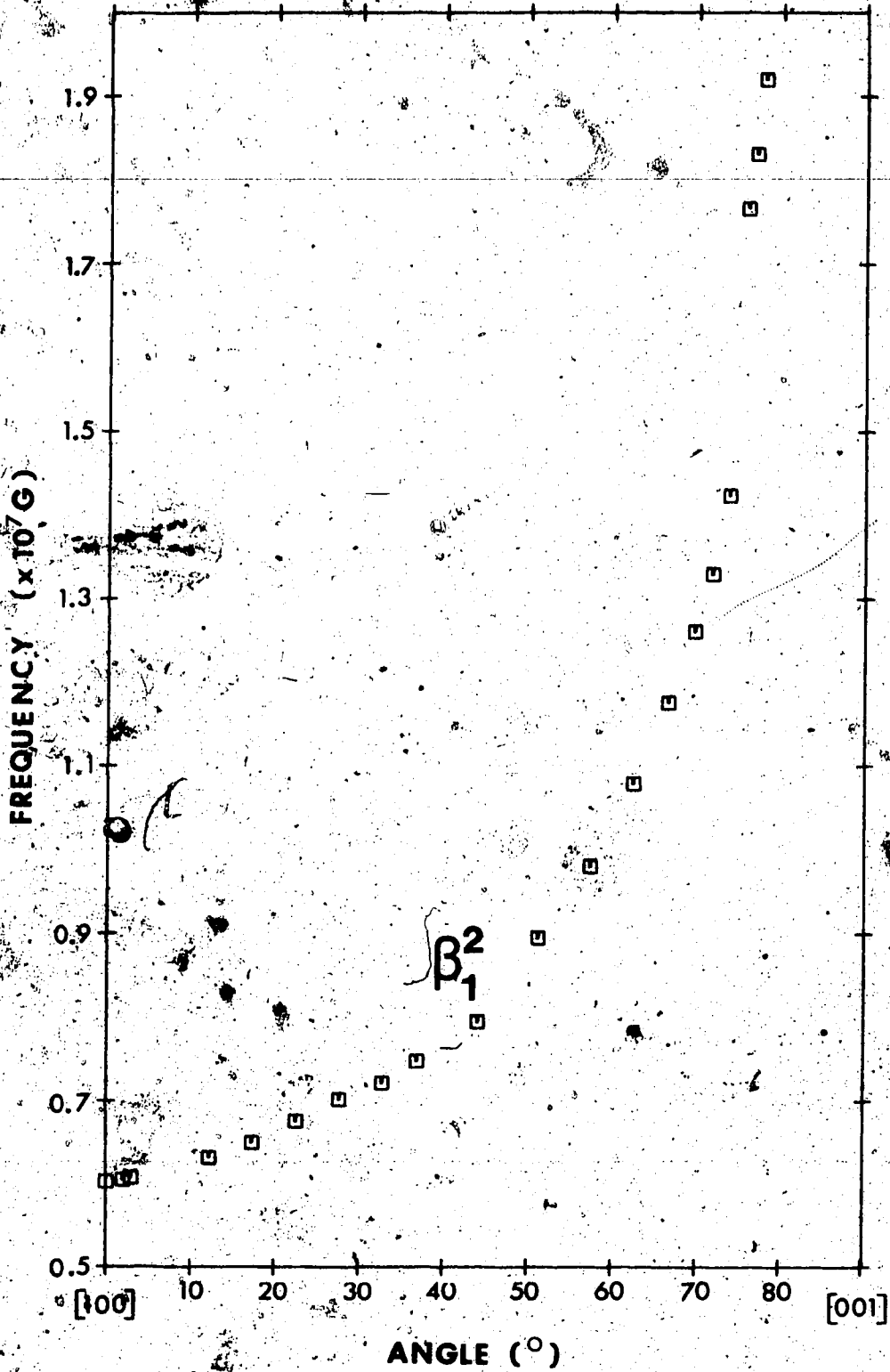


Fig. 17: Orientation dependence of the  $\beta_1^2$  orbit in the (100) plane of indium.

During a preliminary search using small fields a low frequency orbit  $\beta_1^1$  was detected at  $53^\circ$  from [100] in the (100) plane.

### (001) plane

Two frequencies were observed in the (001) plane and assigned to the third zone arms. Their angular dependence in this plane is shown in Fig. 18. The lower frequency orbit,  $\beta_2^3$ , was of large amplitude and required attenuation by the high-pass filter to maintain maximum sensitivity of the apparatus. The higher frequency  $\beta_2^4$  decreased in amplitude as the angle from [100] increased, and was not detected at angles greater than  $40.5^\circ$ . This frequency could not be measured between  $21^\circ$  and  $29^\circ$  because of overlapping with a larger amplitude harmonic of  $\beta_2^3$ .

A low frequency oscillation,  $\beta_1^1$ , was observed in a small field trace at  $16^\circ$  from [100].

The frequencies measured along [100] and at other angles are recorded in Table 10. Corresponding frequencies reported by other investigators are included for comparison. Measurements on the third zone of Indium using the dHVA effect have been done by Brandt and Rayne (1963, 1964), Hughes and Letton (1968), Hughes and Shepherd (1969), and van Weeren and Anderson (1973). Fermi surface areas have also been measured by Balcombe et al (1964) and Cowey et al.



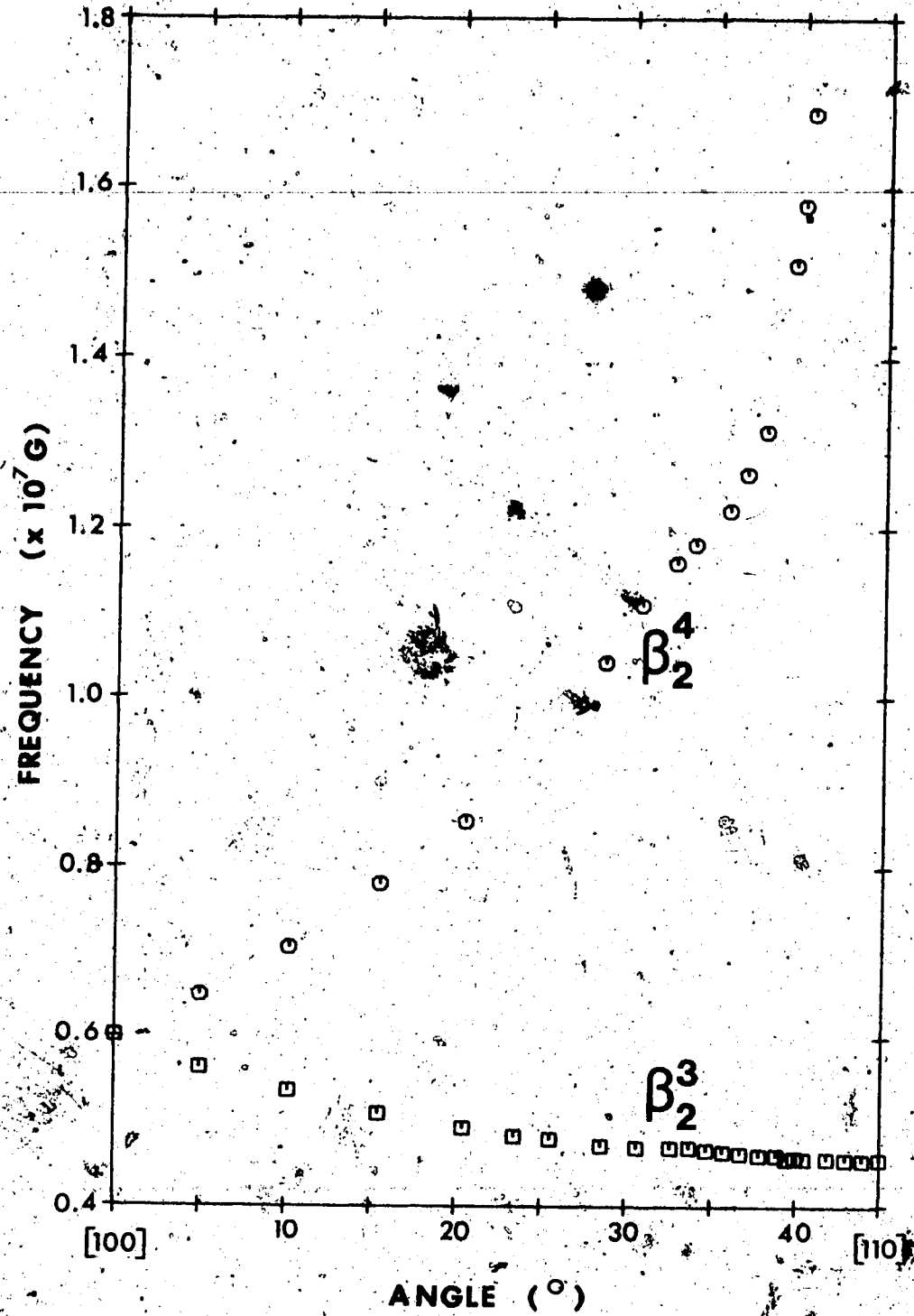


Fig. 18: Orientation dependence of the frequency branches in the (001) plane of indium.

Table 10

Fermi surface frequencies  $f$  in indium, at selected angle  $\theta$  from [100]; are compared with previous investigations. Frequency units are  $10^6$  gauss.

Orbit	$\theta$	f			
		This work	C <sup>a</sup>	BR <sup>b</sup>	HS <sup>c</sup>
$\beta_1^2, \beta_2^3, \beta_2^4$	0°	6.03	6.00	6.16	6.05
$\beta_2^4$	40.5°	16.88			
$\beta_2^3$	45° [110]	4.56 <sup>d</sup>	4.55	4.55	4.60
$\beta_1^2$	78°	19.20			
$\beta_1^1$	53°	0.172	0.18		0.17
$\beta_2^1$	16°	0.106	0.111		0.95

a: Cowey et al (1974), ultrasonic attenuation.

b: Brandt and Rayne (1964), dHvA effect.

c: Hughes and Shepherd (1969), dHvA effect.

d: van Weeren and Anderson (1973) reported  $f = 4.590$  at [110], dHvA effect.

(1974) using ultrasonic attenuation.

Thermal cycling between room temperature and 4 K caused the indium sample to twin, and each thermal cycle increased the amplitude of the frequencies from the new crystallites. The angular dependence of these frequencies suggests that the twinned crystallites are so oriented that their [001] axis is nearly parallel to [100] or [010] of the original crystal (Cowey et al, 1974).

Geometric oscillations were observed between 450 and 4000 gauss at  $T = 1.9$  K when the field was parallel to [010]. The ultrasonic frequencies used were 170, 130, and 90 MHz. The number of oscillations detected, 17 at 170 MHz, allows an approximate mean free path to be calculated, as discussed in Sec. 4.2.2. The extremal caliper dimension measured by these oscillations (Bhatia, 1967) was  $0.88 \times 10^8 \text{ cm}^{-1}$  in the [001] direction.

### 6.5 Apparent Modulation of Two Frequency Branches

Fourier analysis of data collected in the (100) plane during the last run revealed apparent amplitude modulation of two Fermi surface frequencies. The sweep ranges chosen provided sufficient frequency discrimination only on this occasion to resolve the "modulation" side bands. A similar sweep range had been used

88

previously, but not in the (100) plane.

The  $\epsilon_1^2$  frequency branch was affected over an angular range from  $0^\circ$  to  $40^\circ$ , and in Table II are displayed some characteristics of the "modulation". The angle at which the field trace was taken, is given in column 1, and in column 2 the measured frequency of  $\epsilon_1^2$  at that angle is shown. The differences in frequencies between the carrier frequency ( $\epsilon_1^2$ ) and the upper and lower "side bands" are shown in columns 3 and 4, respectively.

The frequency branch  $\beta_1^4$  is unambiguously "modulated" for angles less than  $10^\circ$  only. The details are also presented in Table II.

Several other oscillations were observed with amplitudes as great as these but without "modulation"; therefore this feature is probably not produced by the electronic apparatus. Although the difference frequencies shown in Table II are approximately equal to the frequency of  $\delta_1^2$  or  $2\delta_1^1$  at [001], this is not true in other directions and thus the "modulation" effect is not associated with these orbits.

The absolute value of the Fourier transform showed an 100% modulation of  $\epsilon_1^2$  and an 80% modulation of  $\beta_1^4$ . The transform, after zeroing the amplitudes at other frequencies, when inverted produced a complicated "modulation" or beat pattern which was about

Table II

Apparent "modulation" of oscillation amplitudes in (100) plane in tin. Upper and lower frequency sidebands,  $\Delta f_u$  and  $\Delta f_l$ , expressed as a difference from the "carrier" frequency,  $f_c$ , observed at angles  $\theta$  from [001]. Frequency units are  $10^7$  gauss.

Orbit	$\theta$	$f_c$	$\Delta f_l$	$\Delta f_u$
$\epsilon_1^2$	42°	4.05	0.41	-
"	40°	3.99	0.42	0.40
"	37°	3.90	0.22	0.38
"	34°	3.82	0.37	0.37
"	31°	3.76	0.21	0.30
"	27°	3.67	0.37	0.34
"	25°	3.63	0.36	0.29
"	0°	3.43	0.34	0.35
$\beta_1^4$	10°	13.75	-	0.24
"	6°	13.43	0.32	0.30
"	4°	13.36	0.33	0.33
"	2°	13.34	0.34	0.28
"	0°	13.33	0.33	0.30

10% for  $\beta_1^4$  and less for  $\epsilon_1^2$ . Therefore this is not a simple amplitude modulation as first suggested by the Fourier analysis.

If further experiments confirm the existence of this "modulation", a study of the phase information contained in the transform might help to clarify the nature of this feature.

## CHAPTER

### DISCUSSION OF EXPERIMENTAL RESULTS

The assignment of frequency branches to specific extremal Fermi surface areas of tin is discussed in Sec. 7.1, and the measured effective masses are compared with previous investigations in Sec. 7.2. The results of the comparison of amplitudes are discussed in Sec. 7.3. A short analysis is presented in Sec. 7.4 which estimates the probability of breakdown at two non-equivalent junctions. Finally, the results obtained in indium are discussed in Sec. 7.5.

#### 7.1 Fermi Surface Frequencies of Tin

##### 7.1.1 Model of the Fermi Surface of Tin

The Fermi surface model calculated by Craven (1969) and reproduced in Fig. 19 is used as a basis to assign frequency branches. This figure (except for the sixth zone "molar") originally appeared in the article by CS based on the calculations of Weisz (1966) and apparently was distorted to make visualization of the extremal orbits clearer. In the article by Craven, only the sixth zone molar was redrawn.

Based on Craven's two dimensional scale drawings, the distortions in Fig. 19 are noted. The real Fermi

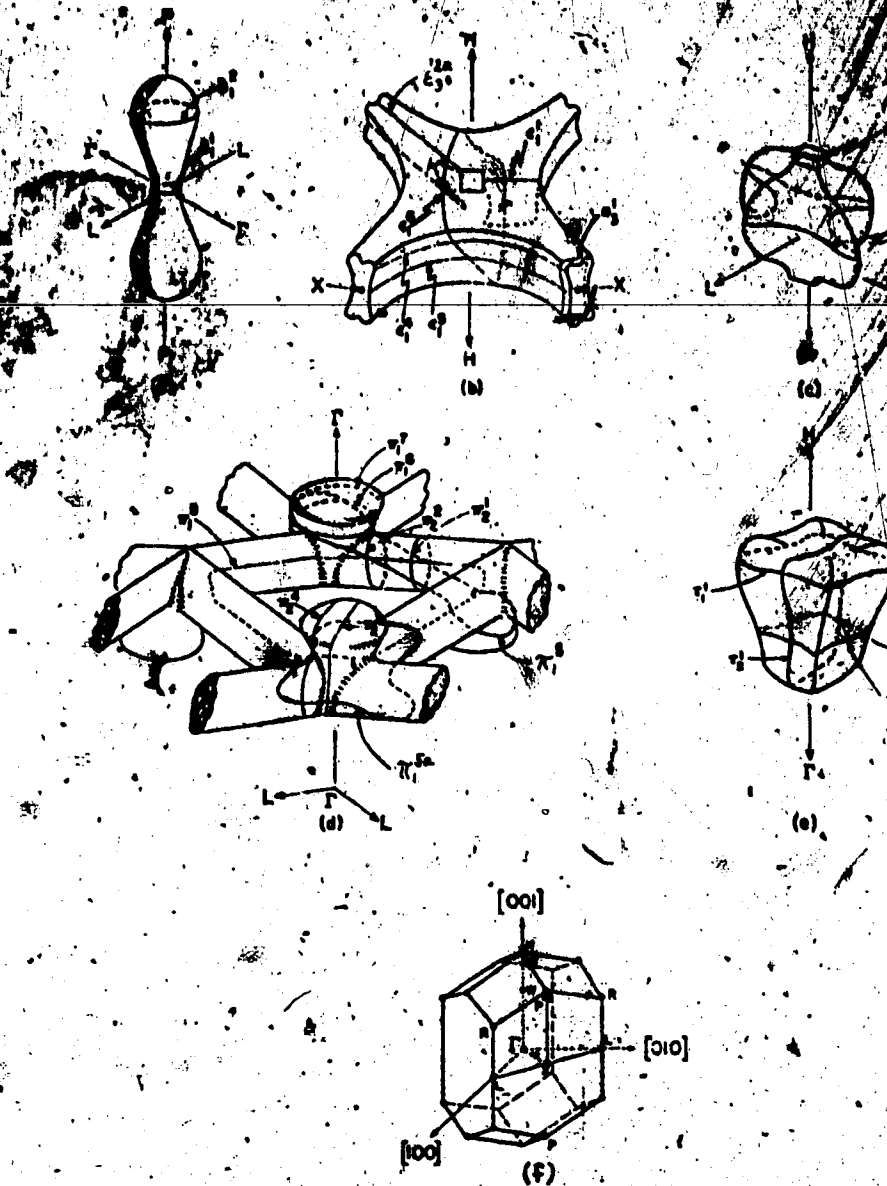


Fig. 19: Model of the Fermi surface of tin according to Craven (1969): (a) third zone holes; (b) fourth zone holes; (c) fourth zone electrons, located in the interior of the fourth zone holes surface; (d) fifth zone electrons; (e) sixth zone electrons. Orbits corresponding to most extremal cross sections are shown; (f) the first Brillouin zone, including some pertinent symmetry points.



surface has a nearly circular neck in the fourth zone, instead of the square neck shown in the figure. The real "pears" in the fifth zone are square when cut by a plane perpendicular to [001] according to Weiss (1966), and this has not been contradicted by Craven; the figure shows a circular cross section. Finally, the "tubes" connecting the pears are much shorter and of a rounded X-shaped cross-section, again according to Weiss and not contradicted by Craven.

In the sixth zone Craven's model of the "molar" has only one extremal cross-section perpendicular to [001]. However, this will be disputed in the next section where a minimum area orbit around the waist of the molar is proposed, as shown in Fig. 19.

#### 7.1.2 Discussion of Frequency Branches in Tin

Justification for the assignment of frequency branches to extremal Fermi surface areas is given below. An orbit also seen by other investigators but named differently will have the authors specifically mentioned in brackets; for example,  $\epsilon_1^3$  (CS). Those branches in Fig. 11 to Fig. 16 labelled with a Roman letter were not assignable to specific Fermi surface orbits. Of these, only the E, F, H, and possibly K

and  $J_3$  branches have previously been reported. The large number of such orbits, A-R, suggests that the Fermi surface in tin is more complex than suggested by Craven's model.

### (100) plane

In this plane, the number of observed frequencies has been doubled and for nine branches the angular dependence was extended. However, the  $\epsilon_1^1$  branch has been detected over a reduced range,

#### Low frequencies

Considering first the frequency branches shown in Fig. 12, the value of the frequencies at [001] and [100], listed in Tables 2 and 3, agree with CS and DM.

The frequency  $\tau_1^0$  was seen very weakly ( $S/N \sim 1$ ) on the two occasions that low frequency data were measured at [001]. Due to the closeness of its cross-sectional area to  $\tau_3^1$  and the lack of other small Fermi surface pockets, this frequency has been assigned to a minimum area at the waist of the (sixth zone) molar. Although Craven's model does not predict a second extremal area, CS reported observing "clear evidence for other branches running near  $\tau_3^1$ ".

$\delta_1^1, \delta_1^2$ 

The relative amplitudes of these two orbits varied quite markedly with the direction of  $q$ . With  $H$  parallel to  $[001]$ ,  $\delta_1^1$  was the largest amplitude in a test crystal whose flat surfaces were perpendicular to  $[001]$ ; i.e.  $q \parallel [001]$ . Sn 2 with  $q \parallel [110]$ , the amplitude ratio  $\delta_1^1/\delta_1^2 = 0.43$  but with Sn 3 where  $q \parallel [100]$  the ratio  $\delta_1^1/\delta_1^2 = 1.84$ . The amplitudes reported by GP show  $\delta_1^1/\delta_1^2 = 0.5$ . These ratios emphasize that the direction of  $q$  relative to the lattice greatly affects the sensitivity of the ultrasonic "probe" to certain orbits.

 $\tau_1^1$ 

The frequency branch  $\tau_1^1$  had a  $S/N \sim 3$  in the  $(100)$  plane. But it was observed by GP, using the dHVA effect, with a  $S/N \sim 13$  at  $[001]$  and a substantially smaller  $S/N$  for directions of  $H$  off-axis.

#### High frequencies

In order to facilitate comparison with other work, Table 12 includes all branches which were detected over a different angular range than reported by CS, DM and SV.

Table 12

Comparison, with previous investigations, of the angular range  $\Delta\theta$  of frequency branches in the (100) plane of tin. Angles are measured in degrees from [001]. Only those branches with difference  $>3^\circ$  are presented.

Orbit	This work	$\Delta\theta$		
		DM <sup>†a</sup>	CS <sup>†a</sup>	sv <sup>†a</sup>
$\pi_1^3$	52.5-90	55-90	81-90	
$\pi_1^4$	31-90	55-90	52-90	43-90
$\epsilon_1^1$	at 90	81-90	70.5-90	72-90
$\epsilon_1^2$	0-69	0-70	0-71	0-70
$E_1$	0-27	at 10, at 15		15-27
$F_1$	0-36	15-25		27-30
$H_1$	0-7	0-10 <sup>b</sup>		
$\pi_1^8$	37-52		35-59	
R	29-60		52-72	
$\beta_1^1$	0-32		0-25	
$\epsilon_1^5$	0-39		0-36	
$\beta_1^4$	0-24	0-10	0-5	

†: Abbreviations for references are found in Sec. 6.1.1.

a: Angles are extracted from the appropriate graphs.

b: Three data points, one weakly observed.

$\pi_1^1, \pi_1^4$ 

The branches  $\pi_1^1$  and  $\pi_1^4$  were not resolved at [100]. Using Fourier analysis the resolution of two frequencies requires at least one beat, and this could not be recorded within the 15" limit of the X-Y plotter while still providing enough sampling points to measure the  $\pi_1^1$  frequency. The measured value of  $\pi_1^1$  (and  $\pi_1^4$ ),  $2.072 \times 10^7$  gauss, falls between the values measured by CS for  $\pi_1^1$  and  $\pi_1^4$ . The branch  $\pi_1^1$  was observed by CS to cut off at  $\sim 59^\circ$ . The low S/N prevented observation of an unambiguous cut-off in these experiments but  $\pi_1^1$  was seen at  $59^\circ$ , an observation which is not in essential disagreement.

 $\epsilon_1^1$ 

The  $\epsilon_1^1$  orbit was observed at [100] with a  $S/N \sim 2$  and not detected at other angles. Also, the frequency was  $\sim 3\%$  greater than reported by CS and DM. In the dHVA effect, GP observed  $\epsilon_1^1$  with a  $S/N > 10$ , and V reported that it produced the largest amplitude oscillations of all frequencies detected at [100]. The dHVA effect appears to be more sensitive to this orbit than ultrasonic attenuation.

 $E_1, F_1$ 

The unassigned frequency branches  $E_1$  and  $F_1$  have

been observed over a far greater range than previously. Although not seen at all by CS, DM detected five frequency data points (his  $F_1$ ; three points were weakly observed) in the region of  $F_1$  and two weakly observed data points (not named) in the region of  $E_1$ . The less precise measurements of SV (his  $F_2$ ) show that  $E_1$  was weakly observed between  $15^\circ$  and  $30^\circ$ . In the present experiments,  $E_1$  and  $F_1$  were measured from  $[001]$  to  $28^\circ$  where they merged into a single branch which cut off at  $37^\circ$ . No unambiguous assignment of  $E_1$  and  $F_1$  could be made, even though the cut-off is identical with that of  $\pi_1^5$  which suggests that they correspond to non-central orbits in the fifth zone.

$\pi_1^{5a}$

The frequency branch  $\pi_1^{5a}$  cuts off at  $60^\circ$ . It is tentatively assigned to an orbit enclosing a "pear" and a "tube" in the fifth zone, as sketched in Fig. 19.

$\pi_1^6, \pi_1^7$

The short branches  $\pi_1^6$  and  $\pi_1^7$  were observed to merge and cut off at  $\sim 16^\circ$ . CS reported a cut-off but did not mention the angle; from their Fig. 3 it can be inferred to be  $\sim 16^\circ$ .

The small difference in frequency between the  $\pi_1^7$  (pear) and  $\pi_1^5$  (tube) orbits confirms that the "tubes" connecting the "pears" are much shorter than shown by the Fermi surface model of Fig. 19.

$\epsilon_1^3, \epsilon_1^{5a}, \epsilon_1^6$

CS observed two frequency branches, which they labelled  $\epsilon_1^3$  and  $\epsilon_1^6$  but are referred to here as  $\epsilon_1^3$  (CS) and  $\epsilon_1^6$  (CS), that I believe were incorrectly assigned to the orbits  $\epsilon_1^3$  and  $\epsilon_1^6$ . The orbit  $\epsilon_1^6$  traverses the hole surface and is cut off by the neck for angles greater than  $71^\circ$ . The orbit  $\epsilon_1^3$  is a non-central one which goes through the re-entrant neck and around the electron "crossed-lens" surface, re-emerges from the same neck then continues around on the hole surface but misses the neck on the opposite side. A sketch of these orbits is shown in Fig. 20.

Craven (1969) claimed to have verified the assignments of CS on the basis of his band structure calculation. However, Devillers and de Vroomen (1971) cast doubt on the assignments since they report appreciable deviations of Craven's model from their radio frequency size effect measurements. In addition, as shown in Fig. 13 two new frequencies were found which cut off within  $1^\circ$  of  $\epsilon_1^6$  (CS). The centre frequency,  $\epsilon_1^{5a}$ , corresponds to  $\epsilon_1^6$  (CS) and another branch,

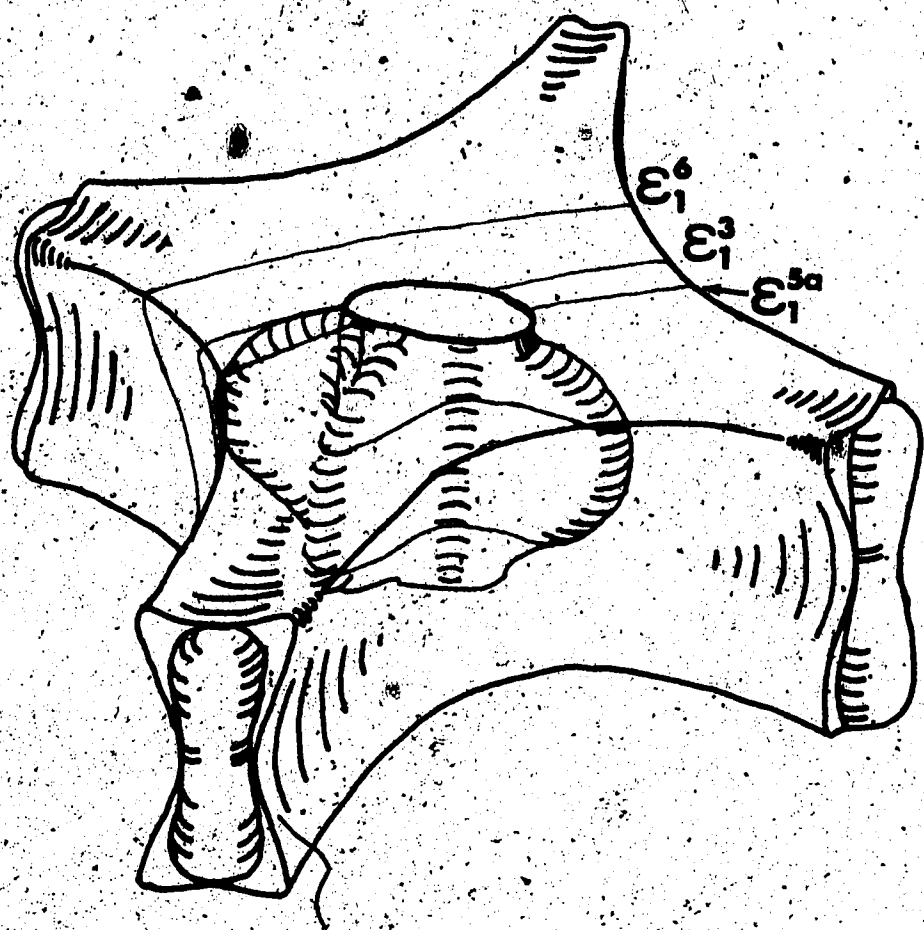


Fig. 20: Orbits  $\epsilon_1^3$ ,  $\epsilon_1^{5a}$ , and  $\epsilon_1^6$  in the fourth zone.



$R_1$  corresponds to  $\epsilon_1^3$  (CS). The discovery of these new frequencies increases the possibility that

$\epsilon_1^3$  (CS) and  $\epsilon_1^6$  (CS) have been incorrectly assigned.

Finally, a simple comparison of areas also suggests that the previous assignments are in error. At cut-off ( $71^\circ$ ) the area of the orbit  $\epsilon_1^3$  must be greater than the areas of  $\epsilon_1^6 - \epsilon_1^2$  which approximates it. The composite  $\epsilon_1^6 - \epsilon_1^2$  serves as a lower bound since  $\epsilon_1^6$  is a minimum area orbit while  $\epsilon_1^2$  is a maximum area orbit, and both must be displaced slightly to form  $\epsilon_1^3$ . Using values of frequency extracted from Fig. 3 of CS at  $71^\circ$ ,  $\epsilon_1^6(\text{CS}) - \epsilon_1^2 = 8.1 \times 10^7$  gauss but  $\epsilon_1^3(\text{CS})$  has a lower value equal to  $6.1 \times 10^7$  gauss.

As a result of the difficulties with the interpretation of  $\epsilon_1^3$  (CS) and  $\epsilon_1^6$  (CS), these two frequencies have been reassigned in this thesis. As shown in Fig. 20, there are two possible orbits which include both the hole and electron surfaces but only one neck. The areas enclosed by  $\epsilon_1^3$  and  $\epsilon_1^{5a}$  will be less than the area of  $\epsilon_1^6$ ; consequently, the highest frequency of the three has been ascribed to  $\epsilon_1^6$ , the middle frequency to  $\epsilon_1^{5a}$  which traverses a smaller part of the electron surface, and the lowest frequency to  $\epsilon_1^3$ . Using values from Fig. 13 at  $69^\circ$  where data for  $\epsilon_1^2$  is available,  $\epsilon_1^3 = 11.37 \times 10^7$  gauss which is 5% larger than  $\epsilon_1^6 - \epsilon_1^2 = 10.81 \times 10^7$  gauss.

R

The frequency  $R_1^3$  (in CS), which was not assignable, abruptly cut off at  $38^\circ$ . The final data point at  $50^\circ$  had a frequency below the anticipated extrapolation of the other points. In the composite graph Fig. 11 this point is denoted by a small square. An outright error in the angle or frequency is unlikely since other frequencies in the same Fourier transform were not similarly displaced. The amplitude was also comparable to the amplitudes of other data in R ( $S/N > 10$ ). Except for this one point, the branch R agrees with  $\epsilon_1^3$  (CS) in the region of overlap.

#### Magnetic breakdown orbits $\beta$

As discussed in Sec. 6.1#2, all frequencies labelled with  $\beta$  are assigned to magnetic breakdown orbits. Near [001], the small waist of the third zone dumb-bell orbit ( $\delta_1^1$ ) acts as a switching or linking orbit to  $\epsilon_1^5$  in the fourth zone. At the magnetic fields employed in these experiments ( $H \sim 80$  KG), many breakdown orbits can exist because the tunneling probability is about 0.9 (Barklie and Pippard, 1970 and Eq. 2.11).

The frequencies ascribed to breakdown are given in Table 13 which shows the experimental frequencies, the algebraic sums of  $\delta_1^1$  and  $\epsilon_1^5$  comprising the break-

Table 13

Comparison in tin of experimental frequencies,  $f_{exp}$ , with the frequencies,  $f_p$ , of proposed magnetic breakdown orbits (T) at angle  $\theta$  from [001] in the (100) plane.

These orbits are calculated from the measured values of  $\epsilon_1^5$  and  $\delta_1^1$  and the frequency units are  $10^7$  gauss.

Orbit	$\theta$	$f_{exp}$	$f_p$	T
$\beta_1^1$	0°		4.66	$2\beta_1^4 - 2\epsilon_1^5$
$\beta_1^2$	0°	10.83	10.97	$\epsilon_1^5 - 2\delta_1^1$
"	32°	12.23	12.22	"
$\beta_1^3$	0°	11.15	11.12	$\epsilon_1^5 - \delta_1^1$
$\beta_1^4$	0°	13.33	13.63	$A_{BZ} + 2\delta_1^1 - \epsilon_1^5$
"	23.5°	15.50	15.29	"
$\beta_1^5$	0°	16.69	16.28	$2\beta_1^4 + 2\delta_1^1 - \epsilon_1^5$
"	29°	20.9	20.42	"
$\beta_1^6$	7°	18.75	18.50	$3\beta_1^4 - 2\epsilon_1^5$
$\beta_1^7$	0°	19.9	20.33	$3\epsilon_1^5 - \beta_1^4$
"	9°	20.25	20.35	"
$\beta_1^8$	9°	22.9	22.72	$2\epsilon_1^5 - \delta_1^1$

†: Area of Brillouin zone,  $A_{BZ} = 24.6 \times 10^7$  gauss at  $\theta = 0^\circ$ .

down orbits, and the corresponding frequencies. The shapes of these orbits are displayed schematically in Fig. 21. Of the seven breakdown orbits measured in this plane, only  $\beta_1^2$  and  $\beta_1^4$  have been observed previously.

The experimentally measured frequencies are not expected to precisely equal the frequencies calculated in the manner described since the electron on tunneling encloses a slightly different area than the algebraic sum of the component areas (Stark and Falicov, 1967; pg 261).

$H_1$

The frequency of branch  $H_1$  does not change with angle, as shown in Fig. 13, and the corresponding branch in the (110) plane,  $H_3$ , increases only slightly (Fig. 15). In contrast DM observed a frequency,  $G(\text{DM})$ , that was 5% lower than  $H_1$  at [001] but which increased rapidly in both planes.  $G(\text{DM})$  was incorrectly ascribed to the magnetic breakdown orbit  $2\beta_1^5 - \beta_1^4$ , since this orbit decreases with angle away from [001], although by only 1% in  $10^\circ$ .

Although  $H_1$  could possibly be ascribed to this breakdown orbit, it is unlikely for three reasons:

- (1)  $H_3$  in the (110) plane increases slightly with angle.
- (2) The measured value of  $H_1$  at [001] was  $8.77 \times 10^7$  gauss

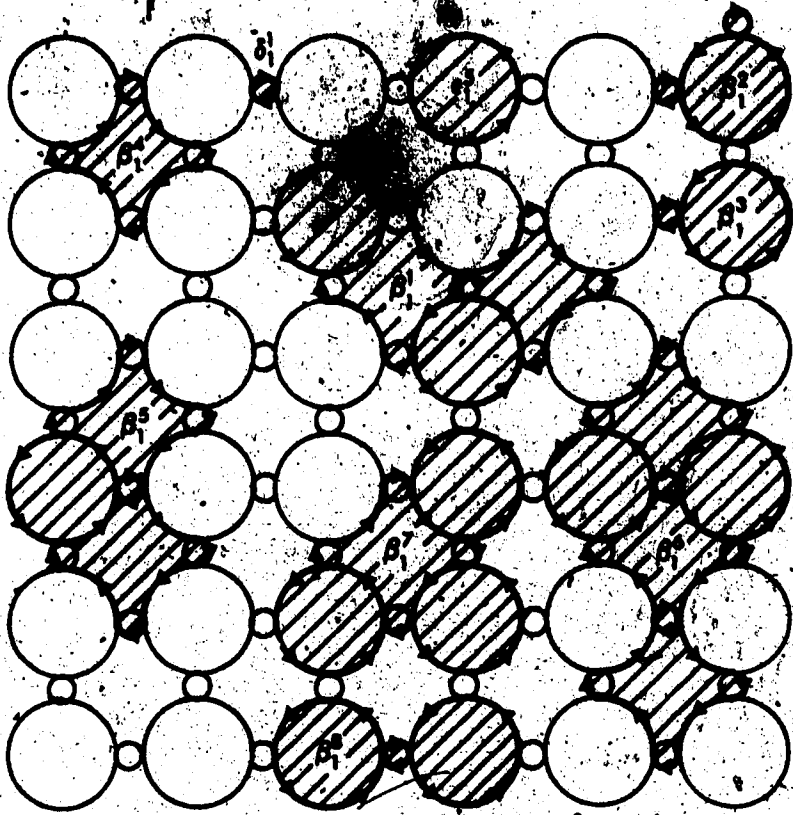


Fig. 21: Cross section in TXL plane of parts of the third and fourth zones, shown periodically extended, to illustrate magnetic breakdown orbits composed from  $\epsilon_1^5$  and  $\delta_1^1$ .

compared to  $2\epsilon_1^5 - \delta_1^4 = 9.01 \times 10^7$  gauss using the experimental values of  $\epsilon_1^5$  and  $\delta_1^4$ . The difference, 2.7%, is somewhat larger than the differences found in Table 13. (3) There exists the possibility that  $H_1$  and L are parts of a single branch, although the sharp curvature then required at  $9^\circ$  is unusual. If  $H_1$  is part of a single branch, then it is definitely not caused by magnetic breakdown.

#### (110) plane

In this plane, the number of known frequency branches has been doubled and the angular dependence of seven have been extended.

#### Low frequencies

Frequencies produced by small area orbits in the third and sixth zones were shown in Fig. 14. CS reported observing four  $\delta_3$  frequency branches in the centre of the plane which indicate the dumb-bells are not of circular cross-section. In the present experiments, the frequencies  $\delta_3^1$  and  $\delta_3^{1'}$  were not resolved, but  $\delta_3^2$  and  $\delta_3^{2'}$  were resolved at three angles. The frequency  $\tau_3^0$  was weakly detected near [001] on three separate occasions; it is assigned to the waist of the sixth zone molar.

### High frequencies

The high frequencies observed in the (110) plane were shown in Fig. 15, and in Table 14 the angular range of branches observed in these experiments and previously are compared.

$\epsilon_3^1$

The  $\epsilon_3^1$  orbit was only observed up to  $30^\circ$  from [110], and DM reported seeing it weakly between  $10^\circ$  and  $20^\circ$  from [110]. However, the dHVA work of CS and SV detected this orbit up to  $44^\circ$  from [110], suggesting that ultrasonic attenuation is a less sensitive probe for this particular orbit.

$\epsilon_3^2$

A cut-off of  $\epsilon_3^2$  was found at  $70^\circ$ , in agreement with DM and the band structure calculations of Craven (1969). The observation of this orbit to within  $20^\circ$  of [110], and similarly for  $\epsilon_1^2$  ( $21^\circ$ ), confirms that the neck has a more circular shape than shown in Fig.

19.

$\pi_3^1$

The  $\pi_3^1$  orbit was observed in these experiments to be cut off at  $25^\circ$ ; CS reports observing a cut-off at  $\sim 23^\circ$ . At  $23^\circ$  the frequency of  $\pi_3^1$  was  $5.64 \times 10^7$  gauss,

Table 14

Comparison with previous investigations of the angular range  $\Delta\theta$  of frequency branches in the (110) plane of tin. Angles are measured in degrees from [001]. Only those branches with differences  $\geq 3^\circ$  are included.

Orbit	$\Delta\theta$			
	This work	DM <sup>†a</sup>	CS <sup>†a</sup>	SV <sup>†a</sup>
$\delta_3^2$	43-64		0-70	
$\epsilon_3^1$	60-90	70-80	46-90	46-90
$\beta_3^4$	64-90	70-90		72-90
$\pi_3^1$	0-25	0-32	0-23	0-15
$\pi_3^5$	74-90		80-90	
$\pi_3^6$	78-90	75-95	72-90	
$\epsilon_3^2$	0-69	0-70	0-58	0-52
$E_3$	4-27	at 25		
$F_3$	2-61	at 10, at 30		
$\epsilon_3^3$	0-16		0-19	0-8
$\epsilon_3^4$	0-30	0-31	0-38	0-37 *
$\beta_3^8$	0-25	0-11	0-3	
$\beta_3^{13}$	0-10	11-16		

†: Abbreviations for references are found in Sec. 6.1.1.

a: Angles are extracted from the appropriate graphs.



which agrees with CS's (Fig. 3) value of  $5.7 \times 10^7$  gauss, but not with DM (Fig. 2) who obtained  $6.2 \times 10^7$  gauss.

Also, the orbit seen by DM appears to have a much larger angular dependence and was observed past  $25^\circ$ .

$\pi_3^3, \pi_3^4$

The two branches  $\pi_3^3$  and  $\pi_3^4$  were observed to cut off at  $16^\circ$  which is the same as reported by CS.

D

The collection of data points labelled D had a S/N  $\sim 2$  to 3 and could not be dismissed as noise. The point at  $72^\circ$  was observed during one experiment, while the others were detected during the other experiment covering these angles some weeks later.

$E_3, F_3$

The unassigned branch  $F_3$  was weakly observed at  $10^\circ$  and  $30^\circ$ , and the branch  $E_1$  at  $25^\circ$ , by DM (Fig. 3); these frequencies were not observed by CS or SV. The two branches appear to merge at  $\sim 28^\circ$ , although the lack of data at this particular angle makes the evidence less convincing.

$H_3$

The observation by DM (his  $G_3$ ) of a frequency branch which rapidly increased away from [001] conflicts

with the data measured in these experiments and shown in Fig. 15. Possibly his data at  $10^\circ$  and  $12^\circ$  are in reality part of the frequency branches  $K$  and  $J_3$ , respectively. Their assignment of  $G_3$  (DM) to the magnetic breakdown orbit  $2\epsilon_3^4 - \beta_3^8$  is clearly incorrect, as has already been discussed for the corresponding orbit in the (100) plane.

It is improbable that the weakly observed branch  $H_3$  is produced by the magnetic breakdown orbit  $2\epsilon_3^4 - \beta_3^8$ , whose expected frequency is  $9.05 \times 10^7$  gauss at [001] and  $8.97 \times 10^7$  gauss at  $20^\circ$  (using the experimental  $\delta_3^1$  and  $\epsilon_3^4$  frequencies). In contrast,  $H_3 = 8.67 \times 10^7$  gauss at [001] and  $\sim 9.6 \times 10^7$  gauss at  $20^\circ$ .

$\epsilon_3^{2a}$

The branch  $\epsilon_3^{2a}$  can almost certainly be assigned to the fourth zone. The electrons producing this branch travel down the neck and along the ridge of the crossed lens surface, re-emerging from the opposite neck. They then move across the hole surface to the neck in the adjacent zone, when viewed in the repeated zone scheme. Half the orbit is shown in Fig. 19.

A rough calculation using Craven's Fig. 7 yields a predicted frequency of  $7.8 \times 10^7$  gauss for this orbit at [110], compared to the measured frequency of  $9.60 \times 10^7$  gauss. The large difference between the

111

experimental and calculated areas, and the discrepancies discussed earlier concerning the  $\epsilon_1^3$ ,  $\epsilon_1^5$ , and  $\epsilon_1^6$  assignments, suggest that the fourth zone surfaces of Craven's model are distorted. As mentioned previously, Devillers and de Vroemen (1971) have also noted appreciable deviations of the model from their radio frequency size effect measurements.

#### Magnetic breakdown at [001]

Except for  $\beta_3^{14}$  and  $\beta_3^5$ , the assignments of frequency branches near [001] to breakdown orbits have been discussed in the section on magnetic breakdown in the (100) plane. The experimental frequencies ascribed to breakdown in this plane are given in Table 15. The proposed breakdown orbits and their corresponding frequencies are also given for comparison. Along [001] the (110) and (100) planes intersect and consequently the frequencies shown in this table should be identical with those in Table 13 for the (100) plane. The largest difference is 0.8%.

#### Magnetic breakdown at [110]

Magnetic breakdown can occur not only at the third zone dumb-bell waist but also at its top. When the magnetic field is parallel to [110], four breakdown orbits are possible. These are shown schematically in

Table 15

Comparison in tin of experimental frequencies,  $f_{exp}$ , with the frequencies,  $f_p$ , of proposed magnetic breakdown orbits (T) for  $H \parallel [001]$ . These orbits are calculated from the measured values of  $\epsilon_3^4$  and  $\delta_3^1$  and frequency units are  $10^7$  gauss.

Orbit	$f_{exp}$	$f_p$	T
$\beta_3^5$	4.58	4.57	$2\beta_3^8 - 2\epsilon_3^4$
"	4.81 <sup>a</sup>	4.79 <sup>a</sup>	"
$\beta_3^6$	11.03 <sup>b</sup>	<del>11.00<sup>b</sup></del>	$\epsilon_3^4 - 2\delta_3^1$
$\beta_3^7$	11.10	11.13	$\epsilon_3^4 - \delta_3^1$
$\beta_3^8$	13.23	13.62	$A_{Bz} + 2\delta_3^1 - \epsilon_3^4$
$\beta_3^{10}$	16.68	16.26	$2\beta_3^8 + 2\delta_3^1 - \epsilon_3^4$
$\beta_3^{11}$	18.27	18.23	$3\beta_3^8 - 2\epsilon_3^4$
$\beta_3^{12}$	19.93	20.37	$3\epsilon_3^4 - \beta_3^8$
$\beta_3^{13}$	22.55	22.49	$2\epsilon_3^4 - \delta_3^1$
$\beta_3^{14}$	29.27	29.5	$3\beta_3^8 - \epsilon_3^4$

a: At  $10^\circ$  from  $[001]$  in the  $(110)$  plane.

b: At  $3^\circ$  from  $[001]$  in the  $(110)$  plane.

Fig. 22 along with the orbits  $\delta_3^2$  and  $\epsilon_3^1$ . In Fig. 22 the two non-equivalent breakdown junctions A and B are shown. To justify assigning the frequencies to magnetic breakdown orbits, the measured frequencies, the proposed breakdown orbits, and their corresponding frequencies have been gathered into Table 16. Only  $\beta_3^4$  has previously been observed (frequency M by DM and  $K_5$  by SV).

The two orbits  $\beta_3^2$  and  $\beta_3^4$  can be constructed from breakdown occurring just at A; however, electrons must tunnel through at both A and B to produce the  $\beta_3^1$  and  $\beta_3^3$  orbits. These experiments represent the first observation of breakdown at the B junction.

The breakdown probabilities at A and B are estimated in Sec. 7.4.

#### (001) plane

The frequency branch  $\delta_2^2$  was observed by CS but not detected in these experiments, and  $\pi_2^2$ , reported by CS, could not be resolved from the  $\pi_2^1$  branch. All other frequencies were measured, two being extended. Five new branches were found.

$\pi_2^1$

The branch  $\pi_2^1$  was observed from [100] (at 45°) to its cut-off at 10°. CS (Fig. 3) reported observing

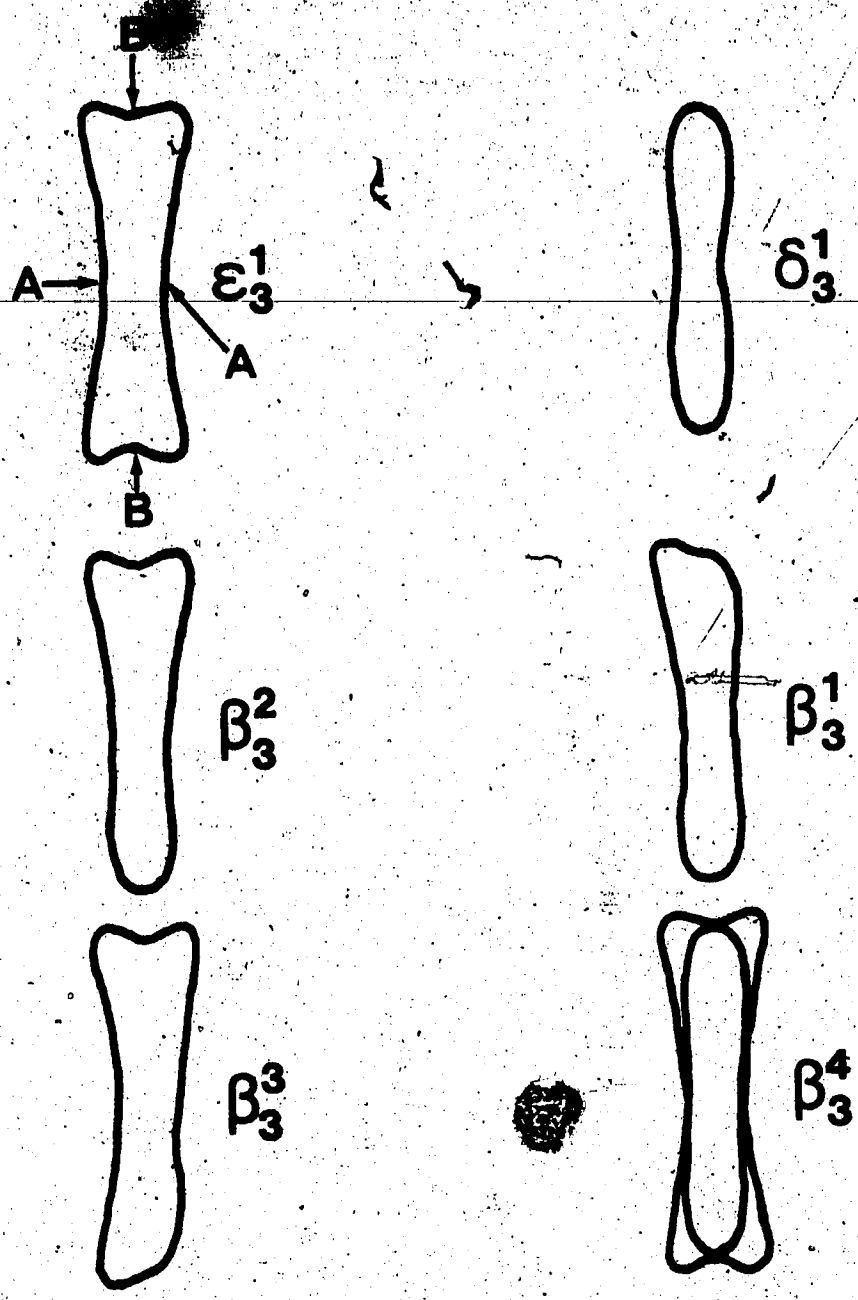


Fig. 22: Cross-sectional view of magnetic breakdown orbits when  $H \parallel [110]$ .

Table 16

Comparison in tin of experimental frequencies,  $f_{\text{exp}}$ , with the frequencies  $f_p$  of proposed magnetic breakdown orbits T for  $H \parallel [110]$ . These orbits are calculated from the measured values of  $\delta_3^1$  and  $\epsilon_3^1$  and the frequency units are  $10^7$  gauss.

Orbit	$f_{\text{exp}}$	$f_p$	T
$\beta_3^1$	1.87	1.88	$0.75\delta_3^2 + 0.25\epsilon_3^1$
$\beta_3^2$	2.07	2.08	$0.5\delta_3^2 + 0.5\epsilon_3^1$
$\beta_3^3$	2.29	2.29	$0.25\delta_3^2 + 0.75\epsilon_3^1$
$\beta_3^4$	4.16	4.16	$\delta_3^2 + \epsilon_3^1$
"	4.55 <sup>†</sup>	4.50 <sup>†</sup>	"

†: At  $56^\circ$  from  $[001]$  in the  $(110)$  plane.

$\pi_2^1$  to  $\sim 12^\circ$ , but did not detect a cut-off.

$\epsilon_2^2$

The  $\epsilon_2^2$  orbit was measured to within  $11^\circ$  of [110] while CS observed it a further  $5^\circ$ .

$\epsilon_2^3$

The continuation of  $\epsilon_3^{2a}$  from the (110) plane is  $\epsilon_2^3$ . As previously discussed, the frequency is assigned to the orbit travelling through four necks when the Fermi surface is viewed in the repeated zone scheme.

The small number of data points for  $\epsilon_2^3$  between [110] and  $\sim 6^\circ$  was due to an accident with the data collection system.

#### Magnetic breakdown at [110]

The four branches in this plane assigned to magnetic breakdown are a continuation of frequencies which have already been discussed in the section on magnetic breakdown in the (110) plane. The angular dependence of the orbit  $\beta_2^4$  has been extended  $10^\circ$  farther than reported by SV; CS and DM failed to detect  $\beta_2^4$ .



## 7.2 Cyclotron Effective Masses in Tin

The cyclotron effective masses presented in Tables 4 to 7 have not previously been measured using ultrasonic attenuation and eight have not been measured by any method. Throughout this section, previous investigations will not be referenced directly since this information has been included in Tables 4 to 7.

Cyclotron resonance provides an alternate method for accurately measuring the cyclotron effective masses. Unfortunately, the orbit corresponding to a particular mass can only be deduced indirectly. This makes comparison with masses determined by the temperature dependence of quantum oscillations (TDQO) difficult and uncertain. Even worse, cyclotron resonance measures the mass ( $m_C^* = \hbar^2 (\partial S / \partial E) / 2\pi$  from Eq. 2.8) at an extremum value of the derivative  $\partial S / \partial E$  (Chambers, 1968) while the TDQO measurements see orbits of extremal area; except on central sections these masses will not normally coincide. For these reasons the masses are not compared with the cyclotron resonance measurements of Khaikin (1962) and van Nieuwstadt and de Vroomen (1967).

### Along [001]

The effective masses found when the magnetic field was along [001] were presented in Table 4. All masses except  $\pi_1^7$  and  $\epsilon_1^4$  agree, within experimental

limits, with the values reported by previous investigators using other techniques. Although one of the three values for  $\epsilon_1^2$  was high (0.59), the average is in agreement with previously reported values.

The  $\pi_1^7$  mass was determined only from the intermediate frequency measurements; the S/N in the high frequency traces was too low to allow evaluation. Although the uncertainty in the measurement was quite large ( $\pm 25\%$ ), the discrepancy with previously reported values is even greater.

The two separate evaluations of the  $\epsilon_1^4$  mass, which agree to within 6%, and previously reported values are substantially different. Unless an error of a factor of two has crept into the calculations of Finkelstein (1974) for this particular mass, the discrepancy is unexplained.

Along [100]

The masses for H parallel to [100] were presented in Table 5. The  $\tau_2^1$  and  $\delta_2^1$  masses agree with previously reported values, but the masses of both  $\pi_2^1$  and  $\epsilon_2^1$  are high. It should be remembered that  $\pi_2^1$  and  $\pi_2^2$  were not resolved in these experiments; consequently, the mass in Table 5 is an average from the two orbits. If the masses were significantly different, however, the data

would deviate from the expected straight line dependence which was not observed.

#### Along [110]

The masses evaluated when  $H$  was parallel to [110] were presented in Table 6. Four new masses were measured, and the others are in agreement with those reported by previous investigations.

#### In the (110) plane

Several effective masses were measured when the magnetic field was at  $2\frac{1}{2}^\circ$  and  $7^\circ$  from [110] in the (110) plane; these were presented in Table 7. Only the  $\pi_3^2$  mass shows a strong dependence with angle.

### 7.3 Comparison of Oscillation Amplitudes in Tin

The theoretical expression for the oscillation amplitude, Eq. 2.8, predicts a strong dependence on angle for intermediate region oscillations. Specifically, the amplitude when  $q$  is perpendicular to  $H$  should be a factor of  $q_l$  smaller than when  $q$  and  $H$  are parallel. In these experiments the  $q_l$  dependence was measured by two different methods as described in Sec. 7.3.1 and Sec. 7.3.2.

### 7.3.1 Comparison of Amplitudes from Sn 2 and Sn 3

The hypothesis of a  $q_z l$  dependence of the oscillation amplitudes ( $\alpha_0$ ) was tested by comparing the amplitudes measured in Sn 2 and Sn 3 when H was parallel to [100]; then  $q_z l = ql$  in Sn 3 and  $q_z l = ql/2$  in Sn 2. No systematic  $q_z l$  dependence appears in the ratios of the amplitudes listed in Table 8 despite the fact that  $ql \sim 150$  (Sec. 4.1.2). If H is parallel to [001],  $\alpha_0$  will be the same in both Sn 2 and Sn 3 according to Eq. 2.8, since  $q_z l = 0$ . However, the experimental results shown in Table 8 do not confirm this. Apparently the electron-phonon interaction has not been included adequately in Eq. 2.8, and as this table demonstrates the factor required to correct the theory is quite large. Since the oscillation amplitudes varied with temperature as predicted by Eq. 2.8 and the calculated masses agreed (in most cases) with ones obtained by other methods, the  $\sinh(\ )$  term in Eq. 2.8 is not affected by this factor.

### 7.3.2 Amplitudes of the Oscillations

A further test of the  $q_z l$  dependence of  $\alpha_0$  was performed by comparing the amplitude of each oscillation as a function of angle,  $\theta$ . The theoretically predicted, systematic dependence was not observed in

any principal plane, as shown in Table 10, despite  $q_l$  being of the order of 150 (Sec. 4.1.2). Thus orbits such as  $\delta$  and  $\tau$ , which are observable across the entire plane, should decrease by two orders of magnitude when  $q$  approaches perpendicularity with  $\underline{H}$ ; a change of less than a factor of five was observed.

This method of checking the  $q_z l$  dependence of  $\alpha_0$  is less certain than that used in Sec. 7.3.1 because the direction of  $\underline{H}$  is changed. Therefore the orbits sample different parts of the Fermi surface and several factors in Eq. 2.8 may vary. Specifically, the density of states  $\rho(E_F, q, l, k_z)$ ,  $\tau_j$ ,  $m_{c_j}^*$ , and the surface curvature  $S''(E_F, k_{zj})$  are expected to change as the field is rotated; however, a variation approaching two orders of magnitude is unlikely. Also, Fenton and Woods (1966) reported that attenuation oscillations in zinc and magnesium did not follow the expected  $q_z l$  dependence.

This test provides further evidence that the interaction of a sound wave with electrons in a magnetic field is much more complex than suggested by Eq. 2.8.

7.4 Estimation of the Magnetic Breakdown Probabilities when H is Parallel to [110]

Magnetic breakdown probabilities are of interest as they provide a direct estimate for the momentum gap

which is an important quantity needed for band structure calculations. It is evident from Fig. 22 that many breakdown orbits associated with the basic orbits  $\delta_3^1$  and  $\epsilon_3^1$  are possible due to tunneling at two distinct points (A and B) in the Brillouin zone.

The conventional method for determining the breakdown field  $H_0$  (eq. 2.12) was not applied here for two reasons: (1) it is not compatible with the Fourier analysis technique used in these experiments; (b) it does not accurately determine "large" values of  $H_0$  such as will be shown to occur for B.

Another method was devised which took advantage of the multiplicity of orbits observed. This made it possible to set up simultaneous equations covering all possible ways of generating the various orbits from sub-sections of the basic orbits multiplied by the tunneling probabilities. It turned out that there are four unknowns and five usable orbit amplitudes given in Table 17, leaving sufficient redundancy to act as a check on the method.

The amplitudes of four orbits were calculated using Eq. 2.8 and the magnetic breakdown damping factor (Chambers, 1966)

$$R = D |p|^m |q|^{(n-m)} \tag{7.1}$$

where tunneling occurs at m of the n junctions on an

Table 17

Experimental oscillation amplitudes  $\alpha_{01}$  and  $\alpha_{02}$  in db of some breakdown orbits and the two basic orbits when  $H \parallel [110]$  from the two sets of measurements used in the calculation of the breakdown fields ( $H_O^A, H_O^B$ ). Experimental amplitudes for some breakdown orbits (and  $\epsilon_3^4$ ) when  $H \parallel [001]$  are included under  $\alpha_{01}$  and the S/N is given for all amplitudes.

Axis	Orbit	$\alpha_{01}$	S/N( $\alpha_{01}^1$ )	$\alpha_{02}$	S/N( $\alpha_{02}^2$ )
[110]	$\delta_3^1$	0.020	12	0.015	6
	$\epsilon_3^1$	0.012	9	0.021	8
	$\beta_3^1$	0.005	2.6	0.002	1
	$\beta_3^2$	0.021	13	0.012	5
	$\beta_3^3$	0.003	1.8	0.003	1
[001]	$\epsilon_3^4$	0.0077	3		
	$\beta_3^5$	0.093	18		
	$\beta_3^8$	0.032	8		
	$\beta_3^{10}$	0.032	8		

orbit. The degeneracy factor,  $D$ , represents the number of distinct orbits of the same area and  $p, q$  are the breakdown and reflection probability amplitudes, respectively. It is assumed in my analysis that an electron travelling on one quarter of the  $\epsilon_3^1$  or  $\delta_3^1$  orbits produce characteristic absorptions  $\alpha_\epsilon^0$  or  $\alpha_\delta^0$ , respectively. By including all factors of Eq. 2.8 in  $\alpha_\epsilon^0$  and  $\alpha_\delta^0$  except  $m_C^*$  and  $R$ , which both depend on the complete orbit, the oscillation amplitude can be simplified to

$$\alpha_0^t = \frac{R m_C^* \Sigma \alpha^0}{\sinh X_1} \quad (7.2)$$

where  $\Sigma \alpha^0$  represents the number of quarter orbits of  $\delta_3^1$  and  $\epsilon_3^1$  required. For example,  $\Sigma \alpha^0 = 4\alpha_\delta^0$  for  $\delta_3^1$  and  $\Sigma \alpha^0 = \alpha_\delta^0 + 3\alpha_\epsilon^0$  for  $\beta_3^1$  as shown in Fig. 22.

The theoretical amplitudes  $\alpha_0^t$  of  $\delta_3^1, \beta_3^1, \beta_3^2$ , and  $\epsilon_3^1$  were equated to the experimental values at [110] and  $\alpha_\delta^0, \alpha_\epsilon^0, P_A$  and  $P_B$  evaluated, where  $P_A$  and  $P_B$  are the probabilities of breakdown at A and B. The results were  $P_A = 0.6$  and  $P_B = 0.01$ , which from Eq. 2.11 gives breakdown fields  $H_0^A = 38$  KG and  $H_0^B = 150$  KG. Since the amplitude of  $\beta_3^1$ , which essentially determines  $P_B$ , was small ( $S/N \sim 2$ ),  $P_B$  could have a "maximum" error of  $\pm 60\%$ , while  $P_A$  is expected to be more accurate ( $\pm 30\%$ ). The amplitude of the extra orbit agreed to within a factor of two which is within the expected error.



The analysis was also applied to similar measurements obtained during another experiment.

The probabilities obtained from the new data were

$P_A = 0.4$  and  $P_B = 0.003$ , corresponding to  $H_O^A = 76 \text{ KG} \pm 50\%$  and  $H_O^B = 480 \text{ KG} \pm 80\%$ , with  $\alpha_O$  unchanged and  $\alpha_C$  a factor of two smaller. The prediction for the redundant orbit amplitude gave exceptionally good agreement with experiment.

It is recognized that for a method of such novelty two sets of measurements are insufficient and further work is necessary to reduce the errors. Another combination of orbits was detected along [001] and could be analysed in a similar though more complex manner. Some of these amplitudes are also given in Table Y7. The amplitudes of some of the larger orbits are, at first sight, too large but this is probably explicable by the large value of  $D$ .

Although the analysis is provisional, it does make possible estimates for the breakdown fields at both junctions. The large difference in  $H_O^B$  determined from the two sets of data may indicate its critical dependence on angle. The other field,  $H_O^A$ , is much larger than the breakdown field of 8 KG (Barklie and Pippard, 1970) determined for the same junction but with  $H$  parallel to [001], rather than [110]. Finally using Eq. 2.12 and Fermi surface curvatures the momentum gap  $k_g$  can be determined from  $H_O$ .

## 7.5 Fermi Surface Frequencies of Indium

### 7.5.1 Fermi Surface Model of Indium

The Fermi surface model of Hughes and Shepherd (1969) is used to assign the measured frequencies to particular orbits. This model supposes a full first and an empty fourth zone. The second zone contains a large hole surface and the third zone has four cylinders joined into a square loop by small necks, as shown in Fig. 23.

### 7.5.2 Assignment of Fermi Surface Frequencies in Indium

No high frequencies were detected that could be attributed to the large hole surface in the second zone. But lower frequencies were observed, as presented in Figs. 17 and 18, and these are ascribed to the third zone arms; the orbits have been drawn on the model in Fig. 23. The frequencies measured in these experiments at both [100] and [110] and displayed in Table 11 agree with the values found by previous investigators.

Both  $\beta_1^2$  and  $\beta_2^4$  have been observed to greater angles than previously. In the (100) plane,  $\beta_1^2$  was extended  $18^\circ$  to  $78^\circ$  from [100] and  $\beta_2^4$  was extended  $10\frac{1}{2}^\circ$  to  $40.5^\circ$  in the (001) plane. The frequencies measured at these angles are included in Table 11.

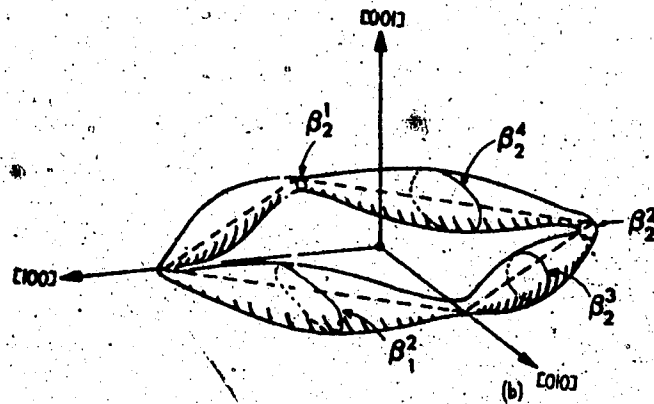
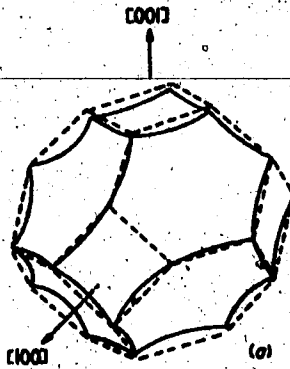


Fig. 23: Model of the Fermi surface in indium according to Hughes and Shepherd (1969): (a) second zone holes; (b) third zone electrons. Orbits corresponding to extremal cross sections are shown.

Two low frequencies were detected; at  $16^\circ$  in the (001) plane and  $53^\circ$  in the (100) plane. Both have been assigned to orbits around the connecting necks. These orbits are drawn on the model in Fig. 23, and from Table 11 the frequencies agree with previously reported values.

## CHAPTER 8

### CONCLUSIONS

A simple method has been devised for rotating a sample about two perpendicular axes while at operating temperatures. This allowed the specimen to be aligned in situ using the symmetry of the Fermi surface. The manufacture of tin samples by the Bridgman technique was found to give specimens of adequate perfection with a minimum of effort.

The method of digital Fourier analysis has proved to be a powerful tool in the extraction of frequencies from the oscillatory attenuation. In addition, a procedure for the accurate calculation of effective masses from the Fourier transform was developed which should find general application.

These experiments have provided much additional information about the Fermi surface properties of tin. The new frequency branches presented in Fig. 11 almost double the number known. In addition, the angular dependence of many orbits previously reported has been extended, and in several cases new cut-offs observed.

Cyclotron effective masses in tin were determined for two-thirds of the orbits, including several new ones, along the three principal axes. The masses

of four orbits were measured off axis (in the (110) plane near [110]).

In tin several differences were noted between the amplitudes and angular ranges of the oscillations observed in the present experiments and those determined with the dHVA effect. These differences provide further evidence that the two methods are complementary rather than competitive.

The many new, unassignable frequencies disclosed in these experiments suggest that the Fermi surface is more complex than Craven's model.

Nine new orbits resulting from the magnetic breakdown of electrons across small forbidden regions have been observed. Their oscillation amplitudes were used to estimate the breakdown field at the two non-equivalent tunneling junctions, one of which had not been detected previously. It was observed that the amplitudes of breakdown orbits along [110] were not as reproducible as non-breakdown orbits. This is probably due to the larger dependence of amplitude on the direction of the field, noted for these orbits, combined with the difficulty of setting angles exactly. The unexpectedly large amplitudes of some breakdown orbits near [001] are explained by the large number of ways of generating those orbits (degeneracy).

Finally, in indium the angular dependence of two frequency branches was extended by a third, and in both planes investigated a frequency from the small Fermi surface neck was detected.

## BIBLIOGRAPHY

- Azbel M.Y. and Kaner E.A. (1958), JETP 6, 1126.
- Balcombe R.J., Guptill E.W., and Jericho M.H. (1964),  
Phys. Lett. 13, 287.
- Barkie R.C. and Pippard A.B. (1970), Proc. R. Soc. A317,  
167.
- Bhatia A.B. (1967), Ultrasonic Absorption (Clarendon  
Press, Oxford).
- Blount E.I. (1962), Phys. Rev. 126, 1636.
- Blömmel H. (1954), Phys. Rev. 96, 220.
- Brailsford A.D. (1966), Phys. Rev. 149, 456, Eq. (23).
- Brandt G.B. and Rayne J.H. (1963), Phys. Rev. 132, 1512;  
(1964), Phys. Lett. 12, 87.
- Bridgman P.W. (1925), Proc. Am. Acad. Arts Sci. 60, 305.
- Cameron J.M. (1960), Fundamental Formulas of Physics,  
Vol. 1, edited by D.M. Menzel (Dover, N.Y.).
- Chambers R.G. (1952), Proc. Roy. Soc. A215, 481.  
(1968), Solid State Physics, 1, 300  
(Gordon and Breach, N.Y.).
- Cohen M.H., Harrison M.J. and Harrison W.A. (1960), Phys.  
Rev. 117, 937.
- Cohen M.H. and Falicov L.M. (1961), Phys. Rev. Lett. 7,  
231.
- Cooley J.W. and Tukey J.W. (1965), Math. of Comput. 19,  
297.
- Cowey J.E., Gerber R. and MacKinnon L. (1974), J. Phys.  
4, 39.



- Cracknell A.P. and Wong K.C. (1973), The Fermi Surface  
(Clarendon Press, Oxford).
- Craven, J.E. and Stark R.W. (1968), Phys. Rev. 168, 849.
- 
- Craven J.E. (1969), Phys. Rev. 182, 693.
- Deacon J.M. and MacKinnon L. (1973), J. Phys. F 3, 2082.
- Devillers M.A.C. and de Vroomen A.R. (1971), Phys. Rev.  
B12, 4631.
- Fenton E.W. and Woods S.B. (1966), Phys. Rev. 151, 424.
- Finkelstein M.M. (1974), J.L. Temp. Phys. 14, 287.
- Fukumato A. and Strandberg M.W.P. (1966), Phys. Lett.  
23, 200.
- Gantmakher V.F. (1962a), JETP 15, 982;  
(1962b), JETP 16, 247;  
(1963), JETP 17, 549;  
(1964), JETP 19, 1366.
- Gold A.V. and Priestley M.G. (1960), Phil. Mag. 5, 1089.
- Gold A.V. (1968), Solid State Physics, 1, 39-126 (Gordon  
and Breach, N.Y.).
- Gradshteyn I.S. and Ryzhik I.M. (1965), Table of  
Integrals, Series, and Products (Academic, N.Y.).
- Gurevich V.L., Skobov V.G., Firsov Y. (1961), 13, 552.
- Hewlett Packard, 433 No. Fair Oaks Ave., Pasadena, Cal.
- Hughes A.J. and Lettington A.H. (1968), Phys. Lett. 27A,  
241.
- Hughes A.J. and Shepherd J.P.G. (1969), J. Phys. C2, 661.

Jenkins G.M. and Watts D.G. (1968), Spectral Analysis and Its Applications (Holden-Day, San Francisco).

Khaikin M.S. (1962), JETP 15, 18.

Kittel C. (1955), Acta Met. 3, 295.

(1967), Introduction to Solid State Physics

(John Wiley and Sons, N.Y.).

Landau L.D. (1930), Z. Physik 64, 629.

Levy M. and Rudnick I. (1963), Phys. Rev. 132, 1073.

Lifschitz I.M. and Kosevich A.M. (1955), JETP 2, 636.

Liu S.H. and Toxen A.M. (1965), Phys. Rev. A138, 487.

Love R.E. and Shaw R.W. (1964), Rev. Modern Physics 36,  
260.

Mason W.P. (1955), Phys. Rev. 97, 557.

Matec Inc., Providence, R.I.

Miller-Stephenson Chemical Co., Inc., 1001 East First St.,  
Los Angeles.

Morse R.W. (1955), Phys. Rev. 97, 1716.

Olsen T. (1963), J. Phys. Chem. Solids 24, 187;

J. Phys. Chem. Solids 24, 649.

Onsager L. (1952), Phil. Mag 43, 1006.

Parrat L.G. (1961), Probability and Experimental Errors in Science (John Wiley and Sons, Inc., N.Y.).

Perz J.M. and Roger W.A. (1971), Can. J. Phys. 49, 296.

Pippard A.B. (1955), Phil. Mag. 46, 1104;

(1957), Phil. Mag. 2, 1147;

(1960), Proc. Roy. Soc. A257, 165;

(1960), Rept. Prog. Phys. 23, 176.

- Rayne J.A. and Chandrasekhar B.S. (1962), Phys. Rev. 125, 1952.
- Reed R.W. and Brickwedde F.G. (1968), RSI 39, 1216;  
(1971), Phys. Rev. B3, 1081.
- Roberts B.W. (1968), Physical Acoustics, IV B, 2.  
ed. W.P. Mason.
- Roger, W.A. (1970), M.Sc. Thesis, unpublished.
- Skobov V.G. (1961), JETP 13, 1014.
- Staflin M.D. and de Vroomen A.R. (1966) Phys. Lett. 23,  
179; (1967) Phys. Stat. Sol. 23, 675; (1967) Phys.  
Stat. Sol. 23, 683.
- Stark R.W. and Falicov L.M. (1967), Prog. L. Tem. Phys.  
5, 235.
- Van Nieuwstadt H.M.M. and de Vroomen A.R. (1967), Phys.  
Lett. 24A, 367.
- Van Weeren J.H.P. and Anderson J.R. (1973), J. Phys. F3,  
2109.
- Vaughan R.W., Ellerman D.D. and MacDonald D.G. (1970),  
J. Phys. Chem. Solids 31, 117.
- Vrba J. (1971), Cryogenics 11, 313.
- Weisz G. (1966), Phys. Rev. 149, 504.

## APPENDIX 1

### Crystallographic Data for White Tin and Indium

White (metallic) tin crystallizes in the body-centred, tetragonal lattice structure with a basis of two atoms per lattice site. The positions of  $\Gamma$ , X, L, and H in the Brillouin zone are shown in Fig. 19. The two-fold symmetric  $\Gamma$ L and  $\Gamma$ X lines are along  $[100]$  and  $[110]$ , respectively, and the four-fold symmetric  $\Gamma$ H line lies along  $[001]$ . The lattice constants, extrapolated to OK, are  $c = 3.15 \text{ \AA}$  along  $[001]$  and  $a = 5.80 \text{ \AA}$  along  $[100]$  (Weisz, 1966). White tin is the only material with this lattice structure at normal temperatures and pressures.

Indium crystallizes in the face-centred tetragonal lattice structure with lattice constants  $a = 4.56 \text{ \AA}$  and  $c = 4.93 \text{ \AA}$  at 4 K (Hughes and Shepherd, 1969). The axial ratio  $c/a = 1.08$  indicates that the lattice is not much distorted from a face-centred cubic structure. There is two-fold symmetry about the  $[100]$  and  $[110]$  axes and four-fold symmetry about  $[001]$ .

## APPENDIX 2

### Definitions of Crystallographic Planes and Cut-off of an Orbit

---

For the results described in this thesis,  $H$  was constrained to be in one of the three principal crystallographic planes. When reference to the (100) plane is made this indicates that  $H$  was in the plane defined by the two crystal axes, [100] and [001]; similarly the (110) plane is defined by [110] and [001] and the (001) plane by [100] and [110]. Orbits, areas, or masses are specified with respect to the axis of  $H$ , and therefore the normal to the cross-sectional area defined by an orbit is parallel to  $H$ .

In these experiments several Fermi surface frequencies were observed to decrease rapidly within a small angle ( $\sim 3^\circ$ ) to the point at which they could no longer be detected. The decrease was attributed to a cut-off of the Fermi surface orbit producing the oscillations. Since the dependence on angle of the frequencies was measured at discrete intervals, the cut-off was determined by plotting the oscillation amplitudes as a function of angle. The particular angle at which the extrapolation of the rapidly decreasing amplitudes had a signal-to-noise ratio of unity was defined as the angle of cut-off.